



UNIVERSITÀ
DEGLI STUDI
FIRENZE

INTERNATIONAL DOCTORATE IN ATOMIC AND MOLECULAR PHOTONICS
CYCLE XXXIII

**ULTRA-SENSITIVE SPECTROSCOPIC MEASUREMENT
OF RADIOCARBON DIOXIDE IN SAMPLES FOR
RELEVANT APPLICATIONS**

Academic Discipline (SSD) FIS/03

Coordinator: Dr. Francesco Cataliotti

Candidate

Maria Giulia Delli Santi

Supervisor

Dr. Paolo De Natale

2017-2020

Contents

Summary	1
1 Theoretical background	4
1.1 Molecules and mid-IR spectroscopy	5
1.1.1 Linear Molecules and symmetric characteristics	5
1.1.2 Energy Levels	7
1.1.3 Line-broadening mechanism	10
1.1.4 Non-linear absorption	12
1.2 High-resolution Spectroscopy	14
1.2.1 Doppler-Free Saturation Spectroscopy	14
1.2.2 Feedback control techniques for high-resolution spectroscopy	15
1.2.3 Polarization spectroscopy for frequency-lock	17
1.2.4 Pound-Drever-Hall (PDH) technique for frequency-lock	20
1.3 High-sensitivity spectroscopy	21
1.3.1 Cavity-enhanced absorption methods	21
1.3.2 High-finesse optical resonator	22
1.3.3 Cavity ring-down spectroscopy	23
1.3.4 Sensitivity Limits of CW-CRDS	26
1.3.5 Saturated-absorption cavity ring-down spectroscopy	27
2 Radiocarbon: its cycle and its detection	30
2.1 Carbon Isotopes	31
2.2 Radiocarbon decay	32
2.3 Global Carbon Cycle	34
2.4 Radiocarbon detection	37
2.4.1 Limits encountered in AMS and LSC radiocarbon detection	39
2.4.2 Radiocarbon detection using mid-IR spectroscopy	41
2.4.3 Fields of applications	42

3 Saturated-Absorption Cavity Ring-down (SCAR) technique	46
3.1 Experimental setup	47
3.2 Fabry-Pérot ring-down cavity	48
3.3 Single-frequency QCL loop chains	50
3.3.1 Pound-Drever-Hall (PDH) locking	51
3.3.2 Polarization spectroscopy (PS) locking	51
3.3.3 Beat note phase-locking	53
3.4 Data acquisition and fitting procedure	55
3.5 Sample preparation protocol and CO ₂ extraction line	56
4 Sample characterization by SCAR technique and results	62
4.1 Evidence of the role of the sample preparation	64
4.2 Raw data: ratios of unknowns to standards	65
4.3 Biofuel samples investigated by C14-SCAR spectrometer	67
4.4 Biopolymer samples investigated by the C14-SCAR spectrometer	71
4.5 Enriched samples investigated by the C14-SCAR spectrometer	72
4.6 Archaeological samples investigated by the C14-SCAR spectrometer	74
Conclusions and outlook	78
Appendix	81
A Photodissociation of N₂O molecule	82
List of Abbreviation	88

Summary

In recent years, the interest for mid infrared (3 - 50 μm) radiation has increased for both fundamental research and industrial applications, thanks to the development of continuous-wave room-temperature sources, such as quantum cascade lasers, which fulfill the requests for relatively high power, narrow emission and compact size. However, optoelectronic technologies in the mid-infrared region are still under development and do not achieve the performance levels of other spectral regions, yet. The main absorption lines of simple molecules lie in this spectral region and the study of their absorption spectra can give precise information on their concentration. Both these aspects enabled widespread applications of tunable laser absorption spectroscopy for real-time, in-situ and non-invasive gas sensing. Trace gas detection by optical spectroscopy plays a key role in applications that demand quantitative measurements of extremely small amounts of molecular gases. The enormous relevance and the complex interplay between climate change and anthropogenic influence, has focused the attention on mitigation of the greenhouse gases effects, the well known increase in the average planetary temperature and the increase in atmospheric concentrations of climatically active gases, including carbon dioxide (CO_2). Indeed, since the increase in concentration of infrared-active gases is responsible for solar radiation trapping, this warming effect has been definitely related to the rise of the industrial era, with a sudden acceleration in the last few decades. Therefore, the anthropogenic contribution, mainly due to the extensive use of fossil fuels combustion, is currently able to significantly compromise the planetary energy balance. In this context, the scientific and industrial debate focuses on possible methods for measuring and quantifying CO_2 emissions from fossil sources, since the identification of markers to control and monitor the reduction of these sources is a necessary step to implement any mitigation politics. In this respect, radiocarbon method represents the most promising approach to validate the estimations provided by single nations or companies. ^{14}C is produced in the stratosphere when cosmic rays interact with the Earth's atmosphere. During its cycle of production and decay, radiocarbon is oxidized to radiocarbon dioxide and it is diffused into the troposphere and enter in the global C cycle between atmosphere land and oceans. Radiocarbon is a natural clock, with a lifetime of about 5,700 years, and the measurement of its concentration is an optimal approach to distinguish "young" samples from very old ones, like fossil fuels, completely depleted in radiocarbon. Therefore, non-zero concentrations of

radiocarbon can be found in atmospheric CO₂ and in any biogenic sample extracted from organic matter. However, ultra-high detection sensitivity is required to quantify radiocarbon due to its extremely low natural abundance being about one part per trillion (10⁻¹²) in the biosphere. Until the last years, only accelerator mass spectrometry (AMS) provided this sensitivity, achieving uncertainty values < 1%, but its complexity and costs suggested to explore the possibility of realizing the same measurement using a spectroscopic approach.

Thanks to the combination of continuous wave-cavity ring down spectroscopy (CW-CRDS) and strong absorption from fundamental ro-vibrational molecular transitions in the mid-infrared, we can overcome the detection limit imposed by the small amount of molecular gases. CW-CRDS is among the most sensitive techniques to measure absorption coefficients of molecular transitions with no need for complex calibration routines. Nevertheless, state-of-the-art conventional CW-CRD spectrometers in the mid IR cannot reach the minimum detectable absorption level required to detect ¹⁴CO₂, mainly because of the empty-cavity decay rate fluctuations. To overcome this limitation, about ten years ago a novel high-resolution and high-sensitivity spectroscopic technique was proposed: Saturated-Absorption Cavity Ring-down (SCAR) spectroscopy. Such technique has shown to improve by more than one order of magnitude the limits of conventional linear-absorption CRDS, thanks to a sample absorption measurement which is independent from the other cavity losses during the same cavity decay event. Indeed, SCAR, benefiting from both CW-CRDS and saturation spectroscopy, overcomes the limits of linear CRD by measuring in each and every single decay event both the "empty" and the "full" cavity contribution. Thanks to the achieved sensitivity, detection of rare molecular species, such as radiocarbon dioxide, was demonstrated. With this work, we describe the optimization of this spectroscopic technique able to detect ¹⁴C, the rarest isotope of carbon, measuring its content in carbon dioxide, for specific samples related to three very important application areas. In particular, in this work, biogenic vs. fossil fraction determination in biofuels and biopolymers is tackled; enriched samples from nuclear power plants are studied for decommissioning; the highest SCAR sensitivity is used to date archaeological samples. The essential ingredients for such experiments are a high-finesse cavity and a narrow-linewidth, frequency-stabilized light source, tunable and powerful enough to enable a Doppler-free technique and to detect the target molecular transition with a good signal-to-noise ratio. The core of this work is dedicated to the optimization and validation of the SCAR technique by performing the first ever measurements of real-world samples, providing key infos about the three areas specified above. The ¹⁴C content in the CO₂ sample is determined by measuring the spectral area of the contribution to the CRD decay rate from the absorbing target line. In practice, we measure changes of lifetime, within the high-finesse SCAR cavity, of photons resonant with the selected (00⁰1 - 00⁰0) P(20) ro-vibrational transition of ¹⁴C¹⁶O₂ around 4.5 μm. Since these changes directly depend on the molecular line absorption, we can calculate the ¹⁴CO₂ concentration. One of the limits of the SCAR technology is linked to the presence of absorption lines belonging to interfering molecules and isotopologues which lie in the spectral range of investigation. They can affect the SCAR results, introducing possible

systematic errors. To improve this aspect, we developed a sample preparation protocol able to both extract the CO₂ isotopic mixture from the investigated system, by means of a combustion reaction, and remove interferences. It allows us to eliminate systematic effects due to the sample combustion procedure, necessary to produce CO₂ to be analysed. In particular, the (01¹1-01¹0) Q(12)e transition of N₂O, which lies in the spectral range of investigation, partially overlaps with the investigated target transition. This protocol and the effect on the C14-SCAR apparatus were validated on samples of biofuels, polymers, enriched graphite coming from the decommissioning of a power plant, and charcoal from a Sumerian site of archaeological interest. Our results are provided by a comparison with the standard method for radiocarbon dating AMS, to prove the accuracy and reliability of the SCAR technique.

This thesis is developed in two parts. In the first one, Chap.1 and Chap.2, the theoretical elements linked to the working principles of the SCAR technology are described. Moreover, a description of the investigated molecular system (¹⁴C¹⁶O₂) and the reason for the interest in radiocarbon detection is provided. The second part of this thesis consists of Chap.3 and Chap.4. In the third chapter, SCAR spectroscopy is discussed. In particular, a description is given of the high-finesse cavity as well as of the techniques to generate and stabilize single-frequency coherent mid-infrared radiation and the sample treatment procedure. The author set up from scratch all the sample treatment procedures, during her PhD thesis, specifically compatible with SCAR analysis: in the next chapter the key needs will be explained in detail. In the fourth chapter the achieved results are presented and discussed.

1

Theoretical background

The number of possible systems and techniques which can be defined under the heading of laser-based sensors is wide. The aim of this chapter is to introduce key theoretical elements needed for developing and optimizing a light source and a spectroscopic technique able to perform high-sensitivity optical detection of radiocarbon dioxide by measuring the P(20) spectral line of the $^{14}\text{C}^{16}\text{O}_2$ molecule. The first section of this chapter will introduce some basic notions of molecular spectroscopy in the mid-IR spectral region. The second and third sections will describe the main laser-based spectroscopic techniques able to achieve, respectively, high resolution and sensitivity. In particular saturated-absorption cavity ring-down spectroscopy will be introduced as a high-performance technique benefiting from both advantages.

1.1 Molecules and mid-IR spectroscopy

Molecules have always played a role of interest as physical systems. Spectroscopy studies their interaction with electromagnetic radiation. The mid-infrared (mid-IR) spectral region (3 – 50 μm) is considered a domain of interest in many areas of science and technology since, due to strong fundamental ro-vibrational transitions, it offers highly discriminatory information allowing molecule-specific detection. A large number of molecules undergo strong transitions in this domain, therefore mid-IR spectroscopy stands out as an univocal way to identify and quantify molecular species, including isotopologues, in a given environment. This section provides an overview of IR molecular spectra, focused on linear molecules, in particular carbon dioxide. The second part of this section introduces the collective absorbing behaviour of a molecular gas sample, explaining broadening phenomena (homogeneous and inhomogeneous) and saturation effects.

1.1.1 Linear Molecules and symmetric characteristics

Any molecule can be described as a geometric object belonging to a symmetry group characterized by all transformations under which the object remains invariant. Linear molecules belong to the point groups $D_{\infty h}$ or $C_{\infty v}$, depending on whether or not they have a plane of symmetry perpendicular to the inter-nuclear axis. The symmetric molecule $^{12}\text{C}^{16}\text{O}_2$, belonging to the first group, has zero permanent dipole moment, hence only transitions involving vibrational modes with a periodic change of the dipole moment can be observed in the mid IR. The CO_2 molecule has three vibrational modes showed in Fig. 1.1.

- Symmetric stretch, labelled ν_1 , does not break the molecular symmetry so it is inactive in the mid IR.
- Bending, labelled ν_2 , is doubly degenerate. For this mode the additional quantum number l is used. It is active in the mid IR with a characteristic frequency of 667 cm^{-1}
- Asymmetric stretch, labelled ν_3 , is active in the mid IR with a characteristic frequency of 2349 cm^{-1} ($\lambda = 4.25\ \mu\text{m}$).

Molecules belonging to this point group, according to the symmetrisation postulate, can be symmetric or antisymmetric with respect to an exchange of the identical nuclei. For a better understanding, we can consider the wavefunction describing a molecule in the Born-Oppenheimer approximation. It can be factorized as follows:

$$\psi_{mol} = \psi_t \psi_e \psi_v \psi_r \psi_n \quad (1.1)$$

Where ψ_t describes the translation, ψ_e the electronic state, ψ_v and ψ_r the vibration and the rotation of the molecule respectively, and ψ_n the nuclear spin. The functions describing the

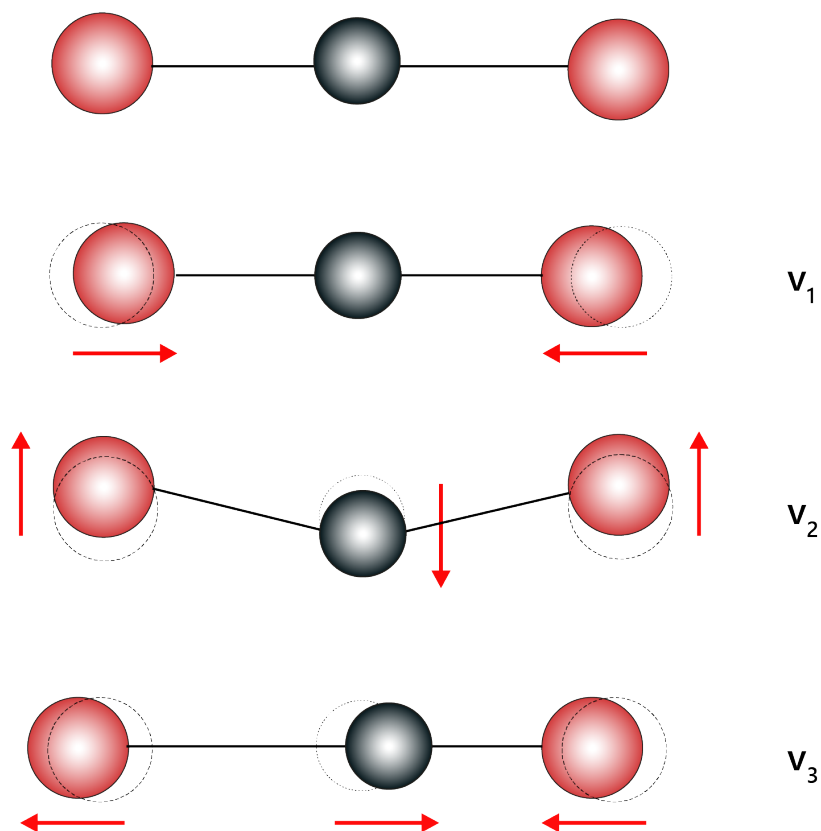


Figure 1.1: **Normal vibrational modes of CO₂ molecule:** Symmetric stretching (ν_1), bending (ν_2), asymmetric stretching ν_3

rotational states are the spherical harmonics while the functions describing the vibrational states depend on the inter-nuclear distance and resemble those describing the harmonic oscillator. The total eigenfunction ψ of the system changes sign or remains unchanged when the nuclei are inverted. For example, the ground electronic and vibrational wavefunctions of the C¹⁶O₂ molecule are symmetric in the exchange of the two ¹⁶O₂ nuclei. Also, the nuclear wavefunction is symmetric, since the nuclear spin $I(O^{16}) = 0$, while, the rotational wave function is symmetric for even values of J and antisymmetric for odd ones. Since the symmetrisation postulate requires the total wavefunction to be symmetric in the exchange of the two ¹⁶O nuclei, the rotational states with odd values of J are forbidden in the ground vibrational state. A vibrational state of the molecule can be generally expressed as $|v_1 v_2^{l_2} v_3 \dots\rangle$. A similar argument could show that the situation is reversed in the 00⁰1 vibrational state, for which even values of J are forbidden, because the vibrational wavefunction in the excited state is antisymmetric. As a consequence, detection of a weak transition of the ro-vibrational form

$00^01 - 00^00 R(J)$ with an odd value of J could indicate a symmetrisation postulate violation and its amount [1].

1.1.2 Energy Levels

Let us consider the total wavefunction in the Born-Oppenheimer approximation, described in Eq.1.1. Since the energy associated to mid-IR thermal radiation at room temperature is too low to excite electronic transitions, we can consider the molecule at rest in the center of mass reference frame and assume it to be in its electronic ground state. In this condition, the translational and electronic contributions can be omitted. The ro-vibrational energy of a molecule can be expressed, in frequency units, as:

$$\frac{E}{h} = G(\nu_1, \nu_2, \dots) + F(J) \quad (1.2)$$

The *vibrational contribution* G depends on the vibrational normal modes of the molecule (labelled ν_1, ν_2, \dots) and it is tightly linked to the symmetry properties of the molecule. For a generic polyatomic molecule the number of vibrational degrees of freedom (DoF) is $3N - 6$ where N is the number of atomic nuclei in the molecule. This result comes considering that the motion of each atomic nucleus is described by three DoF, but looking at the molecule as a system, 3 of them describe the translation of the center of mass, while other 3 describe the rotation of the system. For linear molecules, the number of vibrational DoF is equal to $3N - 5$ because there is no rotation around the molecular axis. Each vibrational mode can be in its ground state ($\nu_i = 0$) or in an excited state ($\nu_i = 1, 2, \dots$). The vibrational contribution can be described as follows:

$$G(\nu_1, \nu_2, \dots) = \sum_i \nu_i \left(\nu_i + \frac{d_i}{2} \right) + \sum_{i, k \geq i} x_{ik} \left(\nu_i + \frac{d_i}{2} \right) \left(\nu_k + \frac{d_k}{2} \right) + \sum_{i, k \geq i} g_{ik} l_i l_k + \dots \quad (1.3)$$

The first term of the equation represents the energy of the molecular harmonic vibration where $\nu_i = \omega_i/2\pi$ is the vibrational frequency related to the mode ν_i , d_i is the mode degeneracy. The second term takes into account the correction due to the anharmonicity of the oscillation, x_{ik} is the anharmonicity constant. The third term expresses the contribution of the vibrational angular momentum from degenerate modes, g_{ik} is the related constant and l_i the quantum number.

The *rotational contribution* $F(J)$ depends on the total angular momentum quantum number ($J = 0, 1, 2, \dots$) and can be expressed as:

$$F(J) = BJ(J+1) - DJ^2(J+1)^2 + \dots \quad (1.4)$$

The first term represents the rotational energy with the rotational constant $B = \frac{h}{8\pi^2 I}$ and I moment of inertia. The second term represents the centrifugal distortion related to the

non-rigidity of the molecule, accounting for the variation of the internuclear distances at increasing rotation speed. Since the moment of inertia changes during a vibration, so that the average value of $1/I$ is slightly different with respect to its value in the equilibrium position, the rotational constant has a little dependence on the vibrational level. Therefore, the expression for the rotational constant becomes:

$$B_{[v]} = \frac{h}{8\pi^2 I} - \sum_i \alpha_i \left(v_i + \frac{d_i}{2} \right) \quad (1.5)$$

The population of each levels depends on J through the expression:

$$N_J = g_J e^{-\frac{hF(J)}{k_B T}} \quad (1.6)$$

where the Boltzmann factor gives the population level at the absolute temperature T . For a linear symmetric molecule, $g_J = 2J + 1$ corresponds to the number of degenerate rotational levels. The energy levels are given by the following equation:

$$\frac{E_r(J)}{h} = B_v J(J+1) - D_v J^2(J+1)^2 + H_v J^3(J+1)^3 + L_v J^4(J+1)^4 + \dots \quad (1.7)$$

where the terms D_v , H_v , L_v are related to the non-rigidity of the molecule (centrifugal distortion). Also for these terms holds the relation expressed by Eq. 1.5. In order to estimate what are the allowed transitions for the investigated molecule, some selection rules, obtained by evaluating the matrix elements of the electric dipole moment between the molecular states, are established. If and only if the molecule has a non-zero permanent dipole moment, purely rotational spectra can be observed, whereas it is possible to have ro-vibrational spectra (in the IR region) if the dipole moment differs from the initial to the final state. As previously mentioned in Sec. 1.1.1, since $^{12}\text{C}^{16}\text{O}_2$ has zero permanent dipole moment, only the ro-vibrational spectrum can be observed. The two asymmetric modes ν_2 and ν_3 (see Fig. 1.1) of the CO_2 molecule induce a periodic variation of the dipole moment, therefore they are active in the IR region. Let us indicate with the subscript k the upper state, with i the lower one. If we consider transitions between non-degenerate vibrational states (Σ states), the selection rules for ro-vibrational transitions impose:

$$\Delta v = \nu_k - \nu_i = \pm 1 \quad (1.8)$$

and

$$\Delta J = J_k - J_i = \pm 1 \quad (1.9)$$

The transitions corresponding to $\Delta J = +1$ form the R branch, while the ones corresponding to $\Delta J = -1$ define the P branch. Once given the center frequency of the vibrational transition ν_0 , each line forming the same band, given by the involved rotational levels $F(J_k) - F(J_i)$, is

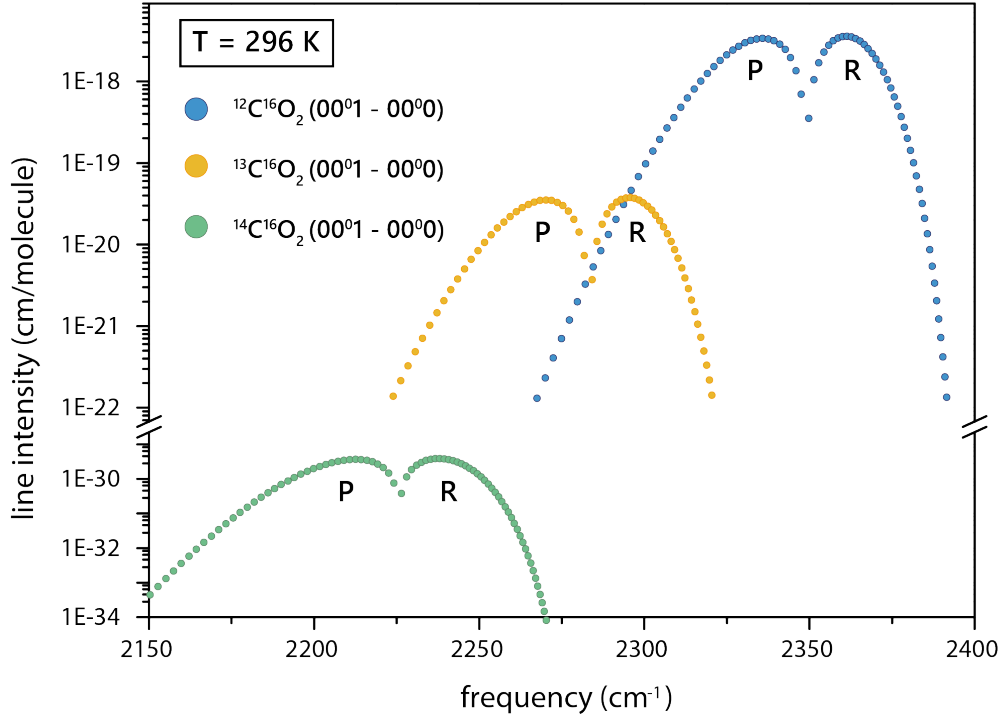


Figure 1.2: Three common CO₂ bands around 4.25 μm at a temperature $T = 296$ K, where the frequency scale is expressed in cm^{-1} ($1 \text{ cm}^{-1} = 29.9792458 \text{ GHz}$). The $(00^01 - 00^00)$ band (blue) of the $^{12}\text{C}^{16}\text{O}_2$ molecule is the most intense, since it involves the ground vibrational state of the most abundant isotopologue. The same $(00^01 - 00^00)$ bands of the $^{13}\text{C}^{16}\text{O}_2$ and $^{14}\text{C}^{16}\text{O}_2$ isotopologues are plotted in orange and green, respectively. In these bands only transitions involving a lower rotational state with even J are allowed by vibrational levels symmetry and by the ^{16}O nuclear spin (0). Source: HITRAN database, [2]

obtained by:

$$\nu = \nu_0 + (B_k + B_i)m + (B_k - B_i)m^2 \quad (1.10)$$

where $m = J + 1$ for the R branch and $m = -J$ for the P branch. These spectral lines are almost equispaced. For those transitions where $\Delta J = 0$ is allowed, the additional Q branch is present. Our work is focused on $^{14}\text{C}^{16}\text{O}_2$, a rare and unstable isotopologue of CO₂. Spectroscopic measurement of radiocarbon dioxide requires accurate knowledge of both line positions and intensities. Since the release of the HITRAN database contains only a limited number of entries for the symmetric isotopologues of carbon dioxide, we used a recent work which provided the *ab initio* computed intensities [2]. The intensity of $^{14}\text{C}^{16}\text{O}_2$ isotopologue lines are normalized to its natural abundance ($1.2e^{12}$). Fig. 1.2 shows the strongest bands of three relevant symmetric CO₂ isotopologues.

1.1.3 Line-broadening mechanism

The spectral distribution $I(\nu)$ of the absorbed or emitted intensity around the central frequency ν_0 , corresponding to the molecular transition with energy difference $\Delta E = E_k - E_i$ between the upper and lower levels, is observed by high resolution spectroscopy [3]. The *Line profile* is referred to the function $I(\nu)$, while $\delta\nu = |\nu_2 - \nu_1|$ is the interval between the two frequencies for which $I(\nu_1) = I(\nu_2) = \frac{I(\nu_0)}{2}$, known as *full-width at half-maximum* (FWHM) of the line. The *natural linewidth* of an absorption transition can be derived starting from:

$$dI = -\alpha_{ik}I dz \quad (1.11)$$

where I is the intensity of a plane wave traveling in the z -direction through an absorbing species, decreasing along the space interval dz , and α_{ik} is the absorption coefficient for the transition $|i\rangle \rightarrow |k\rangle$ depending on the population densities N_i , N_k of the lower and upper levels, and on the optical absorption cross section σ_{ik} , according with the following equation:

$$\alpha_{ik}(\omega) = \sigma_{ik}(\omega) \left[N_i - \frac{g_i}{g_k} N_k \right] \quad (1.12)$$

When $N_i \gg N_k$, integration of Eq. 1.11, yields the Beer-Lambert law:

$$I = I_0 e^{-\sigma_{ik} N_i z} \quad (1.13)$$

The absorption profile $\alpha(\omega)$ can be obtained from the classical model of a damped oscillator with elementary electric charge e under the influence of an incident wave. In the neighbourhood of a molecular transition frequency $\omega_0 \gg |\omega_0 - \omega|$, the dispersion relations become:

$$\alpha(\omega) = \frac{Ne^2}{4\epsilon_0 mc} \frac{\gamma}{(\omega - \omega_0)^2 + (\gamma/2)^2} \quad (1.14)$$

$$n(\omega) = 1 + \frac{Ne^2}{4\epsilon_0 m\omega_0} \frac{\omega - \omega_0}{(\omega - \omega_0)^2 + (\gamma/2)^2} \quad (1.15)$$

with ϵ_0 dielectric constant in vacuum, m the mass of the oscillator and $\omega_0 = 2\pi\nu_0$ is the transition center frequency of the damped oscillator, corresponding to $\omega_{ik} = (E_i - E_k)/\hbar$. The natural linewidth γ , related to the Einstein coefficients A_{21} , B_{21} for the spontaneous and stimulated emission respectively, is:

$$\gamma = A_{21} = \frac{2h\nu^3}{c^3} B_{21} \quad (1.16)$$

Homogeneous broadening

The essential feature of a molecular transition that is homogeneously broadened is that a signal applied to it has exactly the same effect on all molecules in the ensemble. Lineshape in this case is given by a Lorentzian. The principal mechanisms resulting in a homogeneously broadened line are:

- *Lifetime broadening.* This type of broadening is caused by the radiative decay of the molecular system. Spontaneous emission or fluorescence has a radiative lifetime. Broadening of the molecular transition due to this process is related to the lifetime of the specific level involved.
- *Collisional or pressure broadening.* It arises from the interruption of the radiative process due to collisions between particles. Indeed, the long wave train, which would otherwise be present, becomes truncated when a collision interrupts either the emission or the absorption of radiation. The process is restarted after the collision, without any memory of the phase of the radiation preceding the collision. Since the spectral width of a wave train is inversely proportional to its pulse duration, in the presence of collisions, the radiation line width is greater than for an uninterrupted individual process.

Inhomogeneous broadening

If the probability of absorption depends on each specific molecule, it is said that the line is inhomogeneously broadened. Mechanisms which cause inhomogeneous broadening tend to displace the center frequencies of absorption for individual molecules, thereby broadening the overall response of an ensemble. For example, owing to Doppler shift, different molecules have slightly different resonance frequencies on the same transition. An applied signal, at a given frequency within the overall inhomogeneous linewidth, interacts strongly solely with those molecules whose shifted resonance frequencies lay close to the signal frequency [4]. The most significant example of inhomogeneous line broadening is *Doppler broadening* due to the Doppler effect caused by a distribution of velocities in the molecular sample. The probability of absorption of monochromatic radiation is dependent on the velocity of the single molecules. Since the velocity distribution in a sample in thermal-equilibrium conditions follows the Boltzmann statistics, the shape of purely inhomogeneously broadened absorption lines is Gaussian, with a FWHM given by:

$$\Delta\nu_{DB} = \frac{\nu_0}{c} \sqrt{8 \ln 2 \frac{k_B T}{m}} \quad (1.17)$$

Since the width depends on the ratio between temperature and molecular mass, cooling the sample can reduce it. In order to understand how the homogeneous and inhomogeneous broadening mechanisms interact to give the real line shape, we may divide the molecules

in the same initial state into subgroups, such that all molecules with a velocity component within the interval from v_z to $v_z + \Delta v_z$ belong to one subgroup. If we choose $\Delta v_z = \gamma/k$, where k is the wavenumber, we may consider the frequency interval γ to be homogeneously broadened inside the much larger inhomogeneous Doppler width. It means that all molecules in the subgroup can absorb or emit radiation with frequency $\omega = \omega_0 + v_z k$. In this case the line shape is a Voigt profile resulting from the convolution between Lorentzian and Gaussian profiles.

1.1.4 Non-linear absorption

As it will be described in Sec. 1.2, several spectroscopic techniques can achieve sub-Doppler resolution, e.g. saturation spectroscopy. They are based on *non-linear absorption* interaction of molecules with the laser radiation. The population density of molecules in the absorbing level is decreased by optical pumping. This results in a non-linear dependence of the absorbed radiation power on the incident power [5]. It is known that when a plane electromagnetic wave $E = E_0 \cos(\omega t - kz + \phi)$ passes through an absorbing sample, travelling along the z direction, the power absorbed in a volume $dV = Adx$ is:

$$dP = -P\alpha dx = -AI\sigma_{ik}\Delta N dx \quad (1.18)$$

where A is the area crossed by the radiation, $\sigma_{ik}(v)$ is the absorption cross-section and ΔN is the difference of the population density between the upper $|k\rangle$ and the lower $|i\rangle$ level and the intensity I is defined as:

$$I = \frac{1}{2} c \epsilon_0 E_0^2 \quad (1.19)$$

If the incident intensity I is low, ΔN and the absorption coefficient α are constant, then the absorbed power dP is linearly dependent on the power P . Integration of 1.18 gives Beer-Lambert law of *linear absorption*:

$$P = P_0 e^{-\alpha z} = P_0 e^{-\sigma \Delta N z} \quad (1.20)$$

Let us consider the *non-linear absorption* in more detail. If the incident plane wave, with the spectral energy density $\rho_\nu(\nu) = I_\nu(\nu)/c$ has the spectral width $\delta\nu_L$, the intensity will be:

$$I = \int I_\nu(\nu) d\nu \approx I_\nu(\nu_0) \cdot \delta\nu_L \quad (1.21)$$

The absorbed power for a monochromatic laser wave tuned to the center-frequency ν_0 of an absorption line becomes:

$$dP = \Delta N \cdot dV \cdot I_\nu(\nu_0) \cdot \sigma_{ik}(\nu_0) \delta\nu_L \quad (1.22)$$

If the spectral width $\delta\nu_L$ of the laser is larger than the width $\delta\nu_a$ of the absorption line, only that part of the spectral interval inside the line width $\delta\nu_a$ of the absorption line is absorbed, and the absorbed power becomes:

$$dP = \Delta N \cdot dV \cdot I_\nu(\nu_0) \cdot \sigma_{ik}(\nu_0) \cdot \delta\nu_a \quad (1.23)$$

This shows how much important is to have a laser source narrower in frequency than the absorption, since the spectral portion of the optical power that falls outside the absorption line does not contribute to the detection. The population difference in saturation conditions is given by:

$$\Delta N = \frac{\Delta N_0}{1 + S} \quad (1.24)$$

where $S = \frac{I}{I_s}$ is the *saturation parameter*, with I_s saturation intensity depending on the spontaneous emission Einstein A coefficient and the relaxation rates of populations and coherence. If $\delta\nu_a > \delta\nu_L$, the Eq. 1.23 becomes:

$$dP = dV \cdot I(\nu_0) \sigma_{ik}(\nu_0) \frac{\Delta N_0}{1 + S} \quad (1.25)$$

The saturation of homogeneously broadened transitions with Lorentzian profiles gives again a Lorentzian profiles with a FWHM

$$\Delta\nu_s = \Delta\nu_0 \sqrt{1 + S(\nu_0)} \quad (1.26)$$

and the absorption coefficient:

$$\alpha(\nu) = \frac{\alpha_0(\nu)}{1 + S(\nu)} \quad (1.27)$$

decreases by the factor $[1 + S(\nu)]^{-1}$, whereas the saturation parameter $S(\nu)$ has a Lorentzian line profile and the saturation is stronger at the line center than in the line wings. When a monochromatic wave passes through a molecular sample, only those molecules with velocity v_z contribute to absorption. The absorption cross-section is given by:

$$\sigma(\omega - \omega_0 - kv_z) = \sigma_0 \frac{(\gamma/2)^2}{(\omega - \omega_0 - kv_z)^2 + (\gamma/2)^2} \quad (1.28)$$

but even though a hole (called *Bennet hole*) in the population difference is burned, the absorption coefficient still shows a Voigt profile (as in the non-saturated case). The Bennet hole can, however, be detected if two lasers are used:

- The saturating pump laser with the wave vector \vec{k}_1 , which is kept at the frequency ω_1 and which burns a hole into the velocity class $v_z \pm \Delta v_z/2$, with $v_z = (\omega_0 - \omega_1)/k_1$ and $\Delta v_z = \gamma/k_1$

- A weak probe laser with the wave vector \vec{k}_2 and a frequency ω tunable across the Voigt profile. This probe laser is sufficiently weak to cause no extra saturation.

This is the working principle of the *Doppler-free saturation spectroscopy*.

1.2 High-resolution Spectroscopy

In molecular spectroscopy, several effects can cause a broadening or a frequency shift of the spectral lines. In the range from IR to ultraviolet, the Doppler width of the spectral lines is the main effect that precludes the observation of fine structures and a precise determination of the transition frequency. With the introduction of lasers, several techniques developed solutions to obtain spectra with resolution not limited by Doppler broadening. As a general rule, these techniques are available by using two counter-propagating laser beams. A molecule moving with non-zero velocity along the direction of the beams sees the frequencies of the two beams shifted at a higher and a lower frequency. Starting from this effect, two sub-Doppler detection schemes can be identified: the first is speed-selective spectroscopy, e.g. saturation spectroscopy; the second is two-photon spectroscopy. The specific effect induced by the laser and the method for inducing and detecting such effect, characterize the different techniques.

1.2.1 Doppler-Free Saturation Spectroscopy

Pump and probe waves may be generated by a single laser. Let I_1 be the intensity of the pump beam, identified with the wave vector \vec{k}_1 and I_2 be the intensity of the probe beam, identified with the wave vector \vec{k}_2 [5]. Since they are counter-propagating, we have $\vec{k}_2 = -\vec{k}_1$ and the saturated population difference in case of equal intensity $I_1 = I_2 = I$ is:

$$\Delta N(v_z) = \Delta N_0(v_z) \times \left[1 - \frac{S_0(\gamma/2)^2}{(\omega - \omega_0 - kv_z)^2 + (\gamma/2)^2} - \frac{S_0(\gamma/2)^2}{(\omega - \omega_0 + kv_z)^2 + (\gamma/2)^2} \right] \quad (1.29)$$

Due to opposite Doppler shift, the two waves with frequency ω produce two Bennett holes at the velocity components $v_z = \pm(\omega - \omega_0)/k$ into the population distribution, and the saturated absorption coefficient becomes:

$$\alpha(\omega) = \alpha_0 \left[1 - \frac{S_0}{2} \left(1 + \frac{(\gamma_s/2)^2}{(\omega - \omega_0)^2 + (\gamma_s/2)^2} \right) \right] \quad (1.30)$$

where $\gamma_s = \gamma\sqrt{1 + S_0}$ and $S_0 = S(I, \omega_0)$. This represents the Doppler-broadened absorption profile with a dip at the line center $\omega = \omega_0$ called *Lamb dip*. It means that both waves are absorbed by the same molecules with $v_z = (0 \pm \gamma_s/2)/k$ which move perpendicularly to the laser beams. The intensity per molecule absorbed is now twice as large, and the saturation accordingly higher. In saturation spectroscopy, the spectral resolution is no longer limited by

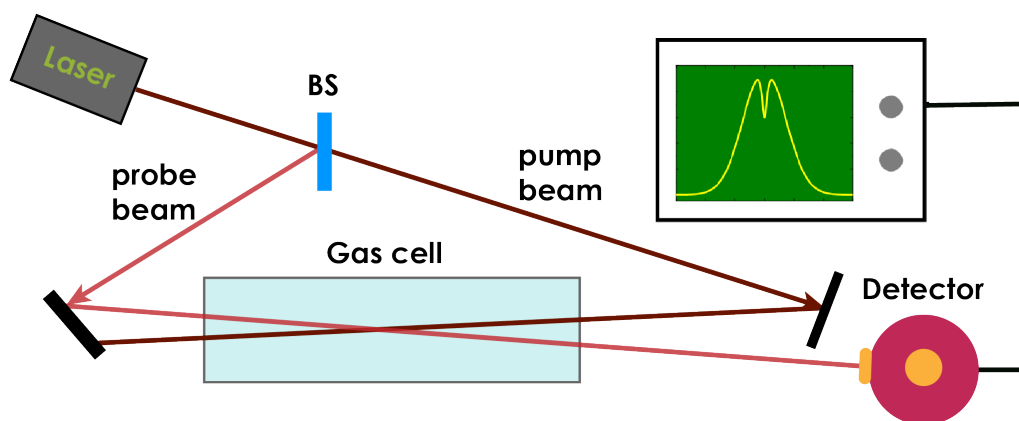


Figure 1.3: **Saturation spectroscopy classical setup:** The beam splitter (BS) splits the main beam in the transmitted pump beam and the reflected probe beam. The pump beam saturates the gas sample and a Lamb dip is observed on the Doppler-broadened absorption profile.

the Doppler width but only by the much narrower width of the Lamb dip. For this reason, it is also known as *Lamb-dip spectroscopy*. The saturation spectroscopy typical scheme is shown in Fig.1.3.

1.2.2 Feedback control techniques for high-resolution spectroscopy

In order to perform high-resolution spectroscopy, very narrow and stable (low frequency noise) sources are required. Quantum cascade lasers (QCLs) are eligible to those applications where a powerful and reliable mid-IR source is required. For instance, most chemical compounds have their fundamental absorption bands in the mid-IR region of the electromagnetic spectrum, thus making this range of paramount importance for gas sensing and spectroscopic applications. QCL is a current-driven semiconductor laser based on intersubband transitions in quantum wells [6]. QCLs are based on a complex super-lattice made of different cells, each of them made of a series of quantum wells. In particular, each cell (or period) is divided into two regions, an active region and a relaxation-injection region (Fig. 1.4). In the active region population inversion is maintained by the current flux due to the externally-applied electric field. Here three levels, which are sublevels of the electronic conduction band, are present. The electrons are injected in level 3 (the highest in energy) and the population inversion is maintained between level 3 and level 2. The injection region must essentially drive the electrons from level 1 of the preceding gain region to level 3 of the following one, matching the energies. The transition occurs through resonant tunneling. A portion of this region is doped with electron donors, in order to provide the carriers. The structure is ordered in an alternate cascade of active and relaxation-injection regions. The externally applied electric field pro-

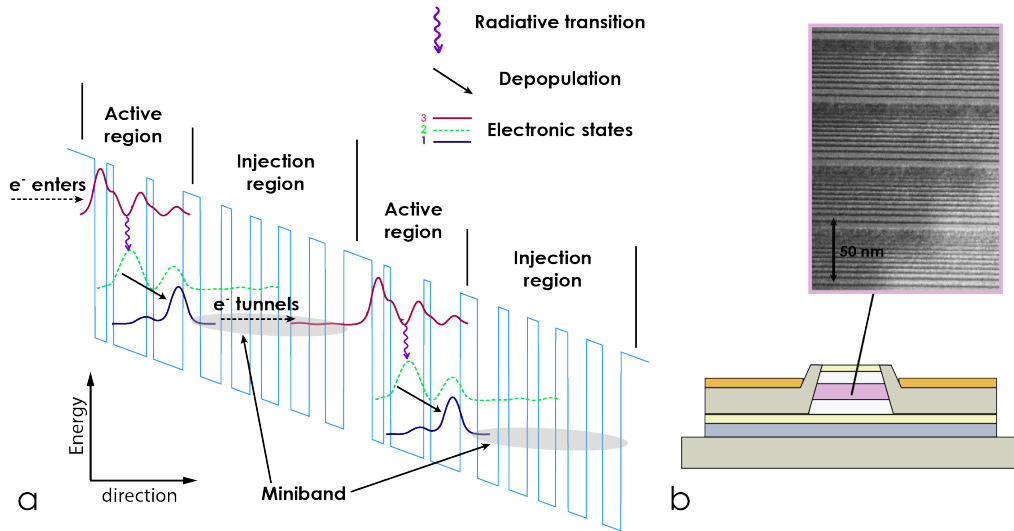


Figure 1.4: **Quantum Cascade Laser scheme:** (a) band diagram of two stages of the cascaded quantum well structure of a QCL with each stage consisting of an active and an injector region. Radiative transitions occur between states 3 and 2 in the active regions. Population inversion is maintained after rapid depopulation of lower state 2 into state 1 which couples strongly with the minibands formed in the injection regions that facilitate electron-tunnelling to state 3 in the next stage. (b) TEM image of a partial section of the active region in a 3-quantum well design QCL.

vides the needed potential energy to the electrons. The advantages of this cascade structure are the decreased density required for each individual active region, with the consequent reduction of the threshold current density, and the potential for many transitions to recycle the same electrons. Indeed this region also provides an “electron reservoir” that will feed the carriers to the next period. Until now, QCLs are the best-performing lasers in the mid-IR and terahertz wavelength region, in terms of reliability and power combined with tunability. For this reason they are fundamental tools for molecular spectroscopy. The QCL provides several key advantages for practical applications: it enables the design of semiconductor lasers for the first time from the same technologically mastered, large-bandgap semiconductor material such as GaAs/AlGaAs or InGaAs/AlInAs/InP in a very wide operating wavelength range in the mid IR. Moreover, it is among the best mid-IR semiconductor lasers to operate at room temperature, being based on a radically different operating mechanism. Mid-IR QCL sources are particularly well adapted for chemical spectroscopy in both atmospheric [7] and medical applications [8]. Moreover, QCLs are becoming a key tool in several advanced experiments in the field of precision molecular spectroscopy and absolute frequency metrology. In view of this, a thorough control of their emission properties must be achieved, including a narrow linewidth as well as a high frequency stability, combined with referencing to a primary standard.

Narrow-linewidth CW lasers have played, and continue to play, a major role in advancing pre-

recision measurements in many fields of science. The “free-running” linewidth, or short-term stability of the laser, is often not adequate for many applications without active stabilization of the laser frequency. Some techniques were developed to realize stable and narrow sources. The noise intrinsic to the laser can be characterized in terms of the linear spectral density of frequency fluctuations, defined as the RMS frequency fluctuations per per square-root unit bandwidth. The free-running linewidth and noise spectrum of different lasers can vary greatly depending on the stability and finesse of the resonator design, gain-medium characteristics, and other laser parameters. The spectral density of frequency noise is often dominated by pump and mechanical fluctuations, which generally fall off as $\sim 1/f$ and can be greatly suppressed by an active locking loop. Moreover, the dominant frequency/phase noise in many diode laser systems is often of a quantum nature due to larger spontaneous emission rates, resulting in significant noise processes extending out to higher Fourier frequencies. To detect and actively reduce fluctuations in the laser frequency, a highly stable reference is needed for comparison. To achieve this, the two common ways are: using a molecular transition or a high-finesse Fabry-Pérot cavity, designed to provide the necessary stability over the time scale of interest.

1.2.3 Polarization spectroscopy for frequency-lock

In light of what described, saturation spectroscopy monitors the decrease of the absorption of the probe beam following the interaction of the pump beam which has saturated (depleted) the absorbing level. Instead, signals in polarization spectroscopy (PS) are generated by the change of the linearly polarized probe wave induced by a circularly polarized pump beam, which leads to both a change in the absorption coefficient α and a change in the refraction index n . Let us assume that a molecular ro-vibrational transition belonging to the R or P branch is the transition involved. If the pump beam is σ^+ polarized, the selection rule on the projection of the angular momentum J states $\Delta M = +1$. This ensures that the pumping process induces an unequal saturation and therefore a non-uniform M sub-level population, which is analogous to an anisotropic distribution for the orientation of the angular momentum vector \vec{J} . Such an anisotropic sample becomes birefringent for the incident linearly polarized probe beam. Since the two balanced circularly polarized components, σ^+ and σ^- , are unbalanced by an induced birefringence, the result is a probe beam with a rotated polarization. To detect the probe beam when the polarization is rotated, a polarizer is added before the detector with a transmission axis perpendicular to the polarization one of the unperturbed probe beam. This effect only occurs for those molecules which are resonant with both beams simultaneously, i.e. when the laser frequency ω coincides with the center frequency ω_0 of the molecular transition within its γ homogeneous linewidth ($\omega = \omega_0 \pm \gamma \Rightarrow \nu_z = 0 \pm \Delta\nu_z$) [5]. To understand the line profile of a polarization signal, we consider that a linearly polarized probe wave can be decomposed as the sum of two opposite

circularly polarized components $E = E^+ + E^-$

$$E^+ = \frac{1}{2}E_0^+(\hat{x} + i\hat{y})e^{i(\omega t - k_+ z)} \quad (1.31)$$

$$E^- = \frac{1}{2}E_0^-(\hat{x} - i\hat{y})e^{i(\omega t - k_- z)} \quad (1.32)$$

where \hat{x} and \hat{y} are the polarization versors. While passing through the birefringent sample, the two components experience different absorption coefficients α^+ and α^- and different refractive indices n^+ , n^- from the nonisotropic saturation caused by the σ^+ -polarized pump wave. After a path length L through the pumped region of the sample, the two components become:

$$E^+ = E_0^+(\hat{x} + i\hat{y})e^{i(\omega t - k_+ L + i(\alpha^+/2)L)} \quad (1.33)$$

$$E^- = E_0^-(\hat{x} - i\hat{y})e^{i(\omega t - k_- L + i(\alpha^-/2)L)} \quad (1.34)$$

Since $\Delta n = n^+ - n^-$, the non-isotropic saturation gives a phase difference

$$\Delta\phi = (k^+ - k^-)L = \frac{\omega L}{c}\Delta n \quad (1.35)$$

and, an amplitude difference:

$$\Delta E = \frac{E_0}{2}[e^{-(\alpha^+/2)L} - e^{-(\alpha^-/2)L}] \quad (1.36)$$

assuming to be in the case of linear polarization, $E_0^+ = E_0^- = E_0$. Behind the exit window the two components (σ^+ , σ^-) of the linearly polarized probe wave traveling into the direction ($z = L$) yields the elliptically polarized wave:

$$E(L) = E^+ + E^- = \frac{1}{2}E_0 e^{-i[\omega n L/c - i\alpha L/2]}[(\hat{x} + i\hat{y})e^{-i\Lambda} + (\hat{x} - i\hat{y})e^{i\Lambda}] \quad (1.37)$$

with $n = (n^+ + n^-)/2$, $\alpha = (\alpha^+ + \alpha^-)/2$, and the phase factor

$$\Lambda = \frac{\omega L \Delta n}{2c} - i \frac{L \Delta \alpha}{4} \quad (1.38)$$

where $\Delta\alpha = \alpha_+ - \alpha_-$. If the transmission axis of the analyser is tilted by the small angle $\theta \ll 1$ relatively to the y -axis, then

$$E_t = E_x \sin\theta + E_y \cos\theta \quad (1.39)$$

Since for $\theta \ll 1$, $\cos\theta \sim 1$ and $\sin\theta \sim \theta$, the transmitted amplitude is:

$$\begin{aligned} E_t &= E_0 \exp\left[-i\left(\frac{\omega nL}{c}\right) - \left(\frac{i\alpha L}{2}\right)\right](\sin\theta \cos\Lambda + \cos\theta \sin\Lambda) \\ &= E_0 \exp\left[-i\left(\frac{\omega nL}{c}\right) - \left(\frac{i\alpha L}{2}\right)\right](\sin\theta + \Lambda) \end{aligned} \quad (1.40)$$

The detector signal $S(\omega)$ is proportional to the transmitted intensity

$$S(\omega) \propto I_T(\omega) = c\epsilon_0 E_t E_t^* \quad (1.41)$$

As it was for saturation spectroscopy, the change of absorption $\Delta\alpha$ is caused for those molecules within $\Delta\nu_z = 0 \pm \gamma_s/k$ that simultaneously interact with the pump and probe beams. The line profile of $\Delta\alpha(\omega)$ is Lorentzian, therefore we can define:

$$\Delta\alpha(\omega) = \frac{\Delta\alpha_0}{1+x^2}, \quad x = \left(\frac{\omega_0 - \omega}{\gamma_s/2}\right) \quad (1.42)$$

The absorption coefficient $\alpha(\omega)$ and the refractive index $n(\omega)$ are related by the Kramers-Kronig dispersion relations 1.14. Therefore, the dispersion profile is:

$$\Delta n(\omega) = \frac{c}{\omega_0} \frac{\Delta\alpha_0 x}{1+x^2} \quad (1.43)$$

Starting from 1.42, 1.43 and expanding them we obtain the detected signal

$$I_t(\omega) = I_0 e^{\alpha L} \left[\theta^2 + \theta \Delta\alpha_0 L \frac{x}{1+x^2} + \left(\frac{\Delta\alpha_0 L}{4}\right)^2 \frac{1}{1+x^2} + \frac{3}{4} \left(\frac{\Delta\alpha_0 x}{1+x^2}\right)^2 \right] \quad (1.44)$$

where $\theta \Delta\alpha_0 L \frac{x}{1+x^2}$ is a dispersive term and $\left(\frac{\Delta\alpha_0 L}{4}\right)^2 \frac{1}{1+x^2}$ is a Lorentzian contribute. The dispersive term is centered around ω_0 and its magnitude depends on the θ angle. Tuning properly this angle allows to minimize the dispersive term. The constant term proportional to θ gives a background to the signal, it is possible to get rid of this background by rotating the analyser of $\theta \sim \pi/4$ and subtracting both the transmitted and the reflected components in a differential-detection scheme [9]. A laser cavity is generally subject to various perturbations, consequently the stability of a single-mode laser can be improved by electronically locking its frequency to some passive reference cavity. PS has already proven to be an effective technique to obtain a narrow-emission and absolutely-referenced QCL [9] [10]. A PS scheme produces, without any external modulation, a narrow dispersive sub-Doppler signal used to close the feedback loop on the QCL driving current for frequency stabilization. It will be shown in Sec. 3.3 that the linewidth of a CW room temperature QCL can be narrowed below 1 kHz (FWHM) by locking the laser to a molecular line. In Sec. 3.3.2 it will be exploited the availability of a natural

frequency references given by the many strong molecular absorption lines, whose center frequency can be absolutely measured with a sub-kHz precision.

1.2.4 Pound-Drever-Hall (PDH) technique for frequency-lock

The adoption of high-finesse Fabry-Pérot (F-P) cavities requires techniques able to improve the frequency stabilization of the laser, since both the frequency of the laser and the length of the cavity vary continuously depending on a range of factors like ambient temperature, injection current and mechanical vibration. Since the laser light, sent to a cavity, is transmitted, absorbed and reflected, Pound-Drever-Hall (PDH) locking uses the reflected beam to generate an error signal that can be used to make small correction to either the length of the cavity or the frequency of the laser, so that the resonance condition is held and transmission is maximized [11]. PDH laser frequency stabilization is a powerful technique to improve the frequency stability of a laser source and was first introduced by R.V. Pound, R. Drever, and J. L. Hall in 1983 [12]. Let us consider a laser with frequency ν , perfectly mode-matched to the F-P cavity, that we want to tune on a cavity resonance. The difference between the two frequencies $\delta\nu$ can be monitored by observing the reflection from the F-P cavity. When the laser frequency is far from cavity resonance, all light is reflected by the cavity. When it is near resonance the reflection coefficient F , depends on $\delta\nu$, vanishing when $\delta\nu$ is zero. The cavity F coefficient is symmetric around resonance, it means that it is not possible to directly use this signal to lock the laser frequency to the cavity mode. However, the derivative of F with respect to $\delta\nu$ is antisymmetric across resonance. By comparing the variation in the reflected intensity with the frequency variation we can tell which side of resonance we are on. Therefore, an error signal proportional to the frequency offset, which indicates the side of the cavity resonance, can be generated. To determine the derivative at any point, one can simply vary the frequency slightly and see how the reflected intensity responds [11]. With a similar approach described before, the PDH technique uses a photodetector to capture the reflected light, which has been modulated, and mixes its photocurrent with a local oscillator (LO) before passing it through a low-pass filter. It provides an unambiguous indication of not only how far the system is from resonance but in which direction adjustments must be made to restore resonance. The readout signal is then sent in a proportional-integral-derivative (PID) controller to generate an error signal which can be used to correct the laser-cavity relative detuning, for instance by modifying the laser driving current, or by changing the length of the cavity by means of a piezoelectric actuator.

1.3 High-sensitivity spectroscopy

Determination of the absorption coefficient $\alpha(\omega)$ from spectral intensity allows to measure absorption spectra. The transmitted power through an absorbing path length x , is

$$P_T(\omega) = P_0 e^{-\alpha_{ik}(\omega)x} \quad (1.45)$$

where $\alpha_{ik}(\omega)$ is the absorption coefficient of the transition $|i\rangle \rightarrow |k\rangle$ with σ_{ik} cross-section determined by the density N_i of the absorbing molecules.

$$\alpha_{ik}(\omega) = [N_i - (g_i/g_k)N_k]\sigma_{ik}(\omega) = \Delta N\sigma_{ik}(\omega) \quad (1.46)$$

If the population $N_k \ll N_i$, from Eq. 1.45 and 1.46 we obtain for the density N_i of absorbing molecules in level $|i\rangle$ over the absorption path length $x = L$:

$$N_i = \frac{\Delta P}{P_0 L \sigma_{ik}} \quad (1.47)$$

This approximation is true if and only if $\Delta L \ll 1$. Since the absorbed power ΔP has to be larger than the noise power P_N , the minimum detectable molecular density is obtained:

$$N_i > \frac{P_N}{P_0 L \sigma_{ik}} \quad (1.48)$$

It is clear that the minimum detectable concentration of absorbing molecules is a function of the noise power, the absorption path length, the absorption cross-section and the incident radiation power. In order to reach a high detection sensitivity for absorbing molecules, L, σ_{ik}, P_0 should be large and the noise power as small as possible.

1.3.1 Cavity-enhanced absorption methods

With *Cavity-enhanced absorption* we refer to all spectroscopic methods exploiting the main property of a high-finesse optical cavity, i.e. the increase of the light-matter interaction time [13]. An optical cavity is also referred to as an optical resonator, since the electromagnetic field inside the cavity increases in amplitude for incident light at resonant frequencies and optical cavities have always been associated with sensitive measurements in physics. High-sensitivity measurements are hindered by a too short interaction path length of the light beam through the sample, or by too high amplitude and/or frequency fluctuations of the laser source. Multiple-pass cells provided the most intuitive solution for increasing the interaction length, but when hundreds of passes are needed, their implementation turns out to be technically complex. Their challenging optical alignment involves highly stable mechanics. In order to minimize the detrimental effects of optical interference between neighbouring reflections,

large mirrors and, consequently, large sample volumes are required. Optical cavities provide an elegant and compact solution for these different problems. The increase of the light-matter interaction time in a high-finesse optical cavity can correspond to an effective interaction length of thousands of passes. In addition, the measurement of the cavity decay time (ring-down signal) provides access to the absorption of the intra-cavity sample regardless of the amplitude fluctuations of the source. Finally, in a high-finesse cavity, the sample size is limited by the TEM₀₀ mode size, which is smaller than the volume needed by a multi-pass device.

1.3.2 High-finesse optical resonator

High-sensitivity spectroscopy is based on the use of optical cavities in order to increase light interaction with matter present inside the cavity. Considering the fundamental transverse modes TEM₀₀, they are uniformly separated in frequency by the Free Spectral Range (FSR) of the cavity

$$FSR = \frac{c}{2n_g L} = t_r^{-1} \quad (1.49)$$

where t_r^{-1} is the reciprocal of the round trip time, L is the cavity length and n_g is the refraction index of the intra-cavity medium. We may assume a symmetric linear cavity made by two facing mirrors at distance L along the optical axis z . A monochromatic Gaussian laser beam is mode-matched to the cavity, when it matches in waist size and position the TEM₀₀ mode of the cavity. Since the TEM₀₀ modes are unchanged after propagating inside the cavity, we can express the field transmitted by the empty cavity (when $n_g = 1$) as:

$$E_{out} = E_0(x, y) \sum_{p=0}^{\infty} \mathbf{t}^2 \mathbf{r}^{2p} e^{i\omega(t-2pL/c-L/c)-ikz} \quad (1.50)$$

$$= \frac{\mathbf{t}^2 e^{-i\omega t_r/2}}{1 - \mathbf{r}^2 e^{-i\omega t_r}} E_{in}(x, y, z, t) \quad (1.51)$$

where $E_{in} = E_0(x, y) e^{i(\omega t - kz)}$ \mathbf{t} and \mathbf{r} are the transmission and reflection coefficients (for the field) of each cavity mirror, whose square modulus corresponds, respectively to T and R coefficients for the light intensity. The transmitted intensity can be expressed by Airy formula, as follows:

$$I_{out}(\omega) = \frac{T^2}{|1 - R e^{-i\omega t_r}|^2} I_{in} \quad (1.52)$$

$$= \frac{T^2}{(1 - R)^2} \frac{I_{in}}{1 + \left(\frac{2\sqrt{R}}{1-R}\right)^2 \sin^2(\omega t_r/2)} \quad (1.53)$$

The transmitted intensity at the resonant frequency is well approximated by a Lorentzian

function. The FWHM of this resonance $\Delta\nu$ and the cavity finesse \mathfrak{F} can be expressed as:

$$\Delta\nu = \frac{1}{\pi t_r} \frac{1-R}{\sqrt{R}} \quad (1.54)$$

$$\mathfrak{F} = \frac{FSR}{\Delta\nu} = \pi \frac{\sqrt{R}}{1-R} \quad (1.55)$$

There, the relation between $\Delta\nu$ and the photon lifetime in the cavity, the ring-down time τ , can be derived. This is mathematically obtained by considering the cavity time response to an impulsive excitation which is written as the convolution of the pulse time profile and the Fourier-Transform (FT) of Eq. 1.50 taken for $r \sim 1$. Taking a delta function for the pulse, we obtain an exponential decay for the field. Switching to the intensity ($I = |E|^2$), the decay becomes twice as fast and we find that the ring-down time is inversely proportional to the cavity mode width (which is related to the time-frequency uncertainty relation of FT theory):

$$\tau = \frac{1}{2\pi\Delta\nu} = \frac{L\sqrt{R}}{c(1-R)} \quad (1.56)$$

the ring-down time is proportional to cavity finesse and to cavity length. It should be noted that a direct derivation of the ring-down time, by considering the cavity losses per round trip, yields the same result except for the term \sqrt{R} which is missing.

1.3.3 Cavity ring-down spectroscopy

Cavity ring-down spectroscopy (CRDS) is an established spectroscopic technique which allows high-sensitivity, direct, and accurate measurements of gas-phase molecules [14]. The first CRDS devices were designed to measure low levels of optical loss in highly reflective mirrors. By coupling a pulsed laser into a high-finesse Fabry-Pérot cavity formed by these mirrors, it was possible to measure changes in reflectivity on the order of parts per million. O'Keefe and Deacon realized that the cavity could also be filled with an absorbing analyte, indeed they obtained the spectrum of a weak magnetic-dipole transition in atmospheric oxygen [15]. One of the main advantages of the CRDS technique is that the measurement parameter is in the time domain. Therefore, the resulting measurement is independent of the intensity fluctuations of the incident light, which further improves the signal-to-noise ratio of the measurements. The basic principle of CRDS lies in the substantial enhancement of the optical path length through the sample of interest, which can increase the actual sample length by about a thousand times. This is achieved by creating a high-finesse optical cavity consisting of high-reflectivity mirrors, which trap the incident light and therefore allow multiple reflections inside the cavity. The optical cavity is suitably aligned to form stable cavity modes which, when matched with the laser mode, generate a resonant signal. The basis of the cavity ring-down technique consists in the measurement of the decay of light intensity

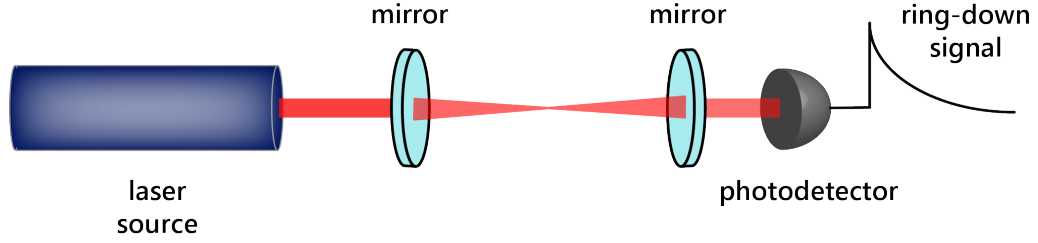


Figure 1.5: **Schematic of the experimental setup for a cavity ring-down spectroscopy.** Two high reflectivity mirrors, a laser providing the input beam and a detector measuring the small amount of light leaking out from the cavity to collect the ring-down signal of decay rate.

coupled into a high-finesse optical cavity. The light is sent along the cavity axis toward the back face of the input mirror, and the small amount of light coupled through this mirror into the cavity undergoes repeated reflections between the two mirrors. A small fraction of light is lost on each round-trip of the cavity, due to both mirror transmission/absorption/scattering and absorption from the intra-cavity medium, with the result that the light intensity within the cavity decays exponentially with time.

The intensity of the leak-out light from the optical cavity is given by the following equation:

$$I(t) = I_0 e^{-\frac{t}{\tau}} \quad (1.57)$$

where I_{in} and I_0 are respectively the incident and the output intensities and τ is the time required for the light signal to decay to $1/e$ of its initial output intensity and it is called, as seen, the *ring-down time* τ . The equation to calculate τ can be derived from the Beer-Lambert law:

$$I_0 = I_{in} e^{-\alpha L} \quad (1.58)$$

with α attenuation coefficient of the absorbing sample and L the path length within the cavity. Let R and T be the reflectivity and the transmission of the mirrors. If the duration of the laser pulse is smaller than the round-trip time in the resonator (a ballistic assumption) the output signal will consist of a number of pulses with gradually decreasing intensity because of leakage of light intensity from the imperfect mirrors at each reflection of the pulse [16]. When a light beam is incident on the cavity, the output intensity I_0 after single pass is:

$$I_0 = I_{in} T^2 e^{-\alpha L} \quad (1.59)$$

After one round trip of the cavity, the light has suffered two reflections and the new output intensity becomes:

$$I_1 = I_0 R^2 e^{-2\alpha L} \quad (1.60)$$

After n round trips of light inside the cavity, the Eq. 1.60 will be:

$$I_n = I_0 R^{2n} e^{-2n\alpha L} \quad (1.61)$$

R^{2n} can be expressed as $\exp(2n \ln R)$ and $R \sim 1$ for high-reflectivity mirrors which gives $\ln R \sim -(1 - R)$ and Eq. 1.61 becomes:

$$I(t) = I_0 e^{-2n(1-R+\alpha L)} \quad (1.62)$$

The discrete variable n can be changed to a continuous time variable $t = 2nL/c$, where t is the time taken to complete n round trips. Comparing Eq. 1.57 and 1.62 we derive the ring-down time τ in the presence of absorbing sample:

$$\tau = \frac{L}{c[(1-R) + \alpha L]} \quad (1.63)$$

where α is the absorption coefficient of an absorbing species present at concentration C over a path length L within the cavity. In the absence of any sample inside the cavity, the ring-down time is expressed as the empty cavity ring-down time τ_0 which is the characteristic parameter of a CRDS system.

$$\tau_0 = \frac{L}{c(1-R)} \quad (1.64)$$

The exponential decay may be recorded by positioning a sensitive photo-detector behind the output mirror to detect the light leaking out through this mirror on each pass. Apart from constants of the experimental setup, such as the length of the cavity and the intrinsic cavity losses, the only parameters that determine the ring-down time are the absorption coefficient and, consequently, the concentration of the sample. By recording the ring-down time in the presence and absence of the sample (τ and τ_0 , respectively), the absorption per unit path length α , can be determined, yielding the concentration C if the absorption coefficient is known at the wavelength of interest.

$$\alpha = \frac{1}{c} \left(\frac{1}{\tau} - \frac{1}{\tau_0} \right) \quad (1.65)$$

From what described before, it becomes evident that the absorption coefficient α can be measured by a technique able to discriminate the smaller gas-induced decay rate $\gamma_g = c\alpha$ (full cavity), on top of the much larger background cavity loss decay rate $\gamma_c = 1/\tau_0$ (empty cavity). The sensitivity of the CRDS technique can be expressed as the minimum detectable absorption coefficient α_{min} expressed as:

$$\alpha_{min} = \frac{1}{c\tau_0} \frac{\Delta\tau_{min}}{\tau_0} \quad (1.66)$$

where $\Delta\tau_{min}$ is the minimum measurable variation in the ring-down time τ .

It is known that the coupling of the laser to a cavity mode affects the SNR; when the laser mode profile is Gaussian and the cavity alignment is on-axis to excite only the TEM₀₀ modes in the cavity, a strong mode coupling can be achieved in CRDS. Some critical aspects of the technique are related to the high-reflectivity mirrors used in CRDS. They are available in a narrow wavelength range, which limits the working spectral range for a particular set of cavity mirrors. Moreover, to achieve the mode-matching condition, a precise alignment of the cavity is needed because the instability of the incoming laser beam direction and shape may affect the detection of the CRDS signal. Improvements in terms of sensitivity and resolution with respect to pulsed CRD are achieved in CW-CRDS. In CW-CRDS only one longitudinal mode of the high-finesse non-degenerate Fabry-Pérot cavity is excited in shorter build-up times, which means a more efficient cavity coupling than the early-developed pulsed version [15]. If the intra-cavity medium response is linear, a simple exponential decay is observed. Moreover, in CW-CRDS lower shot-to-shot ring-down rate fluctuations are measured comparing to pulsed CRD. In addition, the narrower linewidth of CW coherent sources allows also sub-Doppler resolution in CW-CRDS. An important aspect of CW-CRDS is that it is possible to use high intra-cavity power to detect non-linear effects such as two-photon transitions or saturated absorption (e.g. sub-Doppler Lamb dips) [17].

1.3.4 Sensitivity Limits of CW-CRDS

After the development of CW laser sources, such as the above described QCL, it was demonstrated that CW-CRDS is particularly appealing in the mid-IR spectral region, where the strongest ro-vibrational transitions lie, belonging to the so-called *fingerprint region*. Indeed, its sensitivity with short averaging time places CRDS among the simplest quantitative methods, since it allows direct determination of the absolute value of the absorption coefficient α without any need for complex calibration routines. It is worth to mention that sensitivity can be enhanced by a proper optimization of the trigger level and the fitting interval [18]. In that condition the optimized sensitivity can be comparable with high-sensitive spectroscopic techniques such as noise-immune cavity-enhanced optical heterodyne molecular spectroscopy (NICE-OHMS).

Nonetheless, in conventional CRDS, cavity losses are added to the linear absorption from the sample which is measured from the increase of the cavity decay rate with respect to the non-absorbing sample condition. Therefore, accurate and independent measurements of the empty-cavity loss spectrum, in order to retrieve the zero-absorption baseline, are required. Sensitivity depends on both precision in measuring the empty-cavity decay rate (γ_c) and the repeatability and stability of these measurements.

The main observed factors which worsen the shot-to-shot γ_c fluctuations are related to defects of the cavity mirrors such as coating non-uniformity, surface defects and dirty spots. Moreover, fluctuations of the laser alignment, excitation of transverse modes nearly degenerate with

longitudinal ones may further worsen γ_c stability for CW-CRDS [14]. An usual strategy of CRDS is the use of consecutive $1/\tau$ measurements at different laser frequencies, one in resonance with the targeted absorption transition and one out of resonance, in order to directly determine the sample absorption contribution by difference. At the same time, frequency independent $1/\tau$ instabilities could be cancelled out or minimized by taking such difference. Unfortunately, low repeatability of the measured $1/\tau$ prevents sensitivity increase by using long-time averages. Determination of this frequency-dependent baseline can be even more dramatic when a background from other absorbing substances present in the sample is added. The sensitivity limits due to uncorrelated fluctuations of the cavity decay rate suggested us to follow a totally different approach to decouple other cavity losses from the targeted absorption loss in the shortest possible time, i.e. in a single CRD event, approaching, in this way, the ultimate shot-noise-limited sensitivity. *Saturated-absorption cavity ring-down* (SCAR) spectroscopy overcomes limits due to shot-to-shot fluctuations of the cavity decay rate by measuring both γ_c and γ_g , in a single CRD event.

1.3.5 Saturated-absorption cavity ring-down spectroscopy

From the experimental point of view, SCAR does not differ from other conventional CRD experiments. The laser light is coupled to the high-finesse Fabry-Pérot cavity up to a threshold level, and then it is quickly switched off at the cavity resonance. Transmitted light during the ring-down time is detected and the decay rate is measured. If a molecular species inside the cavity absorbs coupled light, it increases the empty cavity loss rate, and such loss rate increase is measured. The difference with the conventional CW-CRDS is that in SCAR saturation effects of the molecular absorption induce a deviation of the ring-down signal from the perfectly exponential behaviour, as expected for linear intra-cavity losses. When the ring-down signal that contains saturated molecular absorption is fitted to an exponential function, the residuals strongly differ from a flat behaviour. Fig. 1.6 shows an experimental SCAR decay that recorded by averaging 3072 decay signals measured at a fixed frequency close to the center of the ($03^3_1-03^3_0$) R(50) transition of $^{12}\text{C}^{16}\text{O}_2$ (line-center frequency 2343.663 cm^{-1}), with cavity length of 1 m, and gas temperature and pressure of 296 K and 50 μbar , respectively [19]. Let us consider the saturation parameter $G(t)$, the following equation gives flat residual plot and explain the physical effect of the saturated molecular transition:

$$\frac{dG}{dt}(t) = -\gamma_c G(t) - \gamma_g \frac{2G(t)}{1 + \sqrt{1 + G(t)}}, \quad G(0) = G_0 \quad (1.67)$$

$\gamma_c = c(1 - R)/L$ where R is the mirror reflectivity and L is the cavity length, while $\gamma_g = c\alpha_0$ where α_0 is the non-saturated value of the absorption coefficient of the absorbing species. They represent the cavity and molecular absorption decay rates, respectively. $G_0 = P_0/P_S$ is the saturation parameter value when the SCAR decay event starts, triggered by a threshold level reached on the F-P transmitted signal. An analytical solution $G = G(t)$ of

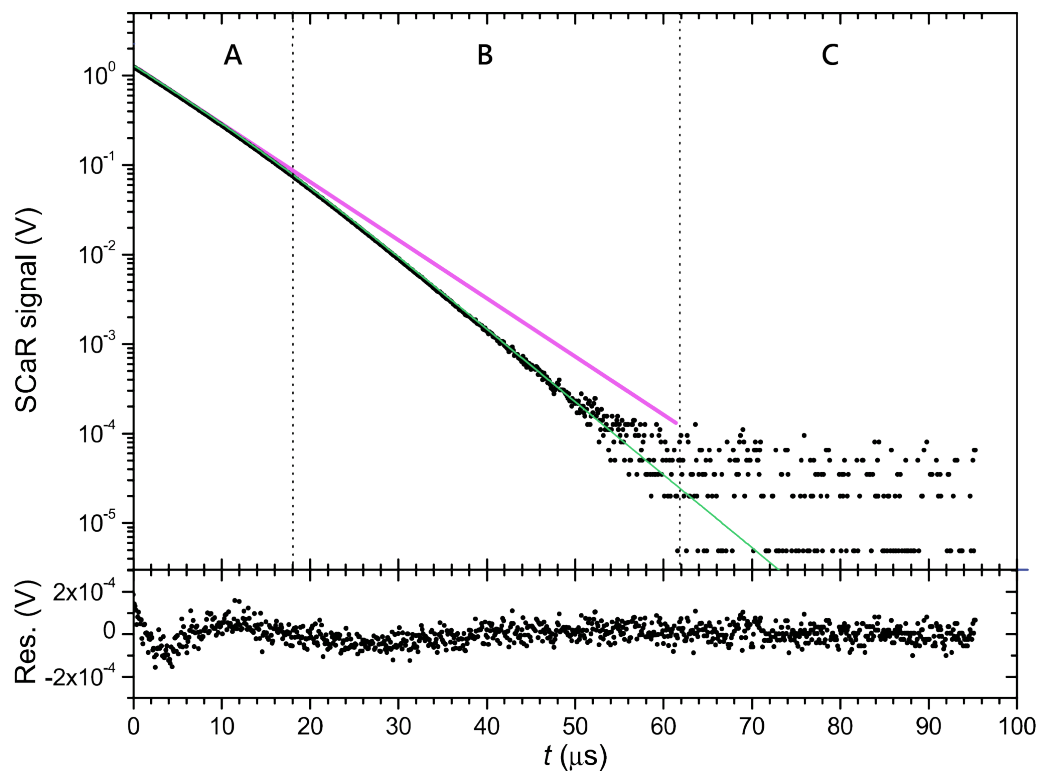


Figure 1.6: **Typical SCaR decay signal.** Three consecutive time intervals can be recognized: zones A, B, and C carry information, respectively, on γ_c , $\gamma_c + \gamma_g$ and the detection offset, which in the IR region is due to thermal background.

this differential equation cannot be found even by explicitly inverting the solution $t = t(G)$. An alternative way consists in performing a numerical integration by using the 4th-order Runge-Kutta algorithm (RK4) as a step of the fitting procedure. Since in real CRD molecular spectroscopy experiments $\gamma_g < \gamma_c$ we can factorize G as follows:

$$G(t) = G_0 e^{-\gamma_c t} f(t; G_0, \gamma_c, \gamma_g) \quad (1.68)$$

By substitution in Eq. 1.67, we obtain the saturated decay function f , which gives a rough and intuitive explanation for the intrinsic ability of the SCAR technique to improve sensitivity by distinguishing between gas absorption losses and cavity ones.

$$\frac{df}{dt}(t) = -\gamma_g \frac{2f(t)}{1 + \sqrt{1 + G_0 e^{-\gamma_c t} f(t)}}, \quad f(0) = 1 \quad (1.69)$$

Numerical integration of Eq. 1.69 and G factorization in Eq. 1.68 can be used for a better computing precision of the fitted parameters G_0, γ_c, γ_g .

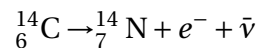
2

Radiocarbon: its cycle and its detection

In this chapter, we present radiocarbon (^{14}C), the rarest isotope of carbon. During their lifetimes, plants and animals, through the food chain, assimilate ^{14}C from atmospheric carbon dioxide. After the death of the organism, carbon is not any more shared with the biosphere and their radiocarbon content starts to decrease at a rate determined by the law of radioactive decay. Radiocarbon dating is a method designed to determine the age of biogenic materials by measuring their residual content of ^{14}C . Radiocarbon has grown far beyond Willard Libby's initial conceptualization as a tool for age determination. At the same time, current uses of radiocarbon for understanding the Earth system build upon the solid foundation laid down by several generations of scientists who worked tirelessly using this unique isotope. While it is not possible to present the entire scope of radiocarbon research, this chapter intends to create a short know-how to understand the role of radiocarbon isotope when addressing the human impact on global carbon cycle and its feedbacks on climate change and Earth system science.

2.1 Carbon Isotopes

Atomic nuclei with the same number of protons (atomic number) and different number of neutrons are called isotopes. Isotopes of an element have the same chemical behaviour because they possess the same number of electrons. Different isotopes have different masses so the bonds they form have slightly different strengths. Carbon has three isotopes which occur naturally: the most abundant is ^{12}C , accounting for 99.89 % of the C atom on the Earth, almost all the remaining 1.11% is ^{13}C with 6 protons and 7 neutrons, both are stable isotopes [20]. *Radiocarbon* (^{14}C) is the radioactive isotope of C, with 6 protons and 8 neutrons. It is a cosmogenic radionuclide, which means it is constantly being created by the interaction of cosmic rays with the Earth's atmosphere. The nucleus of ^{14}C is unstable and will spontaneously decay (half-life $\tau_{1/2} = 5700 \pm 30$ years) with the following nuclear reaction:



^{14}C is produced in the stratosphere as a spallation product when cosmic rays interact with the Earth's atmosphere [21]. Cosmic protons, that are not deflected by the Earth's magnetic field, form neutrons by interaction in the upper atmosphere with nitrogen and atmospheric oxygen via spallation reactions. Through multiple collisions, the neutrons are slowed down to the energy corresponding to the atmospheric temperature. Under these conditions, the capture reaction by the ^{14}N occurs, giving rise to an unstable ^{15}N atom, which decays, with the emission of a proton, to ^{14}C . During its cycle of production and decay, radiocarbon is oxidized to $^{14}\text{CO}_2$, it is diffused by the stratospheric winds into the troposphere and enters in the global C cycle that exchanges C between atmosphere, land and oceans (Fig. 2.1). However, since there is a variation in the cosmic radiation flux, the overall output in this reaction is not constant. Furthermore, the Earth's magnetic field changes course and intensity slightly over time. Consequently, this makes the amount of cosmic radiation colliding with the atmosphere to fluctuate [22]. The natural abundance of ^{14}C in the pre-industrial atmosphere was approximately one in every trillion (10^{12}) C atoms (an abundance of 1 ppt). Through production of new ^{14}C atoms in the upper atmosphere, the loss of ^{14}C atoms due to radioactive decay is balanced. This essential feature gives rise to the unique attribute of ^{14}C . It is redistributed as a "stable" isotope among reservoirs and also acts as a clock because of the regularity of radioactive decay. This seminal discovery by Willard Libby and colleagues led to the Nobel Prize in Chemistry in 1960 [23].

The biosphere works as a reservoir that absorbs ^{14}C in the form of CO_2 . It is fair to assume that the ^{14}C content of the biosphere is the same as that of the atmosphere, but it is true only for terrestrial plants, although slightly different due to isotope fractionation. Since plants use photosynthesis to grow, the growth reflects carbon absorption from the atmosphere, and hence ^{14}C absorption. Consequently, the ^{14}C concentration in a plant can be compared, after death, to the atmospheric radiocarbon concentration during the growth period. Crops or similar plants are fed to livestock. Since the carbon absorption by animals originates from

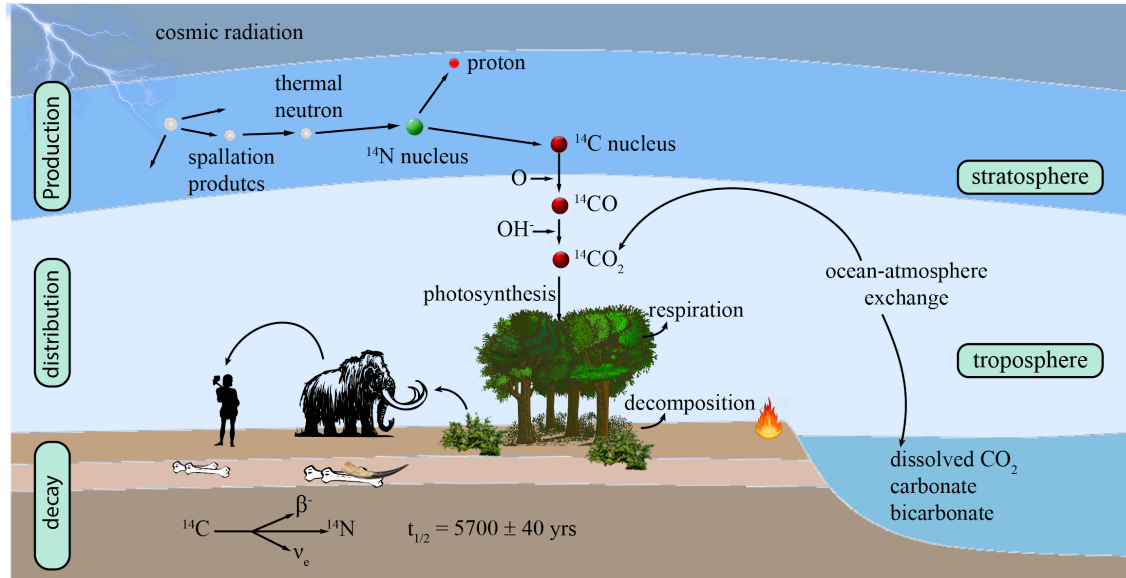


Figure 2.1: **Global Carbon Cycle:** Radiocarbon is produced in the stratosphere as a spallation product when cosmic rays interact with the Earth's atmosphere. During the time between production and decay, it is oxidized to $^{14}\text{CO}_2$, mixed through the atmosphere, and enters the Earth's C cycle

the diet, it reflects their ^{14}C concentration. The oceans act as a reservoir for radiocarbon, reducing the ^{14}C content in the atmosphere. The diffusion of a material within a medium causes the oceans top layer have a lower ^{14}C concentration than the atmosphere (reservoir effect). A box diffusion model has been developed [24] which distinguishes the oceans into two layers: the mixed layer and the deep sea. In this model, the ^{14}C content varies with the depth of the oceans which may further affect radiocarbon concentration in different marine species.

2.2 Radiocarbon decay

Plants and animals assimilate and accumulate the different carbon isotopes present in the atmosphere. Upon the death of an organism, the radiocarbon is no longer replenished from its food, and the total number of ^{14}C atoms in its tissues decreases due to radioactive decay. The number of atoms that disintegrate per unit of time (dN/dt) is proportional to the number of atoms N present at a time t . Given λ as radioactive decay constant:

$$\frac{dN}{dt} = -\lambda N N(t) = N_0 e^{-\lambda t} \quad (2.1)$$

where N_0 is the number of atoms present at initial time $t = 0$. Eq. 2.1 gives the number of radioactive nuclei present at time t (see Fig. 2.2).

The *half-life* ($\tau_{1/2}$) is another representation of the decay constant. The half-life of a radionuclide is the time required for its activity to decrease by one-half. Thus, after one half-life, 50% of the initial activity remains.

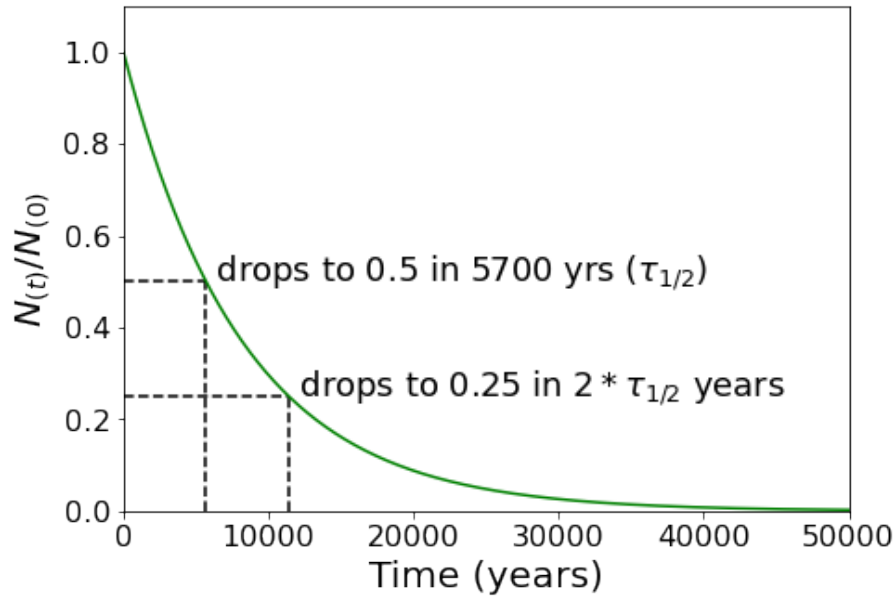


Figure 2.2: **Radiocarbon decay:** Radioactive decay of ^{14}C showing how the proportion of the initial pool (N_t/N_0) decreases over thousands of years, with its half- and quarter-lives. The limit for ^{14}C dating is roughly 10 half-lives

The half-life for a given nuclide can be derived from Eq. 2.1

$$\ln\left(\frac{N}{N_0}\right) = -\lambda t \quad (2.2)$$

If $\frac{N_t}{N_0} = \frac{1}{2}$, the equation yields the half-life $\tau_{1/2}$:

$$\tau_{1/2} = \frac{\ln 2}{\lambda} = \frac{0.69312}{\lambda} \quad (2.3)$$

Libby, Anderson and Arnold were the first to measure the rate of this decay [25]. This value was replaced by the known "*Libby's half-life*" equal to 5568 ± 30 years, resulting from weighted average of three reported measurements that Libby, his collaborators and two other groups had obtained [26]. Newer values of the ^{14}C half-life have been proposed as results of collection of more data and different methods. This value of λ , $1.21 \cdot 10^{-4} \text{ year}^{-1}$, equivalent to a $\tau_{1/2} = 5700 \pm 30$ years, is assumed to be more correct [27]. The calculation of the elapsed time t depends on the assumption that the initial value N_0 (Eq. 2.2) is known. A relative measurement must be performed by comparison of quantified amounts in samples with an internationally accepted standard reference material. Two 'primary' standards are used: the

out of stock standard SRM-4990B, called OX-I, and the standard SRM-4990C, called OX-II or NOX (for New OXalic acid), both distributed by NIST (National Institute of Standards and Technology).

2.3 Global Carbon Cycle

Despite the simplicity of the theoretical method, the experimental measurement of ^{14}C is rather complicated due to both the incomplete verification of the stationarity hypothesis and problems related to the complexity of biological and environmental cycles. The second aspect includes also anthropogenic influences on the radiocarbon source, which make it difficult to assess N_0 . Indeed, the key assumptions on which Libby's theory is based are: (I) the radiocarbon concentration in the atmosphere is spatially uniform, (II) the same concentration is present in terrestrial waters (where CO_2 enters the solution), (III) the atmospheric concentration of $^{14}\text{CO}_2$ has remained constant over time. Due to the effect of the Earth's magnetic field, the quantity of ^{14}C produced by cosmic rays varies with latitude (with a factor of ~ 5 between the poles and the equator). However, these fluctuations are compensated by the atmospheric flows that mix the air around the Earth in a short time (of the order of a few years) compared to the radiocarbon decay time. It can therefore be affirmed that the hypothesis of the stationarity of radiocarbon concentration in a finding, with respect to the place of origin, is correct. In nature, the relative abundances of the three carbon isotopes can differ due to both biological phenomena of carbon assimilation by plants and chemical-physical processes, such as the dissolution of atmospheric carbon dioxide in the waters. This effect is known as isotopic fractionation. The result, on the isotope ratio, is normally expressed as $\delta^{13}\text{C}$ and is defined as relative difference (in ‰ units) between the $^{13}\text{C}/^{12}\text{C}$ of the sample and that of a standard reference material.

$$\delta^{13}\text{C} = \frac{\left(\frac{^{13}\text{C}}{^{12}\text{C}}\right)_{\text{samp}} - \left(\frac{^{13}\text{C}}{^{12}\text{C}}\right)_{\text{stand}}}{\left(\frac{^{13}\text{C}}{^{12}\text{C}}\right)_{\text{stand}}} \times 1000\text{‰} \quad (2.4)$$

The differences in isotopic abundance originates from diffusion phenomena, therefore they are linked to thermodynamic factors in inter- and intra-molecular exchanges and chemical kinetics. Isotope fractionation is a process that occurs both during chemical reactions and during physical processes. It can be a result of slightly different equilibrium constants for different isotopes in a chemical reaction, but evaporation, condensation and thermal diffusion can also cause fractionation. Isotope fractionation occurs when carbon is transferred from one part to another of the ecosystem, e.g. during the photosynthesis process, plants absorbs more $^{12}\text{CO}_2$ than $^{13}\text{CO}_2$ and more $^{13}\text{CO}_2$ than $^{14}\text{CO}_2$. This effect must be taken into account to correct the activity of the sample. It has been shown that the fractionation of the ^{14}C isotope is double than of ^{13}C . Either tabulated values can be used for the correction, or the fractionation

of the ^{13}C isotope can be measured to obtain a precise value that takes into account the fluctuations due to local factors.

The global carbon cycle in the Earth's system can be interpreted as a series of carbon reservoirs which are linked by carbon exchange fluxes. In the global carbon cycle, two domains can be distinguished [28]:

- **fast domain** with high trade fluxes and relatively 'rapid' reservoir turnovers, consisting of carbon in the atmosphere, the oceans, surface ocean sediments and on land vegetation, soils and freshwaters. Reservoir turnover times, identified as reservoir mass of carbon divided by the exchange flux, range from a few years for the atmosphere to decades-millennia for the major carbon reservoirs of the land vegetation and soil and the various domains in the oceans.
- **slow domain** consisting of the huge carbon amounts store in rocks and sediments that exchange carbon with the fast domain through volcanic activity of CO_2 , chemical weathering, erosion and deposition on the sea floor.

During the Holocene (starting 11,700 years ago), before the Industrial Era, the fast domain was close to a stationary state, as evidenced by the relatively small variations in atmospheric CO_2 reported in ice cores [29, 30]. By contrast, since the beginning of the Industrial Era, fossil fuel extraction from geological reservoirs, and their combustion, has resulted in the transfer of significant amount of fossil carbon from the slow domain into the fast domain, thus causing an unprecedented, major human-induced perturbation in the carbon cycle [31]. Indeed, during the last 150 years, the atmosphere has been perturbed due to introduction of additional CO_2 from anthropogenic activities, especially the combustion of fossil fuels and land-use change. This added rate is small compared to the large natural fluxes, but it represents an additional one-way flux into the atmosphere that is not in balance. The ^{14}C isotopic disequilibrium between the sources and the atmosphere is related to four factors: the production of ^{14}C that occurs naturally in the upper atmosphere; the increase of fossil fuel emissions; the anthropogenic production of ^{14}C from nuclear weapons testing or nuclear industry; and the reservoir age, which determines the ^{14}C content in each C reservoir or source. In terms of $^{14}\text{CO}_2$ budget, it is possible to distinguish the atmospheric ^{14}C history in four periods:

- pre-industrial period < 1850
- 1850 < Suess effect period < 1945
- 1945 < bomb peak period < 1985
- post-bomb > 1985

pre-industrial period

The pre-industrial era (conventionally identified as pre-1850) represents an extended period (~ 10 kyr) where the concentration of atmospheric CO₂ was relatively stable compared with today. During that time interval only cosmogenic production, radioactive decay, and land and oceans exchanges influenced the atmospheric ¹⁴CO₂ budget. Cosmogenic production was the only positive flux, increasing ¹⁴C in the atmosphere. Both the terrestrial biosphere and oceans had negative fluxes, since C resides in each of these reservoirs for some time and becomes depleted in ¹⁴C by radioactive decay before returning to the atmosphere.

Suess effect

The first observation of anthropogenic influence on atmospheric ¹⁴CO₂ was made by Suess [32] in 1955. He observed a 25‰ decreasing in atmospheric Δ¹⁴CO₂, which is the measure used to track bomb ¹⁴C [33], between 1890 and 1950 by tree-ring measurements records from North America. The observed effect consists of a change in the ratio of the atmospheric concentrations of isotopes of carbon (¹³C and ¹⁴C) due to the blending of massive quantities of ¹²CO₂ derived from fossil fuels (which are radiocarbon-free).

Bomb peak period

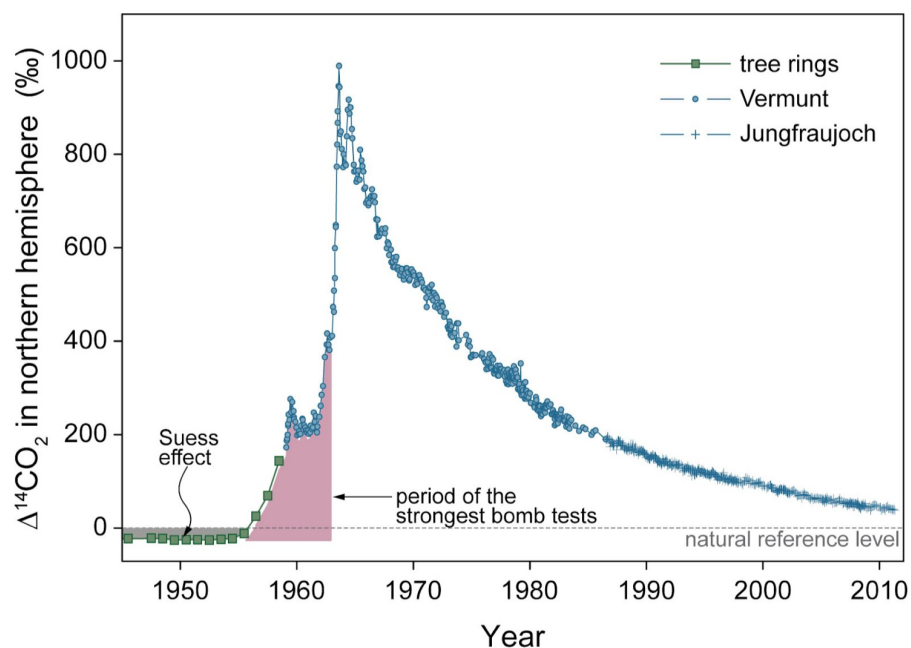


Figure 2.3: **Bomb peak:** the curve represents the atmospheric content of ¹⁴C in the Northern Hemisphere, where most of the nuclear weapons testing took place.

During the 1960s, a networks of atmospheric sampling stations were installed across different sites [34]. These networks were used to observe the radioactive fallout produced by extensive tests of thermonuclear bombs (hydrogen fusion) beginning in the 1950s. The nuclear experiments, conducted in the Northern Hemisphere, doubled the ^{14}C content in the troposphere. Masarik and Beer [35] simulated that it would take 250 years to produce this amount of ^{14}C cosmogenically. The maximum peak was observed in the 1963, immediately before the Limited Test Ban Treaty was signed by the United States, Great Britain, and the Soviet Union, which banned nuclear weapons testing in the atmosphere, in outer space, and under water. From this moment, the $^{14}\text{CO}_2$ started to decrease showing a trend similar to an exponential curve initially falling rapidly (by more than 40‰ per year), as is shown in Fig. 2.3. As well as fossil fuel combustion in the Suess effect, the C cycle distributed the bomb ^{14}C contribution throughout the biosphere. Indeed, in addition to radiocarbon production due to bomb testing, there is an added amount of production deriving from the nuclear industry and research applications [36].

Post-bomb period

The post-bomb period is considered to start in the 1980s, when the influences on atmospheric $^{14}\text{CO}_2$ had changed after the bomb peak. In this phase, we have been observing the absorption of bomb ^{14}C into longer term reservoirs and the increasing fossil fuel emissions. Between 1985 and 2005, CO_2 emissions from combustion of fossil fuels increased by $\sim 50\%$ [37]. Dilution of $^{14}\text{CO}_2$ by fossil-derived CO_2 is now the strongest contribution to one of the main influences on seasonal cycles of $^{14}\text{CO}_2$ in the Northern Hemisphere [33, 38–40].

2.4 Radiocarbon detection

Libby and his team developed the radiometric method in 1949 [25]. The proposed approach is based on the measurement of the radioactive decay rate of the nuclide of interest and corresponding measurement of the emitted beta particle by absorption on a sensitive element (detector). The beta particles are characterized by a quantity of kinetic energy which is typical for each radionuclide (in quantitative terms). Emitted beta particles have a continuous energy spectrum which can range from a few keV to a few tens of MeV. Until now, only three methods provide the measurement of the radiocarbon content in a sample:

- Gas proportional counting (GPC)
- Liquid scintillation counting (LSC)
- Accelerator mass spectrometry (AMS)

GPC is a conventional radiometric technique developed by Dutch physicist Hessel de Vries [41] that replaced Libby's solid carbon method. The method relies on counting the beta particles, produced by radiocarbon decay, emitted from a sample. Furthermore, it requires that the sample carbon is converted into gaseous carbon dioxide before measurement in the gas proportional meter.

Conventional GPC systems consist of a sample detector surrounded by an active screen (guard counter system), a proportional ring gas meter, or a series of long cylindrical or Geiger proportional detectors. A layer of old mercury or lead is inserted between the sample detector and the guard counter system. A layer of boron paraffin, 5-10 cm thick, usually surrounds the guard counter system to absorb the neutrons formed by cosmic rays in the passive screen that encloses it, which consists of a layer of lead or iron [42].

LSC is another radiocarbon dating technique, developed in the 1960s [43, 44]. The method is based on the conversion of the sample into a liquid form suitable for analysis in LSC and a scintillator is added. Indeed, the energy conversion and transmission take place due to the dispersion of the radioactive sample in a "scintillation cocktail" which acts as a detector. The emitted radiation transfers its energy, producing molecular dumping and un-dumping events followed by the release of photons. The scintillation cocktail produces a flash of light when it interacts with a beta particle. A tube containing the sample is passed between two photo-multipliers and the count occurs only when both devices register the flash of light. Nuclear events generate ~ 10 photons per KeV and the energy is dissipated in 5 nanoseconds time. Depending on the form of scintillator, wavelengths of the emitted electromagnetic radiation range from 375 to 430 nm. The approach is consolidated and characterized by an uncertainty of $\sim 0.2 - 4\%$, however it is still rather expensive in terms of both time and costs. The main drawback of the technique is linked to the need to treat a large sample to obtain the required amount of benzene compatible with the LSC analysis, considering the overall yield of the process. The method is optimal for 5-6 g of carbon, resulting in a final yield of ~ 5 ml of benzene. Table 2.1 reports the carbon content of some typical materials of interest and the required mass for the radiometric analysis.

Table 2.1: Carbon content and mass required for the radiometric analysis of ^{14}C .

Material	Typical Carbon Content (%)	Mass (g)
Wood	50	4-20
Charcoal	70	3.5-15
Dry peat	50	4-25
Wet peat	5	40-200
Humus	0-5	120-1000
Bone	0-30	50-500
Carbonate	12	15-60

A further technological evolution in the isotopic ratio analysis consists in the development of the AMS technique, combining mass spectrometry with an accelerator [45, 46]. This technique has found a successful application in radiocarbon detection. Since the β radiation from the ^{14}C atom decay is a low-energy emission (156 keV), a sophisticated detection solves the measurement problems related to this low energy value. Through ionization and acceleration in an electric field, the identification of atoms is achieved. However, traditional spectrometers do not have the required sensitivity to differentiate isobaric nuclei, but mass spectrometers have been modified to isolate a rare isotope from a large surrounding mass. This way made possible radiocarbon detection in a sample, avoiding the most common isobars that bury the signal. Isobaric interferences, ions with the same mass as ^{14}C , are the most critical contaminants in mass spectrometry. Very abundant ^{14}N and molecular ions, such as ^{13}CH and $^{12}\text{CH}_2$, are the known contaminants, because they cannot be suppressed by standard mass spectrometry. Indeed, depending on the detection resolution, processes that produce background ions can occur. These processes involve impacts of residual gas ions in the accelerator beam line, which modify the state of charge or the energy of the ions and for this reason needs to be considered. The AMS analysis of carbonaceous samples requires that they are previously converted into graphite. The conversion is carried out through a first oxidative stage to CO_2 by combustion and subsequent catalytic reduction to elementary carbon. The graphitized sample is introduced into AMS where it is subjected to ionization by an ion source. Electrostatic acceleration, with a charge-exchange scheme called tandem accelerator, is the core unit of the accelerator used in ^{14}C AMS to increase the final ion energy. Here, the ions are separate. At this stage, the ions pass through a "stripper" process where stochastically exchange electrons with the atoms from the foil or the gas. The stripper is placed on a positive electrical potential called the terminal voltage in the tandem accelerator, which attracts the negative ions produced in the ion source of the ion. After the stripper has changed the charge of the ions, from negative to positive, owing to the repulsion of the positively charged ions from the positive terminal voltage, they are further accelerated away from the terminal. Application of a magnetic field deflects the path of moving charges. Carbon isotopes that have the same energy but different mass are deflected at different trajectories. Finally, detectors placed at different angles of deviation allow the counting of the particles. At the end of the AMS cycle, collected data include the number of ^{14}C , ^{13}C and ^{12}C atoms in the sample. On this basis, it is then possible to calculate the concentration ratio of the isotopes.

2.4.1 Limits encountered in AMS and LSC radiocarbon detection

The critical aspect encountered in the measurement of radiocarbon is linked to the extremely low natural abundance of this isotope present in traces (10^{-12}). For its detection, a high sensitivity and precautions are required for the elimination of possible interferences (e.g. isobars in AMS and beta emitters in LSC). The sample converting systems are difficult to manage and, in some cases, reveal safety problems related to the use of carcinogenic substances. In

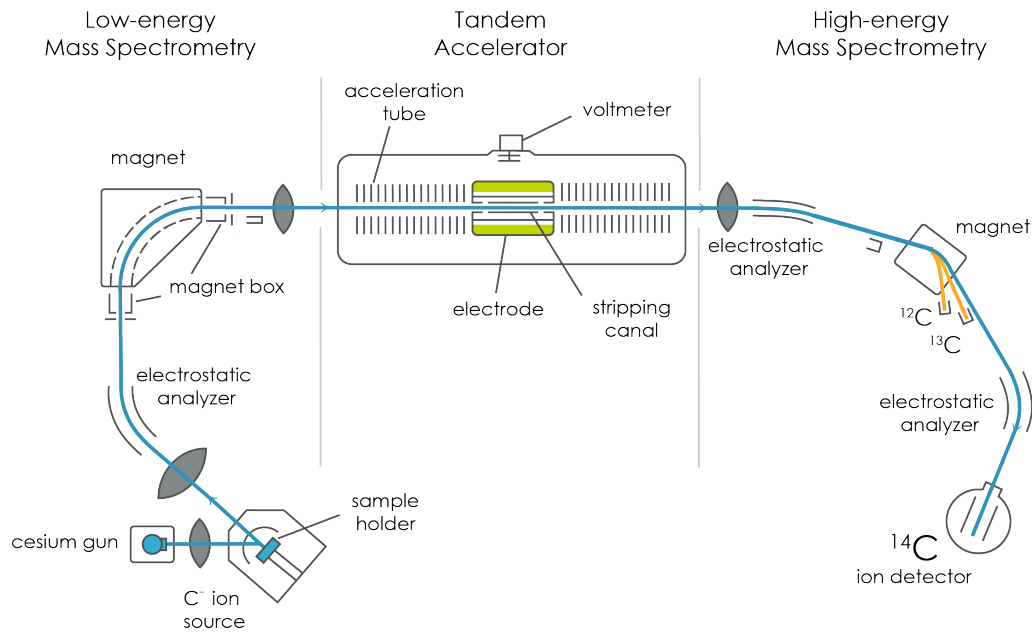


Figure 2.4: **Generalized schematic of the main parts of an AMS facility.** The blue line indicates the central ion trajectory. Since magnetic sector fields disperse the trajectories of ion beams with the wrong momentum, these deviate from the central trajectory and are filtered out. The electrostatic analyser, as indicated in the high-energy beam line, filters analogously the ion beams with the wrong energy (orange line). The stripper (yellow) and the detector are both gas filled

LSC analysis, the ^{14}C very low environmental concentrations need to treat large amounts of sample, with consequent waste of time and costs, and to extend the analysis times to reach statistically significant counts and adequate precision. On the other hand, the AMS analysis requires minimum amount of sample and this leads to a very high risk of contamination by modern ^{14}C , especially in the case of low activity samples, therefore the sample pretreatment and handling steps must be rigorous. For high-precision dating, where unwanted bias effects of the order of 10 years are important for recent sample, modern and fossil contaminants need to be kept below about 0.1%, or about $1\ \mu\text{g C}$, in a typical AMS sample. For all other cases, levels of contamination up to 1% are acceptable [22]. Parallel to this aspect, there is a problem related to the data reporting conventions and the standardization of the units commonly used in the ^{14}C analysis. Stuiver and Polach [26] summarized the conventions and these are still used today, especially in the archaeometric dating field.

The complexity of these aspects means that radiocarbon analysis is still a niche limited only to specialized laboratories. There are currently 150 radiocarbon laboratories and about 100 AMS laboratories internationally [46]. Beta Analytic in Miami (USA) is the only operator having an industrial character, with a productivity of tens of thousands samples each year, whereas all the others are research laboratories with very small productivity.

2.4.2 Radiocarbon detection using mid-IR spectroscopy

The state of the art standard methods for ^{14}C measurement are the above described low background LSC, for very large samples, and AMS, which can achieved extremely high sensitivity. However, these methods have neither on-line nor on-site capabilities, and usually require complex sample preparation or need large sample mass. Therefore, a technique with in-situ measurement capabilities is needed. Detection of ^{14}C with optical techniques has recently gained interest as technology for mid-IR instrumentation has improved. Detection of $^{14}\text{CO}_2$ using diode laser spectroscopy was studied in the 1980s [47, 48], but with the technology of that time the foreseen detection sensitivity was relatively low. This was because ^{14}C has a very low natural abundance, near 1 ppt, requiring both very narrow band lasers for specificity, as well as efficient detection mechanisms for enhanced sensitivity. To achieve the required sensitivity, optical cavities can be used to enhance the interaction length of the laser with the ultra-low-concentration radiocarbon molecules. From the user point of view, differences in sample size and sample preparation criteria may be very significant. Laser techniques require burning samples to oxidize their carbon content to carbon dioxide, while AMS mostly requires a further reduction step to convert it to elemental carbon (graphitization). Spectral data for $^{14}\text{CO}_2$ are available in a few publications [2, 49]. The strongest absorption band for the detection of $^{14}\text{CO}_2$ corresponds to the fundamental asymmetric stretching ν_3 ro-vibration band. In particular, the P(20) line at $4.527\ \mu\text{m}$ ($2209.1\ \text{cm}^{-1}$) resulted to be the most suitable for detection of $^{14}\text{CO}_2$ by laser spectroscopy. Laser-based radiocarbon detection does have the potential to achieve notable sensitivity for small gaseous samples in a compact instrument. This is because lasers interrogate molecules and can induce multiple photon absorption processes from each $^{14}\text{CO}_2$ molecule. Differently, LSC only counts radioactive decays of a very small fraction of ^{14}C atoms, while AMS counts each accelerated ^{14}C ion only once. Counting precision is thus limited by Poisson statistics to $N^{-1/2}$, where N is the number of counts, whereas with the laser interaction the precision improves as $t^{-1/2}$ where t is the averaging time. Well designed counting experiments can achieve negligibly small background count rates whereas photon interactions with most of the species present in the sample yield a significant background signal that must be understood, monitored and subtracted from the total laser induced response in order to quantify the amount of radiocarbon. Two types of laser technologies have been used, so far: CRDS and intra-cavity optogalvanic spectroscopy (ICOGS). In the second case the results were contested because they were not repeatable. Moreover real-world samples were never measured, yet. The first ICOGS work, with a fixed frequency stabilized $^{14}\text{CO}_2$ laser, was published in 2008 [50].

This technique is based on the existence of large isotopic shifts in molecular spectra, the use of narrow band (<1 MHz) fixed frequency isotopic lasers and detection via optogalvanic effect (OGE). The basic principle includes the use of a common CO_2 laser filled with a gas mixture containing pure $^{14}\text{CO}_2$ as gain medium, which can provide the specificity to excite a $^{14}\text{CO}_2$ molecule transition at $11.7\ \mu\text{m}$. OGE laser interaction (absorption or stimulated

emission) leads to an impedance change of an electric discharge through the sample gas that can be positive or negative. Cavity ring-down spectroscopy (CRDS) was proposed as a better and more reliable solution and, to reach the needed sensitivity, CW-CRDS was used [51]. It employs a continuously tunable narrow band laser and the signal are retrieved from fitted line shapes and known absorption cross-sections in order to determine absorbing species concentration. The absorption coefficient, α , is expressed in terms of cavity exponential decay time τ_ν , via $\alpha(\nu) = 1/c(1/\tau(\nu) - 1/\tau_0)$ where τ_0 is the ring-down time in vacuum and ν the wavenumber. In principle, CRDS provides a passive ring-down cavity with an effective path length of the order of 10 km. Since a highly stabilized laser is employed, separation of background from signal is achieved by fitting the full line shape of a spectral feature centered at the chosen frequency where the signal to noise ratio (SNR) is higher. In the last years, a few significant and successful works have demonstrated ^{14}C optical detection in the mid IR. All these spectrometers are based on the principles of linear-absorption CRDS that can only detect enriched levels of radioactivity, for application like studying decommissioned nuclear power plants, or for biological and environmental tracing application. In particular, Genoud et. al. [52], by using, in their system, a commercially available quantum cascade laser with a linewidth of a few tens of MHz, achieved a sensitivity limit of ~ 800 pMC (percent Modern Carbon), which is a suitable value for monitoring nuclear power plants and for other industrial applications. McCartt et.al [53] achieved high sensitivity (11,2 pMC) for tracing ^{14}C -enriched biological samples with 3 mg sample mass. This more complex spectrometer used a cavity cooled at $T = 250$ K which reduces both total interference and temperature sensitivity of nearby ro-vibrational transitions. Notwithstanding, operating in presence of significant spectroscopic interferences limited their spectrometer sensitivity, thus restricting applications to the study of ^{14}C -enriched samples. Fleisher et.al. [54] made other improvements to better determine backgrounds with a cavity requiring 18 mg of C at $T = 220$ K and $P = 0.93$ kPa. A high-precision frequency axis is defined by the transmission spectrum of a temperature-stabilized high-finesse ($F = 52000$) optical resonator, containing the gas-phase CO_2 sample under investigation. With this experiment, they also achieve 11 pMC of sensitivity. The demonstration of mid-IR spectroscopic detection of $^{14}\text{C}^{16}\text{O}_2$ by SCAR addressed all these challenges by implementing a novel non-linear cavity-enhanced approach to achieve a sensitivity of 0.4 pMC [55, 56]. In Chap. 3 we will discuss further improvements to the sample cell as well as to the sample preparation protocol, making SCAR precision comparable with AMS facilities.

2.4.3 Fields of applications

Starting from the development of the radiocarbon method, there were two main fields of application involved: both archaeology and Earth sciences contributed to the development of the potential of the method. The first findings of archaeological interest dated by the ^{14}C method and used for reconstruction of the calibration curve were wood samples from the

Egyptian tombs of Zoser at Sakkara and Sneferu of Meydum [25]. Although radiocarbon dating required a large amount of materials in the early days of the method, so that few objects could be actually used for analysis, this technique has revolutionized archaeology over the years, and this is currently considered to be the main field of application. The Conventional Radiocarbon Age (CRA), expressed in yr BP (years Before Present), underwent calibration, in order to obtain the “real” calendar date, by comparing the conventional dating with calibration curves obtained by dating artefacts of known periods. Through the dendrochronological study of tree growth rings, calibration curves have been realized for the last 11 kyr (thousand years). Instead, based on the annual growth of corals, it was possible to go as far as about 24 kyr ago. The calibrated date is considered the best estimate of the “true” date and is the one that must be taken into consideration to draw historical conclusions. Like for archaeology, paleoclimatic science paces the development of the ^{14}C dating method. Atmospheric $\Delta^{14}\text{C}$ reconstruction and consequent calibration of the ^{14}C time scale till 50 kya (thousand years ago) has been a goal of the scientific community. This need arose after the discovery that production of ^{14}C atoms in the atmosphere was not constant and because the radiocarbon method was required in quaternary periods studies. Indeed, climate change is followed by changes on land, in the oceans, and in the atmosphere with an alteration of the global C cycle. With the measurements of trace gas concentrations in ancient glacial ice layers, it was revealed that atmospheric CO_2 concentration was one-third lower (195 ppm) during the last glacial maximum (LGM) 20 kya ago than that during the present interglacial (IG) period (12 kya to 200 years ago), (280 ppm) [33].

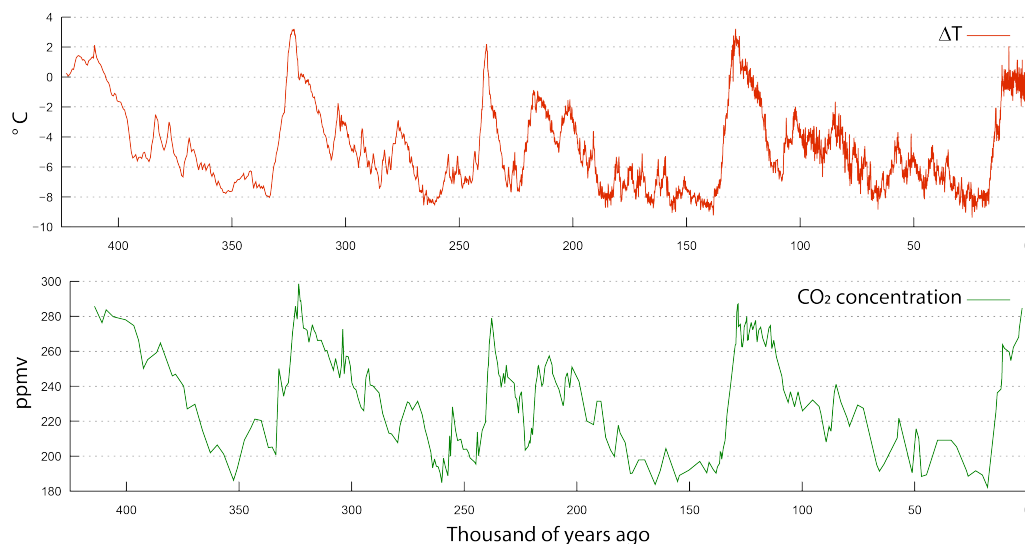


Figure 2.5: Graph of planetary temperature variation (red curve) and CO_2 content (green curve), measured from the Vostok ice core, Antarctica, as reported by Petit et al., 1999 [57].

Technological development, particularly with the advent of AMS, opened up new possibilities

for dating unique objects and archaeology studies and climatology applications could further improve, leading to new problems to solve. Biomedical and environmental studies more recently enriched the spectrum of applications. Following the observation of anthropogenic effects described in this chapter, in particular those related to the emissions of fossil fuels into the atmosphere (Suess effect) as well as the nuclear tests, new scenarios for radiocarbon analysis have been opened. Radiocarbon allows qualitative and quantitative assessments of the origin of the emission source through direct analyses on air or atmospheric particulate matter. This principle was exploited to evaluate the effect of different anthropogenic and biogenic sources on air quality; indeed, radiocarbon is a solid tracer of biogenic sources, since it is not altered by the chemical changes that occur in the atmosphere. The possibility of characterizing the sources of fuels, through the analysis of the gaseous components of the industrial facilities or through a direct analysis of the fuel represents a field of application of recent interest. This application could play a key role in promoting globally adopted political-legislative initiatives. On the one hand, the limited availability of fossil fuels and on the other the goal of reducing greenhouse gas emissions, including CO₂, on a global scale, forces the industrial sector to certify biogenic sources. The ability to distinguish between the biogenic and the fossil fraction in a fuel blend assumes a clearly strategic value for the traceability of both the supply chain and the estimation of the emission rights and disbursement of incentives for those using renewable sources. In this scenario, the use of radiocarbon as unequivocal marker of the presence of biogenic compounds represents an effective method for distinguishing CO₂ of fossil origin. Likewise, the fields of application of the radiocarbon method in the environmental sector comprises the determination of renewable fraction in urban waste, residue-derived fuel and secondary solid fuel, which is related to the possibility of trading emission certificates within the Emissions Trading System regulations and to the recognition of economic incentives for the energy produced by combustion of the renewable fraction in waste [58].

The field of biobased products is growing strongly both in the chemical sector (such as biosolvents, biocatalysts, biofibers) and in terms of commonly used materials (such as biocosmetics and biopolymers). Several studies explored the potential of the radiocarbon method in relation to a wide range of consumer and industrial products such as solvents and lubricants, materials for construction, fertilizers, cosmetics, synthetic intermediates and polymers [59]. Raw materials of biological origin are recyclable in short periods as compared to fossil-based. Therefore, biobased products can make a significant contribution to reduce CO₂ emissions. The determination of radiocarbon content acquires its value in order to certify “green” products, which is currently considered an areas of the utmost interest. Nowadays, the biobased sector is fast growing and several studies explored the potential of the method of radiocarbon analysis for a wide variety of consumer and industrial products [60–62]. The pharmacokinetic (PK) properties of new drugs are thoroughly tested in current drugs development procedures. The pharmaceutical industry has become aware of the need to adequately test PK properties in order to produce superior drugs. There are frequent cases of drugs which, although ini-

tially approved, have been withdrawn from the market due to unexpected effects in human dispersing. Systematic research focusing on predicting drug PK is needed in early drug development. It has been demonstrated that radioisotopes play a role in advancing our knowledge in biomedical sciences [63, 64]. Carbon (thus ^{14}C) has such a stability that it is a built-in molecular design of standard organic chemicals. Radiocarbon is sufficiently active as a β -emitter to be detected by standard techniques, therefore it is used as a drug marker to study absorption, distribution, metabolism, and excretion (ADME) in pharmacokinetics [65, 66]. Radiocarbon, released into the atmosphere due to the effects of nuclear power plant management, is far from negligible and it is currently the main anthropogenic emissive source. It results from the neutron-induced reactions on isotopes of carbon, nitrogen, and oxygen present in the fuel, cladding, coolant, moderator, and structural materials of reactors. For the ^{14}C produced in the coolant system of nuclear plant circuits, about 95% is expected to be available for gaseous release, with the remaining 5% becoming mostly part of the low-level waste, mainly stored in the ion exchange resins, used for the removal of radionuclides in different liquid waste treatment systems of nuclear power plants [67]. The degradation of the irradiated polymeric material can cause the re-mobilization of the ^{14}C content and subsequent release into the environment. Radioactive waste must be systematically analysed in the matrices in which it is mainly present, typically graphite, steel and cement deriving from the decommissioning of nuclear reactors. Rapid continuous in-situ analysis would be valuable as it can provide better monitoring capabilities in support of power plant operators, nuclear waste management organizations, and regulators.

3

Saturated-Absorption Cavity Ring-down (SCAR) technique

In 2010, Saturated Absorption Cavity Ring-down was demonstrated and successfully exploited for sub-Doppler measurements of the $^{16}\text{O}^{12}\text{C}^{17}\text{O}$ isotopologue of carbon dioxide at low pressure. For this latter isotopologue, this technique was able to resolve the hyperfine structure of its (00⁰1 - 00⁰0) R(0) ro-vibrational transition [68]. The earlier experimental SCAR setup was based on a low-power (< 100 μW) DFG-coherent source with narrow linewidth and absolute frequency traceability, provided by the phase locking of pump and signal sources to a near-IR frequency comb. This apparatus allowed for the first ever optical detection of the ultra-rare $^{14}\text{C}^{16}\text{O}_2$ isotopologue of carbon dioxide at natural abundance (~ 1.2 ppt) [55]. In this chapter we will discuss about some upgrades of the SCAR technique, which allowed us to realize the first measurement of radiocarbon dioxide in real-world samples with improved uncertainties, below 1%.

3.1 Experimental setup

Due to its low natural abundance, radiocarbon dioxide requires an extremely high-sensitivity for detection. SCAR, benefitting from both CRD and saturation spectroscopy, can provide the sensitivity required. Indeed, it was demonstrated that the SCAR technique improves by more than one order of magnitude the limits of CRDS, thanks to a sample absorption measurement which is independent from the other cavity losses during the same cavity decay event (see Sec. 1.3.5). Some upgrades realized in the last years allowed us to further improve the sensitivity of this technique. The improved SCAR setup is described below. In SCAR spectroscopy, laser

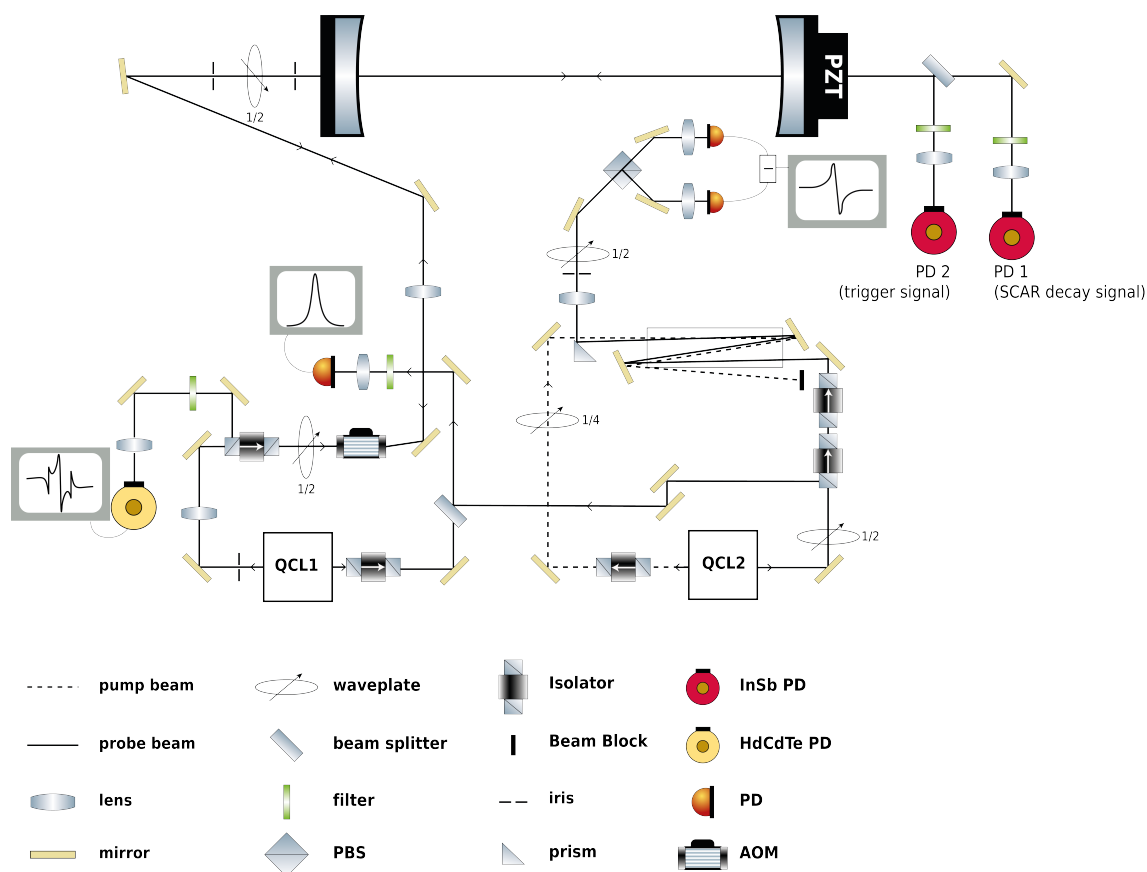


Figure 3.1: A sketch of the optical SCAR setup

radiation must be coupled to the cavity in the most efficient way. Specifically, the intra-cavity laser power at the beginning of the decay must be much higher than the saturation power of the targeted molecular transition. Regardless of the power enhancement factor of the cavity provided by its high-finesse, the requirement for the incident laser power at the cavity input is more relaxed for TEM_{00} and narrow linewidth laser sources. Moreover, this technique requires

laser sources tunable in a wide spectral range, as well as absolute frequency calibration of their frequency. Laser frequency stabilization could be a useful tool to improve sensitive detection of molecules with SCAR, by implementing long-time-average gas absorption measurements. Frequency stabilization of mid-IR QCLs to high-finesse optical cavities or to the side of a Doppler-broadened molecular absorption line achieves narrowing of the QCL emission but lacks in providing absolute frequency referencing. On the other hand, frequency lock of a QCL in the center of a sub-Doppler molecular line provides an absolute frequency reference. Fig 3.1 shows the SCAR experimental setup. Two QCLs (Hamamatsu Photonics) are used in the optical setup, both emitting ~ 100 mW CW radiation tunable in the range $2208\text{-}2212\text{ cm}^{-1}$ ($\sim 4.5\text{ }\mu\text{m}$), to perform frequency-synthesized heterodyne spectroscopy. QCL2 is frequency-locked to the $(02^0_1\text{-}02^0_0)$ R(16)e transition of N_2O at 2209.0854 cm^{-1} which is used as a frequency reference. The first derivative of the absorption profile of this reference line is detected by polarization spectroscopy, at 0.45 mbar pressure and 40 cm absorption path-length. QCL1 is locked by PDH technique to the resonant cavity and it is used as a probe laser for the SCAR spectroscopy of the $(00^0_1\text{-}00^0_0)$ P(20) transition of $^{14}\text{C}^{16}\text{O}_2$. Both QCLs are frequency stabilized, narrowed and controlled by locking loop chains. The beat note between the first and the second laser is locked to a scanning frequency synthesizer, by sending a feedback signal to the PZT-mounted mirror controlling the cavity length, thus closing the stabilization loop of the QCL1 frequency relatively to QCL2.

3.2 Fabry-Pérot ring-down cavity

In a classical Fabry-Pérot (F-P) configuration, the width of a cavity mode can be expressed as the ratio between the free spectral range and the finesse. In order to have an effective radiation-gas interaction paths as long as possible, the cavity should have very narrow modes, a condition that requires either high-finesse or a small free spectral range. Optical cavities with a small free spectral range have the major drawback of mechanical instability because of their considerable length: this would introduce an external noise at low frequencies in the output signal that depends on the cavity length variations. Furthermore, when dealing with quantum cascade lasers, the optical feedback coming from a F-P resonator can be a serious limit. The SCAR F-P cavity (shown in Fig. 3.2) consists of a quartz tube of 0.7 L of volume, which is surrounded by a copper tube coated by a multilayer aluminized-mylar super-insulation material which strongly suppresses any radiative heat transfer from the room temperature external vacuum chamber. The choice of the cell material fell on quartz since its low adsorption property and low thermal expansion coefficient. It is equipped with two ZnSe plano-concave mirrors coated with high-reflectivity multilayer dielectric materials with transmission $T \sim 120$ ppm and (absorption + scattering) $A \sim 30$ ppm, totalling overall losses $1 - R \sim 150$ ppm. The mirrors radius curvature of 3 m produces a narrow beam waist ($w_0 = 1.27$ mm at the cavity center) for all the TEM_{00} longitudinal modes, thus enhancing

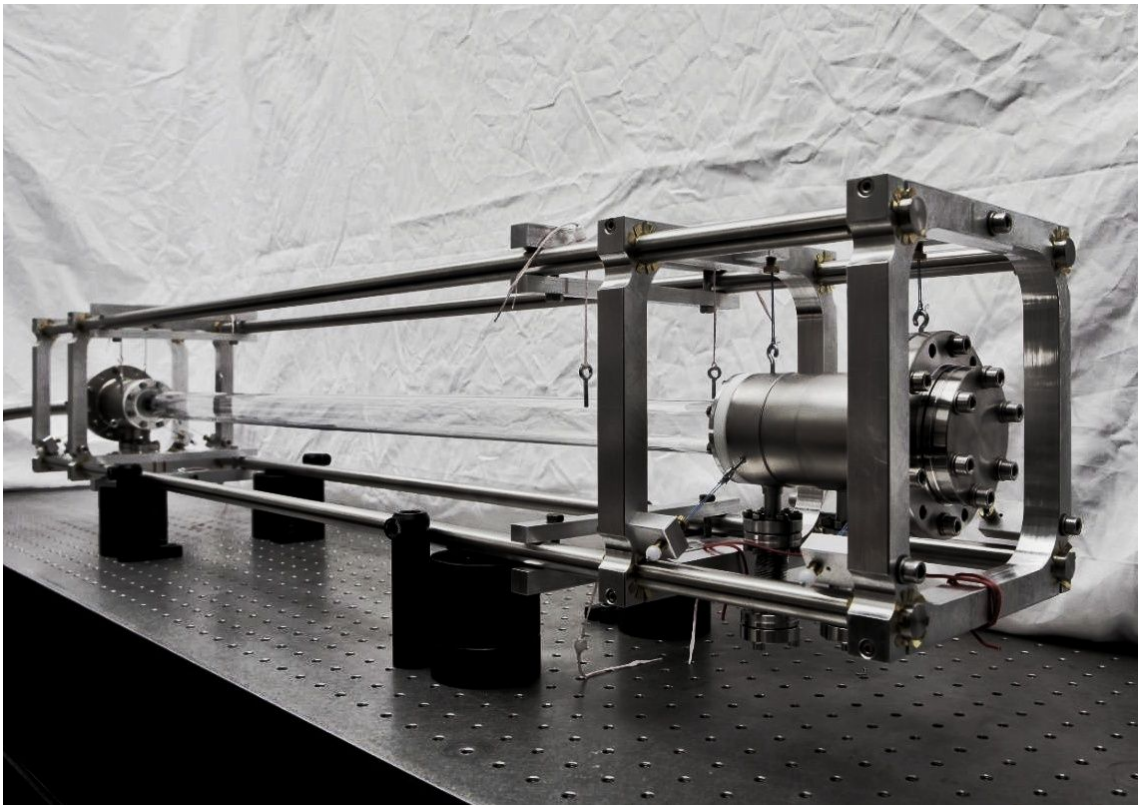


Figure 3.2: The SCAR Fabry-Pérot cavity

the nonlinear saturation effects exploited by the SCAR technique. This resonator has a free-spectral range (FSR) of 149.986 MHz at 4.5 μm . The measured mode FWHM at this frequency is ~ 7 kHz, corresponding to a Q -factor of $\sim 9 \times 10^9$ and a finesse of ~ 20908 . The described features yield a ring-down time of $\sim 22 \mu\text{s}$ and an effective interaction path between IR radiation and gas sample of ~ 6.6 km. The cavity is cooled down to 170 K by means of a cryogen-free Stirling acoustic cryocooler (Qdrive, mod. 2S102K-FAR-DE-TI) and it is housed inside a vacuum chamber providing both thermal and acoustic insulation. This cooling system allows us to reduce the effects of interfering hot-band lines deriving from all other CO_2 isotopologues, in particular the $(05^5_1 - 05^5_0)$ $\text{P}(19)\text{e } ^{13}\text{C}^{16}\text{O}_2$ transition at $2209.1159 \text{ cm}^{-1}$. The long-term temperature stability of the optical cavity, as well as the uncertainty of the temperature measurement, are critical factors due to the temperature dependence of the molecular line intensity S . Therefore it must be constant and it is monitored by 8 Pt100 electrical resistances distributed along the cavity. Three resistive heaters provide to actively stabilize the temperature and to minimize any thermal gradient of the cell. The dependence of the line intensity S on temperature will be discussed in sec 3.4. With respect to the first SCAR set-up, the volume has been reduced by about one order of magnitude. This has as a consequence a lower amount of sample gas needed for the measurement, which now corresponds to 6 mg of carbon content. The external gas filling line was redesigned in order to optimize the vacuum performance of the turbo-molecular pump (HiCube 80 Eco, DN 40 ISO-KF, MVP 015-4), so to obtain a pressure as low as 10^{-3} hPa, measured outside the cavity. Detector PD 2 (in Fig. 3.1), a liquid N_2 cooled InSb photodiode, provided by Hamamatsu Photonics, has the function of detecting the (established) threshold for filling the cavity with IR radiation. When the threshold is reached, the acousto-optic modulator (AOM) rapidly switches the laser beam off and the ring down event begins.

3.3 Single-frequency QCL loop chains

To achieve the high-sensitivity and sub-Doppler resolution spectroscopy provided by the SCAR apparatus, it is fundamental to have an intense and narrow (low-frequency-noise) mid-IR laser source. Since this experiment also aims to high accuracy for detection of trace molecules, an absolute frequency reference is required. As we mentioned in Sec. 1.2.2 QCLs are ideal candidates to provide these features thanks to their intrinsic linewidth, comparable to the natural linewidth of molecular transitions (tens-hundreds of Hz). Moreover, the radiation emitted by a QCL can achieve a power spanning from μW up to W. These characteristics give them appeal to be used for SCAR spectroscopy. Unfortunately, over time scales spanning from 10 ms to 1 s, QCLs linewidth is way wider in free-running operation (about 1 MHz) due to the $1/f$ noise contribution. To overcome this limitation, a frequency stabilization loop chain was implemented. Two QCLs, mentioned in Sec. 3.1, are employed in the optical setup. QCL1 is used as a probe laser for the SCAR spectroscopy of the $\text{P}(20)$ target line, QCL2 is

frequency-locked to the $(02^01 - 02^00)$ R(16)e transition of N_2O at $2209.0854 \text{ cm}^{-1}$. These lasers require thermal stabilization and a beam collimator. With this purpose, *ad hoc* mounts have been created which include a thermoelectric Peltier cell for temperature stabilization and an aspheric collimating lens positioned on a mount that allows 3-axis adjustments of the three axes. Moreover, these lasers are in C-mount configuration that enables the emission from both facets and powered by ultra-low-noise current drivers (ppqSense S.r.l.). A frequency stabilization chain with two locking loops efficiently narrows and controls the QCLs frequency.

3.3.1 Pound-Drever-Hall (PDH) locking

To tightly lock the laser frequency to a resonance of the Fabry-Pérot cavity, the resonance must be detected quickly and with a high SNR. This is perhaps the most critical part of the feedback loop, as it ultimately determines the performance of the system. Since on the characteristic times of the measurement, the linewidth of the emitted radiation is approximately of 500 kHz, which is much higher than the 7 kHz cavity resonance width, QCL1 shown in Fig. 3.1 is locked to the high-finesse cavity with the PDH technique (described in Sec. 1.2.4) in order to maximize the power coupling into the cavity itself. This lock allows to further tighten the emission spectrum of the laser in such a way to couple over 60% of the radiation into the cavity, thus allowing to reach the required level of saturation of the P(20) target transition of $^{14}C^{16}O_2$. Furthermore, since this lock keeps the laser frequency resonant with a cavity mode, it enables the acquisition of CRD decays at high rate ($\sim 3 \text{ kHz}$), with a duty cycle of about 50%. The QCL emitting at $4.5 \mu\text{m}$ is provided by Hamamatsu Photonics. It operates at room temperature and 527 mA current, delivering a measured output power of about 59 mW, and it is modulated at 4MHz to add to the laser carrier frequency the two FM side-bands required by the PDH lock. In this way, the QCL1 linewidth ($\sim 500 \text{ kHz}$ free running) is made narrower than the cavity resonance width ($\sim 7 \text{ kHz}$), achieving a locking bandwidth of about 300 kHz. Its drift/jitter frequency fluctuations follow the cavity resonance and thus the IR photons are efficiently coupled to the cavity itself, only limited by the spatial mode matching ($>60\%$). The QCL1 beam reflected back by the cavity is sent to the PDH detector by the input polarizing cube of the optical isolator. The PDH locking signal is obtained by demodulating (with the right relative phase) the detected photocurrent at the modulation frequency of 4 MHz, by use of proper RF electronics (a mixer and a low-pass filter). This signal is further processed by a proportional, integral, differential (PID) amplifier and sent to the laser current to close the locking loop.

3.3.2 Polarization spectroscopy (PS) locking

High-sensitivity spectroscopy, such as SCAR, requires a radiation source with high frequency stability both at short and long timescales, therefore with a narrow linewidth and linked to an absolute frequency reference. The strategy used consists in referring the emission

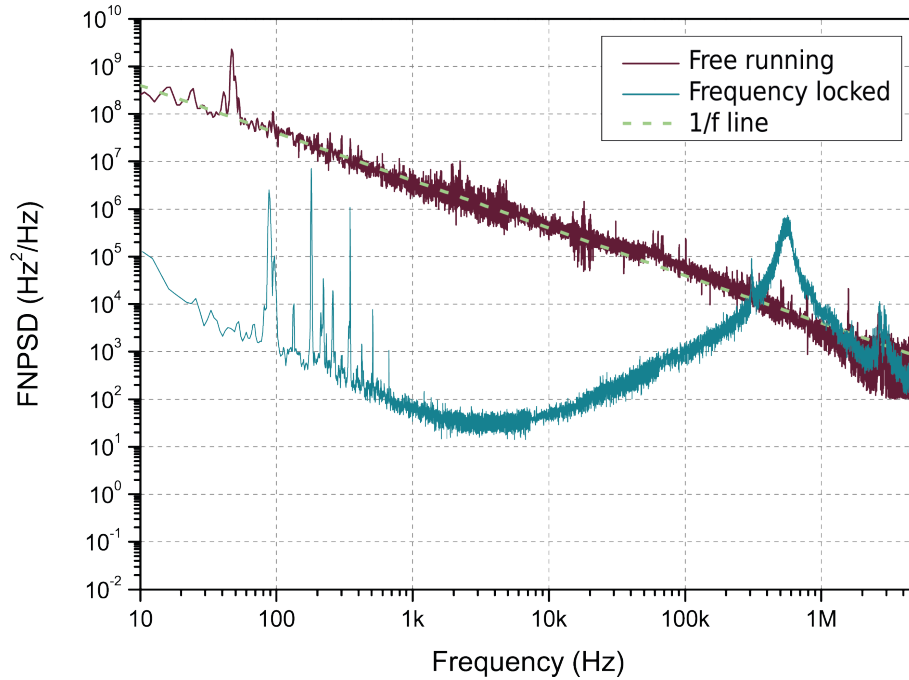


Figure 3.3: Panel a: bordeaux and blue traces represent free-running and locked QCL2 FNPSD.

itself to a molecular absorption line (frequency locking). PS is the most suitable technique, since it directly generates the narrow (sub-Doppler) dispersive signal, without any external modulation, to be in the feedback loop on the QCL2 driving current to stabilize its emission frequency. PS exploits the birefringence that a circularly polarized pump laser beam induces on absorbing molecules, generating a polarization rotation in a linearly polarized probe beam which is proportional to the derivative of the molecular absorption profile. The sub-Doppler absorption feature has a Lorentzian line shape whose derivative has a typical S-shaped dispersive profile. With appropriate settings, the signal is zero on the absorption center and varies linearly around it. By using this PS scheme, a narrow-emission, down to sub-kHz level, was achieved [56] with the aim of obtaining an absolute frequency reference for the Fabry-Pérot ring-down cavity. The linewidth of a CW-QCL can be narrowed below 1 kHz (FWHM) by locking the laser to an N_2O line, as explained before. For the QCL2 frequency stabilization, the PS signal is processed by an electronic controller (PID), and fed back to the field-effect transistor (FET) gate for current control, in order to suppress its frequency fluctuations. The effect of frequency locking is evident observing the frequency fluctuations in terms of frequency noise power spectral density (FNPSD) of the laser radiation, shown in Fig. 3.3. Making a comparison between the free-running and locked traces, it can be

observed how the fluctuations are reduced by ~ 4 orders of magnitude. QCL2 is operated at 318 K temperature and 473 mA current, delivering a measured output power of about 45 mW for the probe beam and 62 mW for the pump beam. The ultra-low-noise current driver ensures a current noise power spectral density below $1 \text{ nA}/\sqrt{\text{Hz}}$, while keeping a fast current modulation capability, thanks to a control circuit placed in parallel to the QCL based on a FET. The chosen molecular transition is the R(16)e of the $(02^0_1 - 02^0_0)$ ro-vibrational band of N_2O at $2209.0854 \text{ cm}^{-1}$ filled into a reference cell at the pressure of 0.4 mbar with an absorption path-length of 36 cm. The circularly polarized pump beam saturates the sample absorption and induces its birefringence. The probe beam undergoes a polarization rotation. The typical S-shaped dispersive profile is retrieved by a couple of mid-IR photodiodes in differential configuration. Placed behind a half-wave plate and a polarizing cube, they can detect any polarization rotation of the probe beam generating a zero-background signal. An optical isolator positioned on the probe beam optical path, picks up a portion of light which is sent to the detector for beating. In this way, such molecular-dip-locked QCL2 can be used as a master oscillator for the phase-locking scheme.

3.3.3 Beat note phase-locking

The beat note between the two frequency-locked lasers described before, allows both to refer QCL1 to the absolute frequency of QCL2 and to realize the frequency scan around the line of the $^{14}\text{C}^{16}\text{O}_2$ molecule. Thanks to the additional phase-locking system between the two lasers, the frequency of the QCL1 laser can be changed by scanning the cavity. A phase-lock is realized: the beat note measured by the detector is mixed with a variable known frequency produced by a synthesizer and then processed by an electronic phase-lock circuit (PLL), which sends the correction signal to the piezoelectric actuator of the high-finesse cavity. The QCL1, being locked to the cavity, follows the movements of the latter and therefore can scan around the target line without losing the frequency reference. The scheme realized for phase-locking the beat note is shown in the Fig. 3.4. To achieve long-term stability of the QCL1 frequency, we control the cavity length by phase-locking it to the stable reference described before. The beat note between QCL1 and QCL2 is detected by a fast (700 MHz bandwidth) HgCdTe photodiode and it is controlled by a local oscillator (RF synthesizer). The error signal is processed by a proportional-integral (PI) circuit and the correction is fed back to the PZT moving one of the cavity mirrors with a locking bandwidth of 500 Hz. This scheme, shown in Fig. 3.4, provides a cavity narrowed QCL1 traceable to the N_2O reference transition. By tuning the RF synth frequency, the cavity length is scanned across the $^{14}\text{C}^{16}\text{O}_2$ target line.

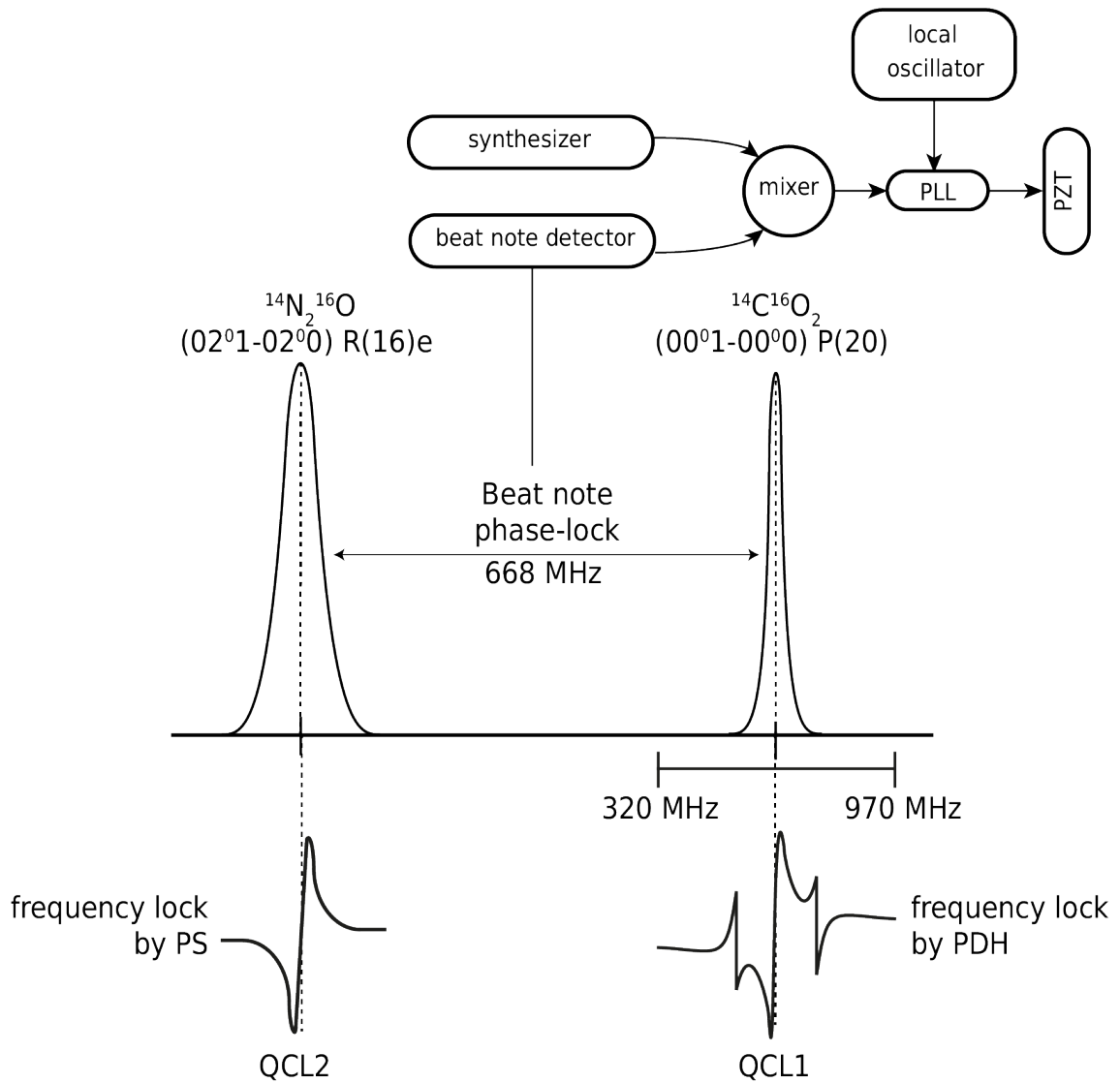


Figure 3.4: Scheme of the phase locking between the QCL1 and QCL2

3.4 Data acquisition and fitting procedure

The $^{14}\text{C}^{16}\text{O}_2$ concentration (x_0) is determined by measuring the spectral area of the P(20) line recorded by scanning the cavity frequency over 650 MHz across the line center, and by using the following equation:

$$x_0 \equiv \frac{P_0}{P} = \frac{1}{c^2 n_s} \frac{P_s}{P} \frac{T}{T_s} \frac{1}{S} \int \gamma_g(\nu; P_i, T) d\nu \quad (3.1)$$

being P the total CO_2 pressure, P_i partial pressures of all absorbing species (CO_2 isotopologues and any interfering trace gases) contained in the sample (P_0 for $^{14}\text{C}^{16}\text{O}_2$), T the absolute temperature, S the line intensity of the P(20) target transition (expressed in cm/molecule), ν the frequency (in Hz) and γ_g is the gas-induced decay rate. The Loschmidt density $n_s \sim 2.48 \times 10^{19} \text{ cm}^{-3}$ (the density of an ideal gas at standard thermodynamic conditions: $P_s = 1013.25 \text{ mbar}$ and $T_s = 296 \text{ K}$) and the speed of light c (in cm/s) are physical constants. Though the thermodynamic conditions (P,T) are measured with uncertainties better than 1‰, the line intensity (S) is known from theoretical calculations only, with uncertainty lower than 1% [69]. Therefore, the determination of the mole fraction from the measured spectral area of γ_g would be limited by the uncertainty of S . Nevertheless, by following a different approach, Eq. 3.1 can be used to compare the spectral area between each unknown sample and the reference standard to retrieve mole fraction ratios by means of a relative measurement:

$$\frac{x_{0,s}}{x_{0,srm}} = \frac{\int \gamma_{g,s}(\nu; P_i, T) d\nu}{\int \gamma_{g,srm}(\nu; P_i, T) d\nu} \quad (3.2)$$

where s indicates the sample and srm the standard reference material. This approach is justified since the thermodynamic conditions (P,T) and the line intensity are the same, within the instrumental uncertainty reported above, for the sample and the standard reference material. Furthermore the low temperature dependence of S ($1/S dS/dT \sim 2 \times 10^{-3} \text{ K}^{-1}$ at 170 K) does not affect the uncertainty of this relative measurement.

The ring-down signal is detected by an InSb photodiode (Detector 1 in Fig. 3.1), provided by Hamamatsu, amplified by means of a logarithmic amplifier, and digitized by a 18-bit, 10 MSample/s analog-to-digital converter (ADC, NI PXI-6250). Each measurement is processed by real-time fitting software. An acousto-optic modulator (AOM) is used to switch the light off in $\sim 100 \text{ ns}$ at the set cavity-filling threshold, thus starting the CRD events. Three back-and-forth stepwise scans of the QCL1 frequency across the target transition are performed for each acquisition. The typical back-and-forth scan spans 650 MHz, with 66 points spaced by 10 MHz, and takes about 4 min. For each frequency step, 3350 SCAR signals are acquired and averaged. These averaged SCAR decays are analysed with the effective saturation parameter Z_{1V} [70] for each scanned frequency. Hence, the gas-induced cavity decay rate γ_g is determined by averaging together the six values belonging to the single sweeps (three back and forth). The

acquired spectrum is fitted using three Voigt profiles. The three-line manifold appearing in the experimentally recorded spectrum is formed by the target line of $^{14}\text{C}^{16}\text{O}_2$ and two sets of interfering lines, belonging to N_2O and two different CO_2 isotopologues. The first set is formed by the unresolved $(05^5_1-05^5_0)$ P(19)e and $(21^1_1-21^1_0)$ P(23)e lines of $^{13}\text{C}^{16}\text{O}_2$ at 2209.1165 cm^{-1} , overlapped with the $(01^1_1-01^1_0)$ Q(12)e line of $^{14}\text{N}_2^{16}\text{O}$ at 2209.1144 cm^{-1} , and it lies within the scanned range. The other set lies just out of the scanned range and is formed by the unresolved $(02^2_1-02^2_0)$ P(30)e+f doublet of $^{13}\text{C}^{17}\text{O}^{18}\text{O}$ at 2209.1202 cm^{-1} . By cooling the sample cell from room temperature down to 170 K, the overall intensity of the $^{13}\text{C}^{16}\text{O}_2$ interfering doublet is greatly reduced from almost 2000 times the target line down to $\sim 1.5\%$ of it, whereas the overall intensity of the $^{13}\text{C}^{17}\text{O}^{18}\text{O}$ interfering doublet is reduced from almost 20 times the target line down to $\sim 10\%$ of it, anyway being much more detuned. Therefore, we can state that most of the residual spectral interference, at such a low operating temperature, comes from the $^{14}\text{N}_2^{16}\text{O}$ line. In the next section we described the sample preparation protocol, developed to reduce this interfering line down to few ppb. All the acquired data that will be shown in the next chapter are processed by a code written in Python language.

3.5 Sample preparation protocol and CO_2 extraction line

In order to determine the radiocarbon content in samples, a line for preparation and purification of the gaseous samples was set up and its operation parameters were carefully optimized to satisfy the known purity demand required by the C14-SCAR spectrometer [56]. This line allows to isolate and extract the isotopic mixture of gaseous CO_2 while avoiding contamination with spectral interfering molecular species, to reduce any possible systematic error below the measurement statistical uncertainty. With the aim of extracting the CO_2 molecules, an elemental analyser (EA) unit (Elementar mod. vario ISOTOPE cube) was installed. In parallel, several approaches were considered to eliminate the interfering molecules, from a chemical distillation method up to moving to a different target line (P(16) at $2212,628\text{ cm}^{-1}$). Among the various methods tested, photochemical purification with a laser source in the vacuum UV was the most effective. But after some changes made on the EA unit, initially purchased only for the extraction of CO_2 , we obtained the same result, i.e. the elimination of the interfering molecule directly in the sample preparation phase, considerably simplifying the overall process needed to estimate the amount of radiocarbon present in the sample. The experiment for the N_2O photodissociation will be treated in Appendix A. As we mentioned, the sample preparation protocol was developed for the purification of the extracted CO_2 , so as to ensure the removal of all interfering molecular species. In particular, nitrous oxide (N_2O), whose $(01^1_1 - 01^1_0)$ Q(12)e transition lies in the spectral range of investigation, close to the $(00^0_1 - 00^0_0)$ P(20) target transition of $^{14}\text{C}^{16}\text{O}_2$, was strongly abated, below few ppb. The performance of the extraction and of the developed purification protocol were validated

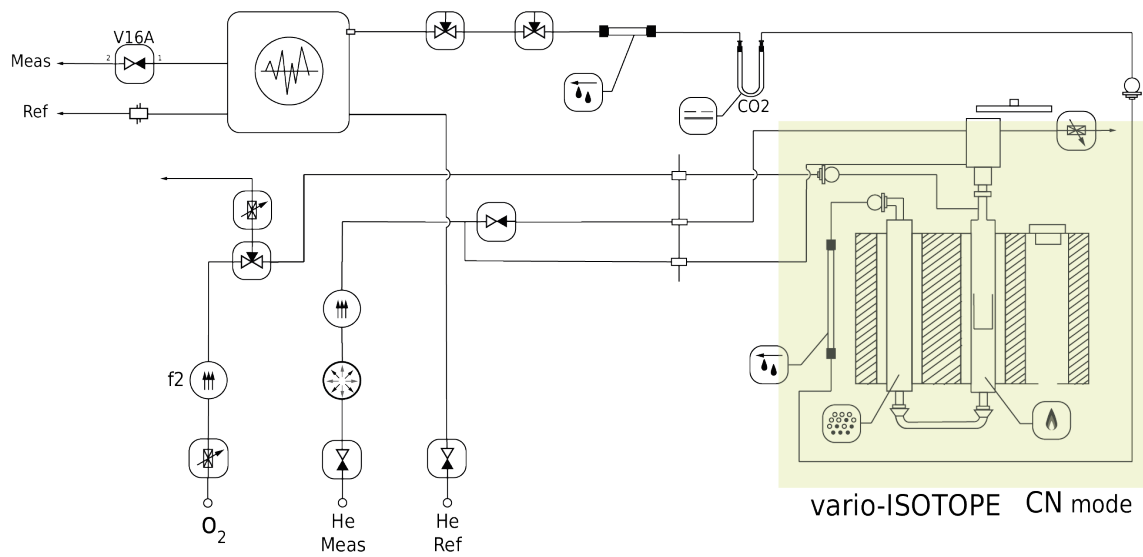
through measurements with the C14-SCAR apparatus.

The EA is an instrument for automatic and quantitative analysis of the elements C, H, N, S, O. The instrument can simultaneously determine the quantity of these elements starting weighed sample. It uses the advanced purge and trap (ATP) technology, a unique chromatographic technique for the quantitative separation of combustion gases, based on selective chemical absorbing traps. Moreover, this technology allows to avoid completely the problem of isotope fractionation (see Sec. 2.1), which can alter significantly the result of radiocarbon concentration measurements. The commercial EA was modified with the aim of optimizing the separation of the molecules involved in the considered samples, focusing on carbon and nitrogen bounding elements ("CN" mode), since the presence of any other compounds is not relevant in the spectroscopic analysis with the C14-SCAR system. In the following, the sample extraction by use of the EA set in CN operating mode will be described. The burning unit consists of four essential elements:

- Combustion column. Inside it, the combustion of the sample, including combustion catalysis, is realized.
- Reduction column. It binds the excess of oxygen, reduces NO_x to N_2 and binds volatile halogen compounds.
- Adsorption column. It provides the absorption and release of CO_2 .
- Thermal conductivity detector (TCD). It is used to quantitatively track all gas flows at the unit output (N_2 and CO_2 , in our case).

Furnace section

Fig. 3.5 shows an overview scheme of the instrument circuit. The light yellow shaded area represents the furnace section with three independent heaters. All heaters are temperature-monitored by the software. The combustion tube is located in the middle of the furnace and it is heated at the set point temperature of 900 °C. The reduction tube is located on the left and it is heated at the temperature of 550 °C. The third heater on the right is not used in this configuration. The substance digestion of the reaction gas mixture is divided into different phases. The atmosphere in the combustion column is enriched with oxygen that promotes the combustion of the sample. The elements, typically C, H, N and S, bound in the sample burn to form the following reaction products: CO_2 , H_2O , N_2 , NO_x , SO_2 , SO_3 . The combustion tube is filled with copper oxide which promotes the combustion of hardly combustible samples and silver wool which absorbs sulphur compounds. The carrier gas (He) flow transfers the gaseous combustion products into the reduction tube where the nitrogen oxides (NO_x) are reduced to N_2 at the copper contact and SO_3 is reduced to SO_2 . The H_2O in the reaction gas mixture is bound in an adsorption tube filled with Sicapent®. In CN mode only the carbon and



The following list names the functional and basic symbols:







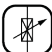





	Two-way valve		Drying		Pressure sensor
	Three-way valve		Combustion		Measuring cell
	Throttle		Reduction		Sensor
	Flow sensor		Gas separation		Actuator

Figure 3.5: **Functional diagram CN mode:** the yellow shaded area represents the furnace section of the EA unit

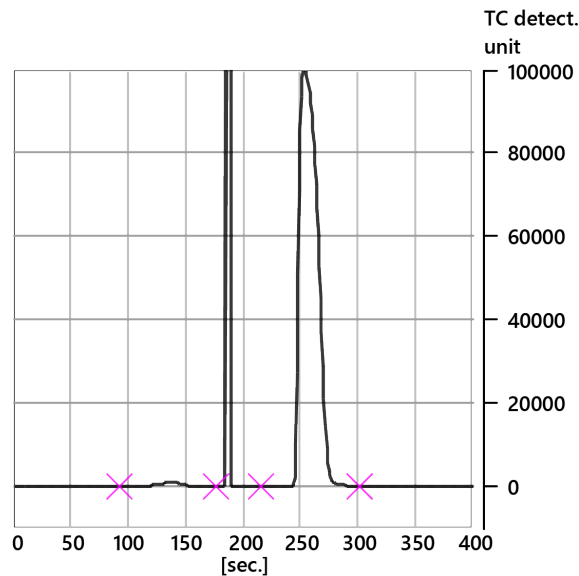


Figure 3.6: **Progression view of the components detected by the TCD of the EA unit:** it displays a graph of the time evolution of the output gases during the processing for the sample selected. The two peaks, each one delimited by two magenta crosses, represent the detected N_2 and CO_2 , respectively on the left and right hand side.

nitrogen bound elements are detected. Separation of the measured components takes place in the adsorption columns. N_2 is not absorbed when the adsorption column is at standby temperature ($25\text{ }^\circ\text{C}$), consequently it is the first measured component to enter in the TCD, while CO_2 is trapped in the adsorption column.

When the N_2 peak flow is detected, the temperature of the adsorption column is increased to induce CO_2 desorption (up to $240\text{ }^\circ\text{C}$), hence the CO_2 molecules are released and detected. The adsorption columns has a limited capacity to hold CO_2 , approximately 20 mg of corresponding carbon mass. After desorption from the adsorption column, the measured components are transported by the carrier gas flow into the measuring cell of the TCD. The thermal conductivity of the carrier gas sensibly changes under the addition of small amounts of foreign gases such as the measured components N_2 , CO_2 . If one of these measured components exists in the analysis gas mixture, this leads to a disturbance of the measuring bridge that is registered in the form of an electrical signal. The TCD measuring signal is digitized, integrated and output by the instrument to the PC, where it is registered in the form of a measuring peak dependent on time. The peak area is correlated with the absolute quantity of the respective measured component by calibration functions. An example of the progression vs. time of the detected components is reported in Fig. 3.6

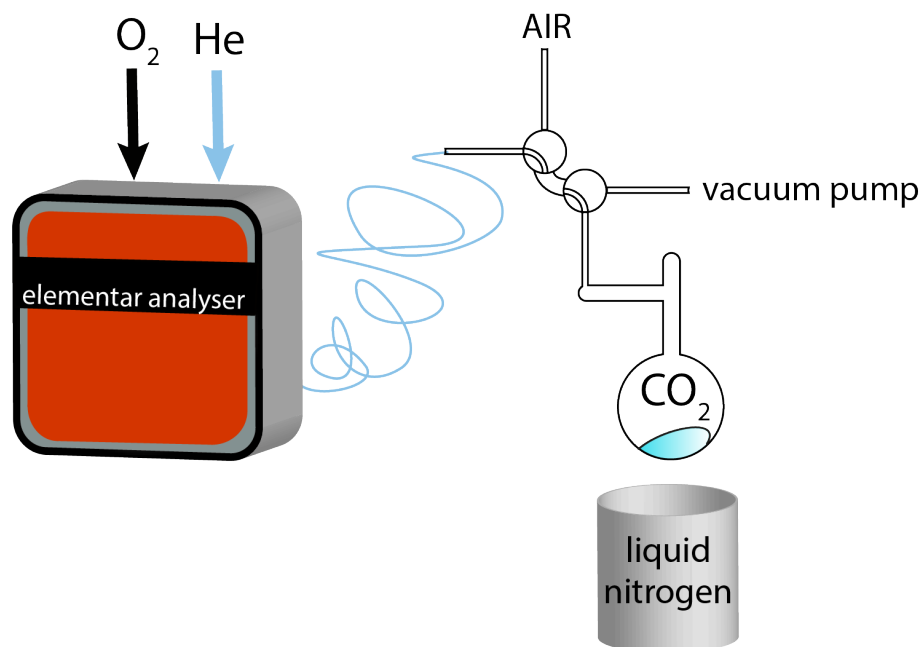


Figure 3.7: **Scheme of the realised CO₂ extraction line:** EA unit, the pre-evacuated circuit and the cryogenic trap

Samples characteristics

Carbon containing sample masses lying within the 16-20 mg range were used to produce the C14-SCAR CO₂ gas amount required for the measurements. Let us calculate the total sample carbon mass needed to fill the SCAR cavity, following the ideal gas law: $PV = nRT$, where P is the pressure inside the cavity (12.000 mbar), V is the volume of the cavity summed with the filling circuit (1.7 L), R is the molar ideal gas constant (83.1446 L mbar K⁻¹ mol⁻¹) and T is the cavity temperature (170 K). We found that our system requires a minimum sample carbon mass of 13 mg which will be scaled on the basis of the theoretical fractional carbon content of each investigated matrix.

Liquid samples are collected with a syringe (0.5 mL volume) while the solid samples by use of a steel spatula. All the samples are weighed by a balance with 0.01 mg precision, placed in a tin capsule of adequate volume and either packaged manually (if a solid sample is treated) or using a manual mechanical press that seals the sample capsule (if a liquid sample is treated). The capsule-containing sample is placed into the EA unit where the reaction occurs. The released CO₂ flows with the carrier gas (He) into the pre-evacuated collection circuit. A Schlenk flask (250 mL volume), equipped with a liquid-N₂ cryogenic trap, is placed at the end of the circuit. The solid CO₂ is collected into the flask and the carrier gas is removed by a turbo-molecular pump (HiCube 80 Eco, DN 40 ISO-KF, MVP 015-4). The collected gas is analysed by the SCAR technique to measure the ¹⁴C¹⁶O₂ concentration, expressed as a

percentage related to the standard. The described CO₂ extraction line is sketched in Fig. 3.7

4

Sample characterization by SCAR technique and results

With the aim to evaluate the ^{14}C content in unknown real-world samples, spectroscopic measurements by means of SCAR technique were performed. This content is determined by measuring the spectral area of the contribution (γ_g) to the CRD decay rate from the absorbing target (00⁰1-00⁰0) P(20) line of $^{14}\text{C}^{16}\text{O}_2$ at 2209.1077 cm^{-1} . The measurement is performed by a fitting procedure with a function defined as the sum of a linear baseline and three Voigt profiles, representing the $^{14}\text{C}^{16}\text{O}_2$ target line and two interfering lines attributed to $^{14}\text{N}_2^{16}\text{O}$ and $^{13}\text{C}^{17}\text{O}^{18}\text{O}$. This chapter is divided in four sections, each of them dedicated to a specific investigated matrix.

- **Biofuels.** In this section will be shown the results for the measurement of the ^{14}C content of two samples provided by Neste Corporation (labelled **Biofuel 1** and **Biofuel 2**), two samples provided by RISE: Research Institute of Sweden (labelled **Bio oil 1** and **Bio oil 2**) and two samples obtained from CSV-AM: Centro Sperimentale di Volo, Aeronautica Militare (labelled **Avionic jet fuel (Jet A1)** and **Biofuel blend**).
- **Polymers.** In this section three samples of polymer provided by RISE (labelled **Bio polymer 1**, **Bio polymer 2**, **Polymer 3**) will be under analysis.
- **Enriched graphite.** This sample comes from the Ispra cyclotron. Actually, the Joint Research Centre (JRC) of Karlsruhe (Germany) sets the EU standards for the decommissioning of nuclear power plant operations.

- **Archaeological samples.** Here we will present measurements on two charcoal samples coming from a NE area of Abu Tbeirah. They were provided thanks to a collaboration between our research group and the Dept. Institute of Oriental Studies, Sapienza Università di Roma.

To obtain an estimate of the radiocarbon content in each sample, a relative measurement was performed by comparing it with a standard reference material. Oxalic acid dihydrate ($C_2H_2O_4 \cdot 2H_2O$) provided by NIST (SRM 4990C), with known carbon mass content of approximately 19% and a ^{14}C content of 134.06 pMC, was chosen for all the samples except for those provided by CSV-AM. These measurements are compared with another sample certified by CSV-AM to be 100% biogenic avionic fuel. The statistical error for each measurement is reported as standard deviation calculated on the averaged residuals.

The measurement is performed starting from the extraction of CO_2 obtained by combustion of the sample. The required mass of each sample is collected into a tin capsule used for its combustion by means of the elemental analyser (Elementar, mod. vario ISOTOPE cube). The CO_2 extracted by the ATP mechanism described in Sec. 3.5, implemented inside the Elementar system, was condensed into a flask of 250 mL volume by means of a liquid-nitrogen bath (cooling bath). The described operation was performed for each sample. No treatment-related systematic effects were observed during the extraction phase, and the spectrum resulting from each measurement does not show any interfering signal, except for negligible traces of N_2O . The isotopic mixture of the extracted CO_2 is inserted, after adequate vacuum creation, into the SCAR cavity to perform the measurement of $^{14}CO_2$ concentration in static conditions.

4.1 Evidence of the role of the sample preparation

Through an in-depth study of the sample preparation conditions, we identified the parameters required to optimize the extraction of CO₂ and minimize pollution from interfering gases. The critical factors in this operation are the correct validation of the release times, hence the CO₂ capture and the ratio between the mass of the matrix subjected to combustion (sample) and the maximum amount of carbon that can be burnt by the EA unit. The SCAR technique measures the ¹⁴C content in a CO₂ isotopic mixture obtained by burning the sample under test, as it was described in Sec. 3.5. The elimination of interfering molecules was possible by use of a commercial elemental analyser able to oxidize the carbon content of the sample and to selectively extract only CO₂ from the gas mixture. In this section we will present different solutions devised to eliminate most of interfering molecules. Thanks to the developed protocol described, the reduction (down to few ppb) of the (01¹1 – 01¹0) Q(12e) line of nitrous oxide ¹⁴N₂¹⁶O was demonstrated. This unearthed a new line, shown in Fig. 4.1, that lies just out of the scanned range, formed by the unresolved (02²1-02²0) P(30)e+f doublet of ¹³C¹⁷O¹⁸O at 2209.1202 cm⁻¹ [71]. Although the overall intensity of the interfering doublet is reduced by almost twenty times the target line, down to ~10% of it, by cooling the sample cell from room temperature down to 170 K, we had to include this line to get a three Voigt profile fit function. Another effect of the sample preparation on the SCAR spectrum was observed. It is

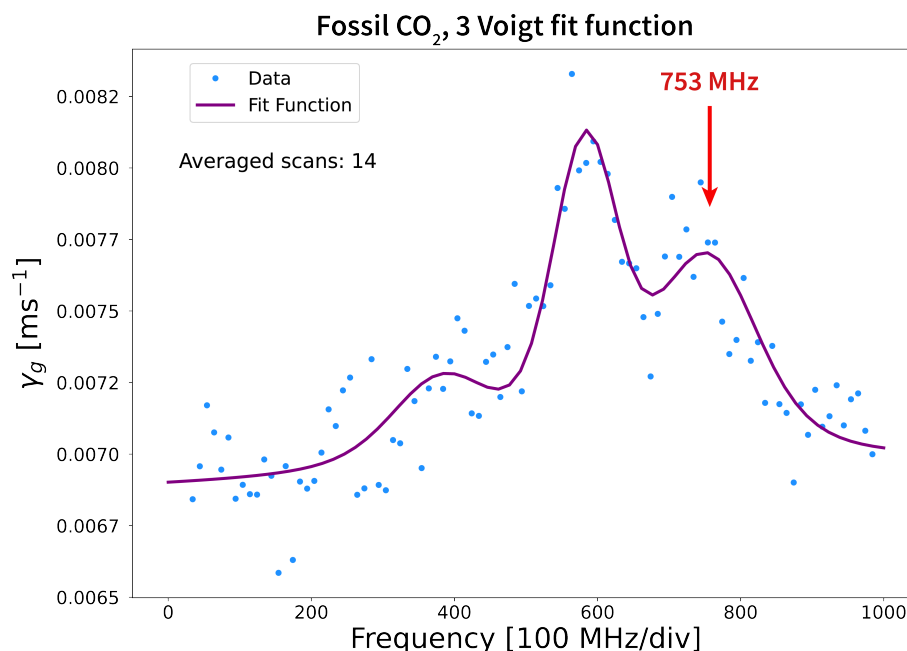


Figure 4.1: **SCAR spectrum of fossil CO₂ recorded 1000 MHz.** The labelled line (red row) at 753.5 MHz represents the unresolved (02²1-02²0) P(30)e+f doublet of ¹³C¹⁷O¹⁸O at 2209.1202 cm⁻¹

related to the maximum mass that can be burnt by means of the combustion unit. This effect was observed mainly for samples of fuel. The overall capacity of the adsorption column (see section protocol) equipped inside the elemental unit is 20 mg of carbon. Beyond this value the system saturates. Moreover, it was observed that a mass too large results in an additional complexity to control the CO₂ extraction process. One of the hypotheses made relates to the possibility that the combustion is incomplete, with a residue of unknown un-combusted chemical species (probably shorter chain hydrocarbons), when the mass of the sample already exceeds 10 mg. Considering that the carbon content in of hydrocarbons is about 80-90% of the total mass and that the C14-SCAR spectrometer requires about 13 mg of C for each measurement, an overall mass of ~ 16 mg was estimated to extract the needed amount of CO₂ to fill the SCAR optical cavity. We notice that, burning the overall mass in only one fraction, produces an unidentified line that is observable only in the spectrum of the empty cavity decay rate γ_c as shown in the top right graph of Fig. 4.2. It means that this species has a non-saturable absorption, hence it is not observable in the γ_g spectrum. Since a certain degree of correlation exists between γ_c and γ_g , this effect may compromise the measurement of the carbon content in the investigated sample, with a systematic increase in the value of the spectral area of ¹⁴CO₂. Fig. 4.2 shows the spectra of the same sample obtained by burning the overall mass of ~ 16 mg in either one shot or two shots of ~ 8 mg each. The effect on the gas contribution spectrum consists in an unwanted systematic drop of the γ_g plot at lower frequencies (top left graph in Fig. 4.2), that compromises the accuracy in the determination of the carbon content in the sample.

4.2 Raw data: ratios of unknowns to standards

Both decay counting and AMS measurements can give rise to artefacts that may cause the measured activity or isotope ratio to differ from the actual value. Such systematic errors can include counter efficiency and quenching (for decay counting) and uncertainties in the calibration of the current measurement device (for AMS). These errors make it very difficult to accurately measure activity or isotopic ratio, which is why ¹⁴C measurements rely on the parallel measurement of an internationally accepted standard, just like is done for stable isotope measurements. The assumption is that any systematic alteration of the isotopes by sample preparation or decay counting methods will be the same for the standard and the sample. Likewise, the SCAR spectrum could be affected by systematic effects possibly related to the lineshape of the measured spectrum, i.e. small deviations from a perfect Voigt profile. This suggests to calibrate SCAR measurements. Consequently, the ratio between the sample and a standard will be measured accurately.

The first modern ¹⁴C standard was NIST (National Institute of Standards and Technology) Oxalic Acid or OX-I (C₂H₂O₄), made from a crop of sugar beets collected in the year 1955. The absolute ¹⁴C standard has ninety-five percent of the activity of OX-I, measured in the year

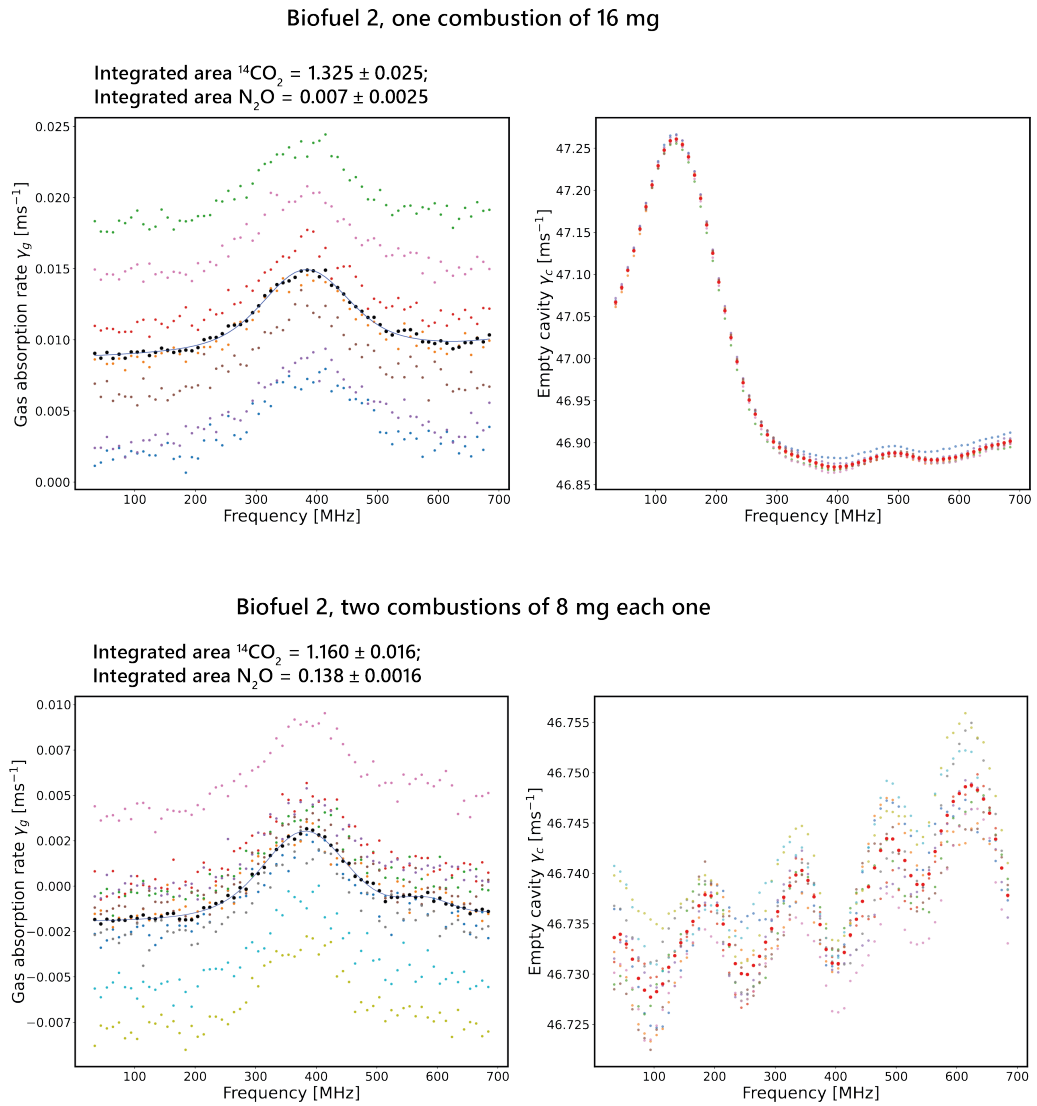


Figure 4.2: Spectra of γ_g (left hand side) and γ_c (right hand side) for **Biofuel 2** realized starting either from a single combustion of 16 mg of sample (on the top) or from 2 combustions of 8 mg each one (on the bottom)

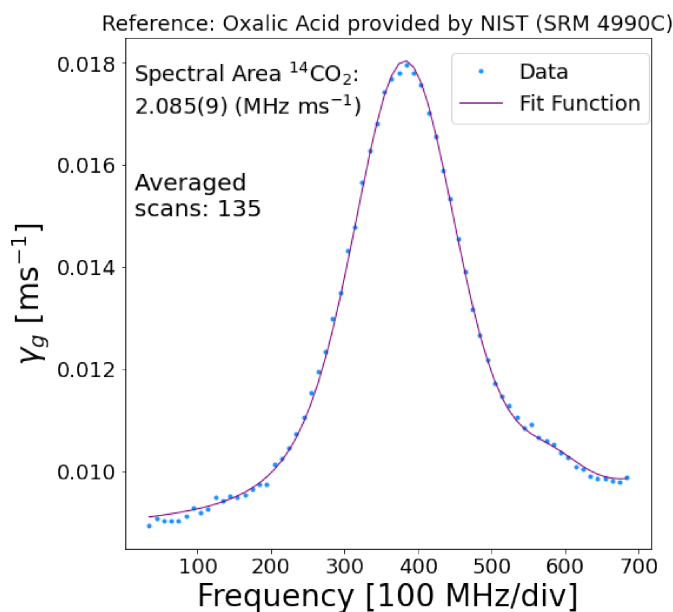


Figure 4.3: Oxalic Acid (standard Ox-II SRM 4990C) spectrum performed by C14-SCAR apparatus

1950. The New Oxalic Acid standard (NOX) was introduced in 1980 to replace the primary Ox-I standard by the National Bureau of Standards (NBS). Actually, it is available from the NIST as SRM-4990C, while the original OX (SRM-4990B) is no longer available. The NOX standard was calibrated against the OX-I by decay measurements in several laboratories. The accepted consensus value is 1.2736 ± 0.0004 for the ratio of NOX normalised to $\delta^{13}\text{C}$ of -25 ‰ over OX normalised to $\delta^{13}\text{C}$ of -19 ‰ . This resulted in a nominal ^{14}C of $134.066 \pm 0.043 \text{ pMC}$ for NOX. Fig. 4.3 shows the spectrum of standard reference material oxalic acid (SRM-4990C). We perform 135 measurements which averaged together give an integrated area of $2.085 \pm 0.009 \text{ MHz ms}^{-1}$.

4.3 Biofuel samples investigated by C14-SCAR spectrometer

Currently, among the different biofuel production pathways for avionic transport use (e.g. approved for blending with jet kerosene), hydroprocessed esters and fatty acids (HEFA) fuels are technically mature and commercialised. On the other hand, the thermochemical conversion of biomass is considered the most viable and emerging technology for the production of biofuels, due to its simplicity, cost-effectiveness, and feedstock flexibility. Particularly, pyrolysis is the most efficient route, by which bio-waste can be thermally degraded to produce bio char (solid), bio oil (liquid), and gaseous fuel. Due to their low energy density (compared to fossil fuels), pyrolysis oils are used in stationary engines, boilers and for heating. This

section will show measurements performed on different fuel samples, namely blends of HEFA aviation fuel with Jet A1 fossil fuel and bio-oil derived by pyrolyzed biomass, to demonstrate the accuracy achieved by the SCAR technique in the determination of the biogenic fraction in fuel blends. This accuracy evaluation was carried out by using both AMS, as primary verification method, and direct mass mixing ratio (MMR), as independent cross check. Indeed, the measured ^{14}C contents of avionic fuel blends **Biofuel 1**, **BioFuel 2** (provided by Neste Corporation) and upgraded pyrolysis **Bio oil 1**, **Bio oil 2** (provided by RISE: Research Institute of Sweden) were compared to AMS results, with the aim of testing the SCAR technology accuracy. Afterwards, avionic fuel blends **Avionic jet fuel (Jet A1)**, **Biofuel blend** (provided by CSV-AM: Centro Sperimentale di Volo, Aeronautica Militare), prepared with fixed biogenic/fossil composition by mixing precisely measured mass ratios, were analysed by using the SCAR technique. For each sample, the measurement is performed starting from an extraction of CO_2 obtained by combustion of the liquid fuel. The sample is collected into two tin capsules of ~ 8 mg each. The isotopic mixture of the extracted CO_2 is inserted into the SCAR cavity to perform the spectroscopic measurement of $^{14}\text{CO}_2$ concentration in static conditions. Though the SCAR measurements were performed on samples with different ^{14}C mole fraction, no memory effect was observed within our precision, thus confirming that the chosen material for the cell of the SCAR cavity was suitable.

Biofuel samples compared with the standard reference material (SRM 4990C)

Fig. 4.4 shows the experimental results obtained for the measured biogenic content in four samples of biofuel compared with the standard reference material. The ^{14}C content is determined by averaging ten single measurements for each sample. For each single measurement, the SCAR cavity was scanned six times (three back-and-forth) across the target transition (at 2209.1077 cm^{-1}). All the results are expressed in pMC, with an uncertainty of about 1 pMC, by taking the ratio between the spectral area of the target line (light green shaded region) and the spectral area of the reference oxalic acid standard (beige shaded region), which is plotted in the background. These blends of liquid fuels were also measured by AMS facilities. All fit residuals, plotted in Fig. 4.4 below the measured spectra, appear to be randomly distributed, without any visible hint for either an inaccurate lineshape model or missing lines. As for the N_2O interfering line on the right hand side of the target line, its spectral area is almost negligible, except in the case of highly ^{14}C -depleted samples, such as **Biofuel 1**. Indeed, any possible systematic effect on the measured spectral area of the target line, resulting from its partial overlap with the N_2O line, was not observed for such low residual concentrations of this interfering species (below few ppb). The results obtained for this four samples were validated by performing AMS measurements. Table 4.1 summarizes our results and compares them with those obtained by AMS. For each sample, the biogenic content measured by C14-SCAR shows a good agreement with the expected value, within its experimental uncertainty.

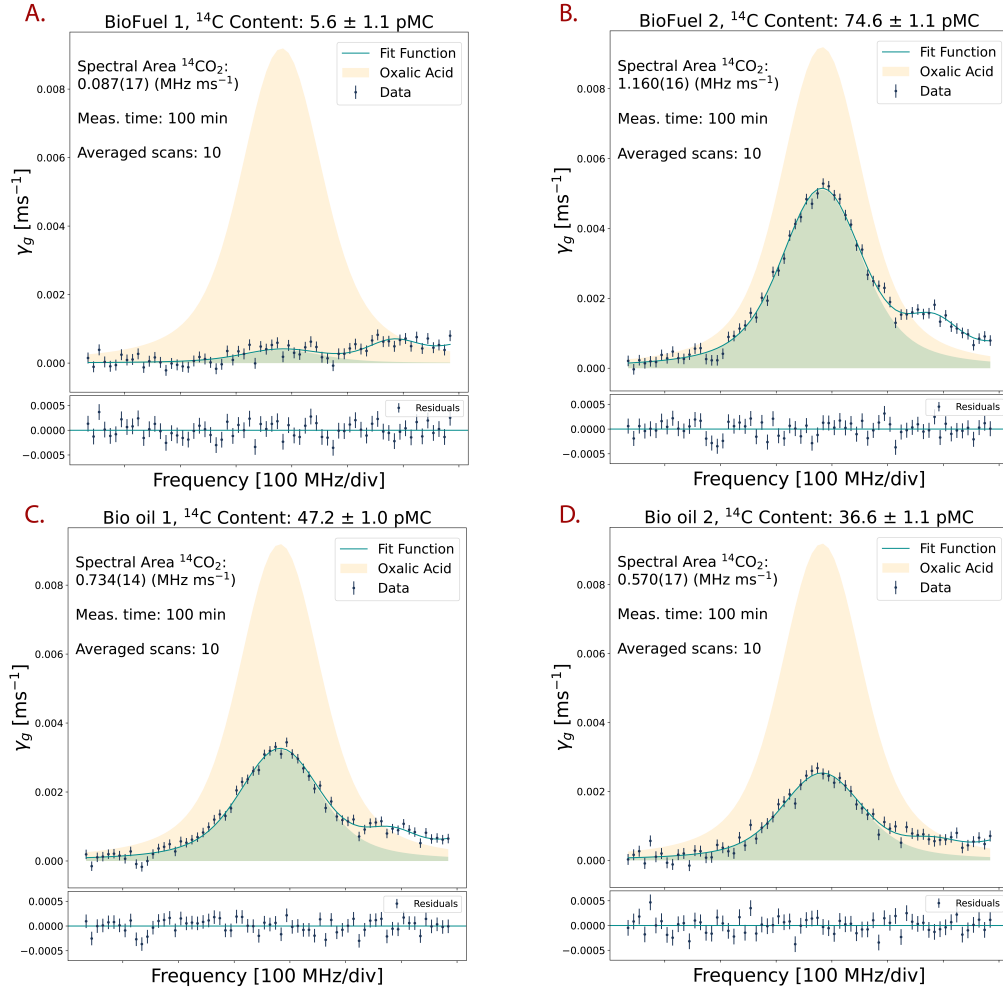


Figure 4.4: **Radiocarbon content measured by the C14-SCAR spectrometer in fuel blends** made from biogenic HEFA and fossil Jet A1 (**Biofuel 1** and **Biofuel 2**, A and B graph respectively) and samples made by thermochemical conversion of biomass (**Bio oil 1** and **Bio oil 2**, C and D graph respectively). Both of them are compared to oxalic acid reference material (beige shaded area). Error bars represent $1 - \sigma$ standard deviation.

Sample	SCAR result (pMC)	AMS result (pMC)
Biofuel 1	5.6 ± 1.1	4.7 ± 0.2
Biofuel 2	74.6 ± 1.1	74.0 ± 0.1
Bio oil 1	47.2 ± 1.0	47.0 ± 1.5
Bio oil 2	36.6 ± 1.1	38.0 ± 1.5

Table 4.1: Comparison between SCAR and AMS measurement results for the sample shown in Fig. 4.4

Biofuel samples compared with a 100% biofuel reference

Fig. 4.5 shows the experimental results obtained for the measured biogenic content in two more samples, **avionic jet fuel** and **biofuel blends**, within the CNR-INO project "Aerotrazione con BioCarburanti (ABC)" funded by Ministero dell'Ambiente e della Tutela del Territorio e del Mare (MATTM). They are biogenic HEFA and fossil Jet A1 mixed in different amounts, with known mass mixing ratio (MMR). The measurement was performed as described before. Both the results are expressed in % of biogenic content with an uncertainty of about 1% by taking the ratio between the spectral area of the target line (beige shaded region) and the spectral area of the reference 100% biogenic avionic fuel (light green shaded region), which is plotted in the background. The ^{14}C content of this reference fuel was also measured, resulting to amount to 98.2 ± 1.1 pMC. Such a slight difference with the 100 pMC value is not surprising, since, due to combined bomb peak and Suess effects, discussed in Sec. 2.3, the ^{14}C content depends, even for very recent samples, on the specific year of death of the biogenic material employed to produce the fuel itself. Table 4.2 summarizes our results expressed in % of biogenic fraction

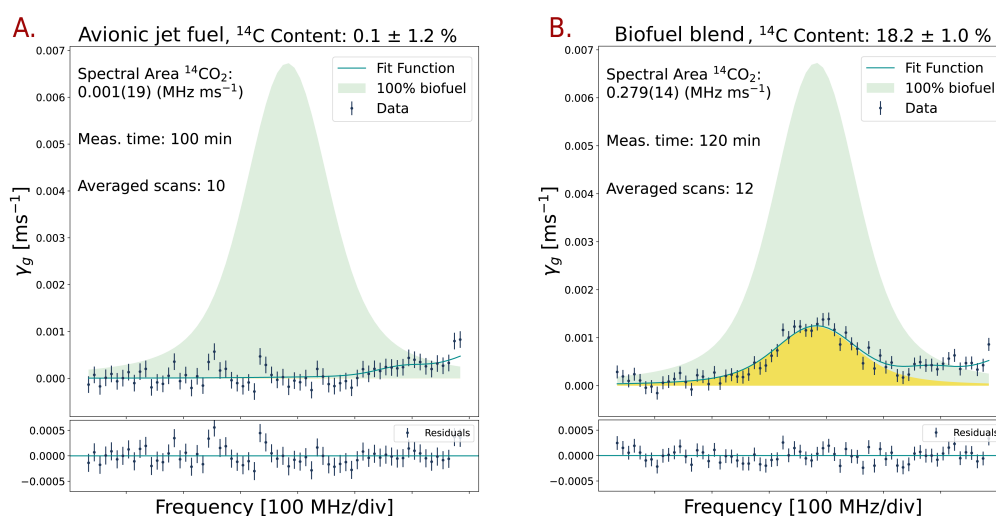


Figure 4.5: Radiocarbon content measured by the C14-SCAR spectrometer in a sample of **avionic jet fuel**, labelled E) and a biofuel blend made from biogenic HEFA, with known MMR (**biofuel blend**, labelled F). Both of them are compared to 100 % biogenic avionic fuel (light green shaded area). Error bars represent $1 - \sigma$ standard deviation.

contained in the two samples shown in Fig. 4.5, compared with the mixing values chosen to prepare the blends. For each sample, the biogenic content measured by C14-SCAR shows a good agreement with the expected value, within its experimental uncertainty.

Sample	SCAR result (%)	MMR (%)
Avionic jet fuel	0.1 ± 1.2	0.0 ± 0.0
Biofuel blend	18.20 ± 1.0	18.98 ± 0.01

Table 4.2: Comparison between SCAR measurement and known MMRs of the samples shown in Fig. 4.5

4.4 Biopolymer samples investigated by the C14-SCAR spectrometer

As it was discussed in Sec. 2.4.3, the field of biobased materials is growing strongly both in chemical sector (e.g. biosolvents, biocatalysts, biofibers) and in terms of commonly used materials (such as biocosmetics and biopolymers). Bio-based materials, such as biopolymers, are totally or partly derived from materials of biological origin, thus excluding materials embedded in geological formations and/or fossilised. In industrial processes, enzymes are used in the production of chemical building blocks, detergents, pulp and paper, textiles, etc. By using fermentation and bio-catalysis instead of traditional chemical synthesis, a higher process efficiency can be obtained, resulting in a decrease in energy and water consumption, and a reduction of toxic waste. Raw materials of biological origin are recyclable for a brief period (less than 10 years), differently from those fossil-based. Therefore, bio-based products can make a significant contribution to reduce CO₂ emissions and offer other advantages, such as lower toxicity or novel product characteristics (e.g. biodegradable plastic materials). The determination of radiocarbon content can play a relevant role in certifying “green” products, which is currently considered a subject of great interest. With the aim of demonstrating the applicability of the SCAR technique to certification of bio-based materials, three different polymers with unknown biogenic content were analysed. Also in this case, the accuracy evaluation was performed by using AMS. Indeed, the measured ¹⁴C contents of **Biopolymer 1**, **Biopolymer 2** and **Polymer 3** (provided by RISE: Research Institute of Sweden) were compared to AMS results, with the aim of testing the SCAR accuracy. For each sample, the measurement was performed starting from the extraction of CO₂ obtained by combustion of the polymeric material. Each sample was collected into three tin capsules of ~ 7 mg each. The isotopic mixture of the extracted CO₂ was inserted into the SCAR cavity to perform the spectroscopic measurement of ¹⁴CO₂ concentration in static conditions.

Fig. 4.6 shows the experimental results obtained for the measured biogenic content in three samples of biopolymers compared with the standard reference material (NOX SRM-4990C). The ¹⁴C content was determined by the average of ten single measurements for each sample, corresponding to ~ 2 hours of total averaging time. Also in this case the SCAR cavity was scanned six times across the target transition, for each single measurement. The results

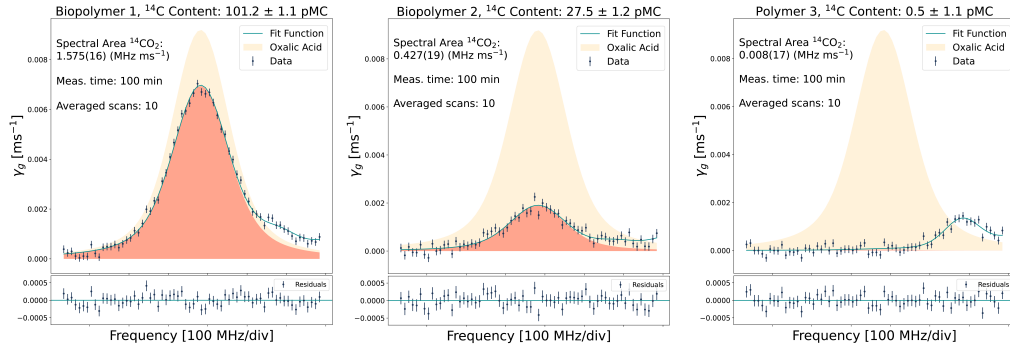


Figure 4.6: Radiocarbon content measured by the C14-SCAR spectrometer in three sample of polymers (orange shaded area). Both of them are compared to oxalic acid reference material (beige shaded area). Error bars represent $1 - \sigma$ standard deviation.

Sample	SCAR result (pMC)	AMS result (pMC)
Biopolymer 1	$101.2 \pm 1,1$	100.0 ± 1.5
Biopolymer 2	$27.5 \pm 1-2$	28.5 ± 1.5
Polymer 3	0.5 ± 1.1	0.01 ± 1.5

Table 4.3: Comparison between SCAR and AMS measurements results for samples shown in Fig. 4.6

are expressed in pMC, with an uncertainty of about 1 pMC, by taking the ratio between the spectral area of the target line (orange shaded region) and the spectral area of the reference standard (beige shaded region). The residuals do not show an inaccurate lineshape model or missing lines. As it was suggested in the precedent case of biofuel measurements, the N_2O interfering line on the right hand side of the target line has a negligible spectral area, except in the case of highly ^{14}C -depleted samples, such as **Polymer 3** which has no biogenic content. Therefore, any possible systematic effect on the measured spectral area of the target line was not observed. The comparison between the SCAR measurement and AMS is shown in table 4.3. For each sample, the biogenic content measured by C14-SCAR shows a good agreement with the expected value, within its experimental uncertainty.

4.5 Enriched samples investigated by the C14-SCAR spectrometer

The Joint Research Centre (JRC) belongs to the European Commission's science and knowledge service. Its mission is to support EU policies with independent evidence throughout the whole

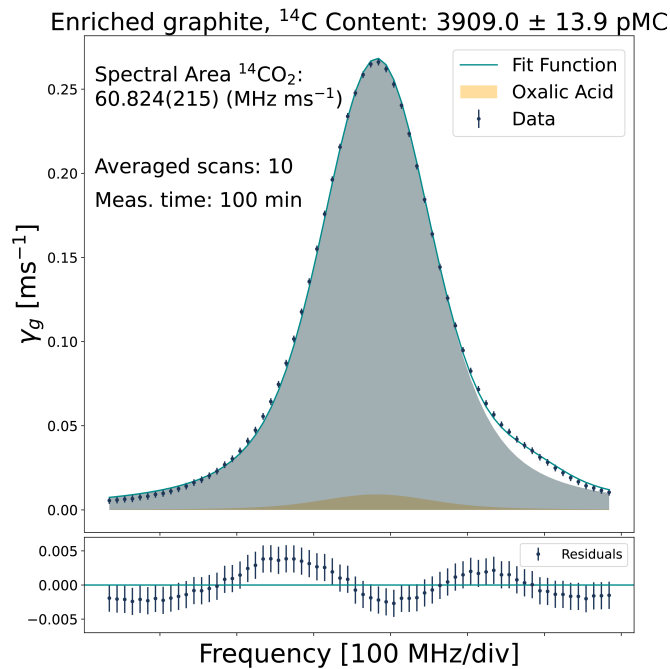


Figure 4.7: Radiocarbon content measured by the C14-SCAR spectrometer in a sample of graphite (gray shaded area) compared to oxalic acid reference material (beige shaded area). Error bars represent $1 - \sigma$ standard deviation.

policy cycle. The so called Directorate of Nuclear Safety and Security, under which the nuclear work program of the JRC lies, is sponsored by the EURATOM Research and Training Program. It contributes to the scientific foundation for the protection of European citizens against risks associated with the handling and storage of highly radioactive material. Moreover, it provides scientific and technical support for the conception, development, implementation, and monitoring of community policies related to nuclear energy. Their research and policy support activities contribute to the achievement of effective safety and protection systems for the nuclear fuel cycle and to the enhancement of nuclear security, thus contributing to the achievement of the low carbon energy production goal. The sample investigated in this section is a piece of nuclear grade graphite coming from the reactor of the cyclotron of the JRC-Ispra that now is in the decommissioning phase. The irradiation time of this sample is unknown.

The ^{14}C content of this sample was determined starting from the extraction of CO_2 obtained by combustion of graphite dust. Since the carbon content in graphite is 100 %, the sample was collected into three tin capsules of ~ 7 mg each. The isotopic mixture of the extracted CO_2 is inserted into the SCAR cavity to perform the spectroscopic measurement of $^{14}\text{CO}_2$ concentration in static conditions. The results obtained for the measurement of ^{14}C content

in enriched graphite, compared with the standard reference material, is shown in Fig. 4.7. The ^{14}C content is determined by the average of ten single measurements, for each one of which the SCAR cavity was scanned six times across the target transition. The result is expressed in pMC, by taking the ratio between the spectral area of the target line (grey shaded region) and the spectral area of the reference standard (beige shaded region), which is plotted in the background. The sample resulted to be enriched ~ 39 times more than the natural abundance. This was one of the first samples that we measured and, at that time, the sample preparation protocol was not optimized, yet. Indeed, we can notice the presence of the interfering N_2O line at higher frequency (2209.1144 cm^{-1}). Moreover, we fit our spectrum using a Voigt profile. As it was demonstrated [70], this function is not suitable when the radiocarbon content is much higher than natural abundance since the signal to noise ratio is very high. This systematic error dominates the statistical one and it results evident observing the fit residuals. The comparison with AMS is still to be done.

4.6 Archaeological samples investigated by the C14-SCAR spectrometer

In this section, the results obtained by measuring two ancient charcoal samples **AbT5** and **AbT6** will be shown. They come from the first campaign of excavations carried out by an Italian-Iraqi team, directed by Franco d'Agostino and Licia Romano from dept. Institute of Oriental Studies, Sapienza Università di Roma. The preliminary project, which led to the first campaign for the site of Abu Tbeirah (southern Iraq) in 2012, was intended as a first step toward the normalization of the activities of the State Board of Antiquities and Heritage at Nasiriyah, after the long period of standstill started with the first Gulf War (Desert Storm) in 1991. The site, officially spelled Abu Tubairah, is known popularly as the 'Ibrahim's Mounds' and is located 7 km South of Nasiriyah, near the ancient coastline of the Arabian Gulf, in a petrol area known as Ar-Rafidayn. Indeed, its surface is disturbed by modern activities connected with petrol and gas exploitation [72]. The charcoal sample has been found inside a grave (Grave 1 NE) in the North-Eastern area of Abu Tubairah. On the base of taphonomic and stratigraphic evidence, the date of the discovered graves has been preliminary established to the Akkadian period (2350-2200 BC).

Before the measurement, each sample must be treated to remove exogenous carbon incorporated on or within the material. A common pretreatment for many organic matter samples that most laboratories worldwide use is the well-known *ABA* (acid-base-acid) procedure. Although this pretreatment is relatively straightforward, there is no consensus among labs about the optimal strength of the chemical solutions, or even the temperature, used for such chemical digestions. For our samples, this procedure was provided by LABEC (Laboratory of nuclear techniques for the Environment and Cultural Heritage) at the INFN section of Florence. During such pretreatment, samples are initially washed using weak acid (HCl 1M)

and base (NaOH 0.1M) in order to remove secondary carbon-containing species, such as carbonates and acids that might have accumulated on the sample. These washes are followed by a final acid bath (HCl 1M), designed to remove any CO₂ absorption that may have occurred when the samples were submerged in the base solution.

The measurement is performed starting from an extraction of CO₂ obtained by combustion of the charcoal samples. For each sample we made three single combustions of ~ 8 mg each. The isotopic mixture of the extracted CO₂ was inserted into the SCAR cavity to perform the spectroscopic measurement of ¹⁴CO₂ concentration in static conditions. Fig. 4.8 shows the

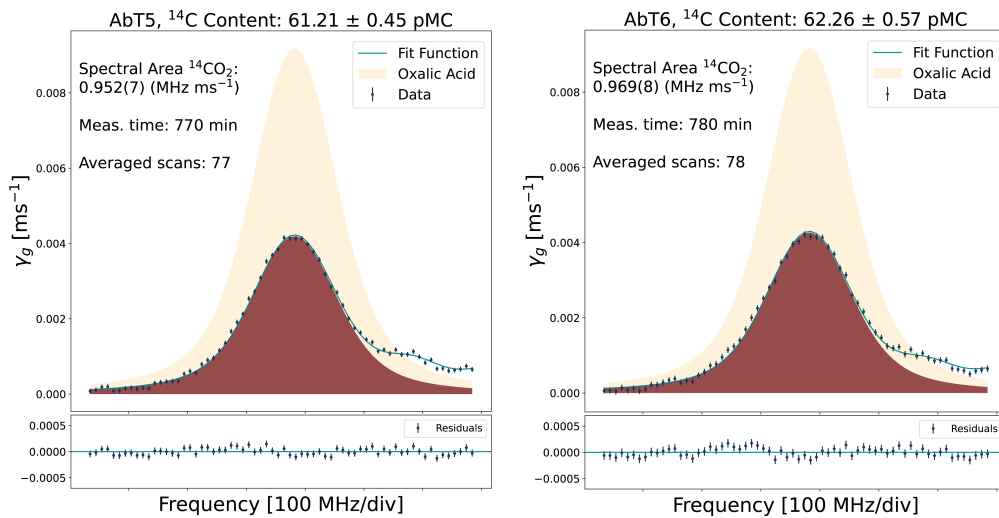


Figure 4.8: Radiocarbon content measured by the C14-SCAR spectrometer in ancient charcoal sample **AbT5** and **AbT6**. Both of them are compared to oxalic acid reference material (beige shaded area). Error bars represent $2 - \sigma$ standard deviation.

results obtained for the measured ¹⁴C content in two charcoal samples, **AbT5** and **AbT6**, compared with the standard reference material (NOX SRM-4990C). It is determined by the average of 77 single measurements for the sample **AbT5** and 78 single measurements for the sample **AbT6**. As it can be noticed, increasing the integration time corresponds to decreasing the uncertainty value, which scales as $1/\sqrt{n}$. Normally the accurate age determination of a sample requires a correction for the isotope fractionation (this aspect is treated in Sec. 2.3). This depends on the relative difference (in ‰ units) between the ¹³C/¹²C isotopic ratio of the sample and that of a standard reference material. Moreover, it can be assumed that the fractionation of the ¹⁴C isotope is double that of ¹³C. Unfortunately, we were unable to measure $\delta^{13}\text{C}$, but tabulated values can be used for the correction, although these values are often contradictory in the literature [73]. Since the mean of $\delta^{13}\text{C}$ in charcoal samples is -25.7 ‰ and the corresponding value for the reference standard is -25.0 ‰, referring to the Eq. 2.4, we should correct our results by -1.4 ‰. This value falls within our error bar.

Sample	SCAR result (pMC)	AMS result (pMC)	SCAR t_{rC} (BP)	AMS t_{rC} (BP)
AbT5	61.21 ± 0.45	61.25 ± 0.36	3943 ± 59	3938 ± 47
AbT6 2	62.26 ± 0.57	61.76 ± 0.51	3806 ± 74	3971 ± 66

Table 4.4: Comparison between SCAR and AMS measurement results of samples shown in Fig. 4.8

Therefore, although it is a systematic deviation, we did not consider necessary to apply this correction. The comparison between the SCAR measurement and the one from AMS (Labec - INFN, Florence) is shown in table 4.4.

In this case, two more columns are added. The value t_{rC} corresponds to the conventional radiocarbon age, a standard way for reporting dating in years before the present (BP). A few assumptions are implicit in the citation of a conventional radiocarbon age: the Libby half-life for ^{14}C of 5568 years is used, AD 1950 is the reference year zero and radiocarbon years BP are the units used to express the age calculated as:

$$t_{rC} = \tau \ln \left(\frac{{}^{14}R_0}{{}^{14}R_t} \right) \quad (4.1)$$

where τ is the mean life of ^{14}C using the Libby half-life (8033 years), R_0 and R_t are the ^{14}C content in the standard and in the samples respectively. This value must be converted to calendar age equivalents using a calibration curve compensating for fluctuations in atmospheric ^{14}C concentration in the Northern Hemisphere [74]. The IntCal Working Group (IWG) has endeavoured to provide ^{14}C calibration curves at semi-regular intervals since 2004. With the aim of converting the conventional radiocarbon age measured for samples **AbT5** and **AbT6** to a true probable age, the measured t_{rC} was calibrated by use of the software OxCal 4.4 with the newly calibrated curve IntCal20 as reference. In Fig. 4.9 our results are reported.

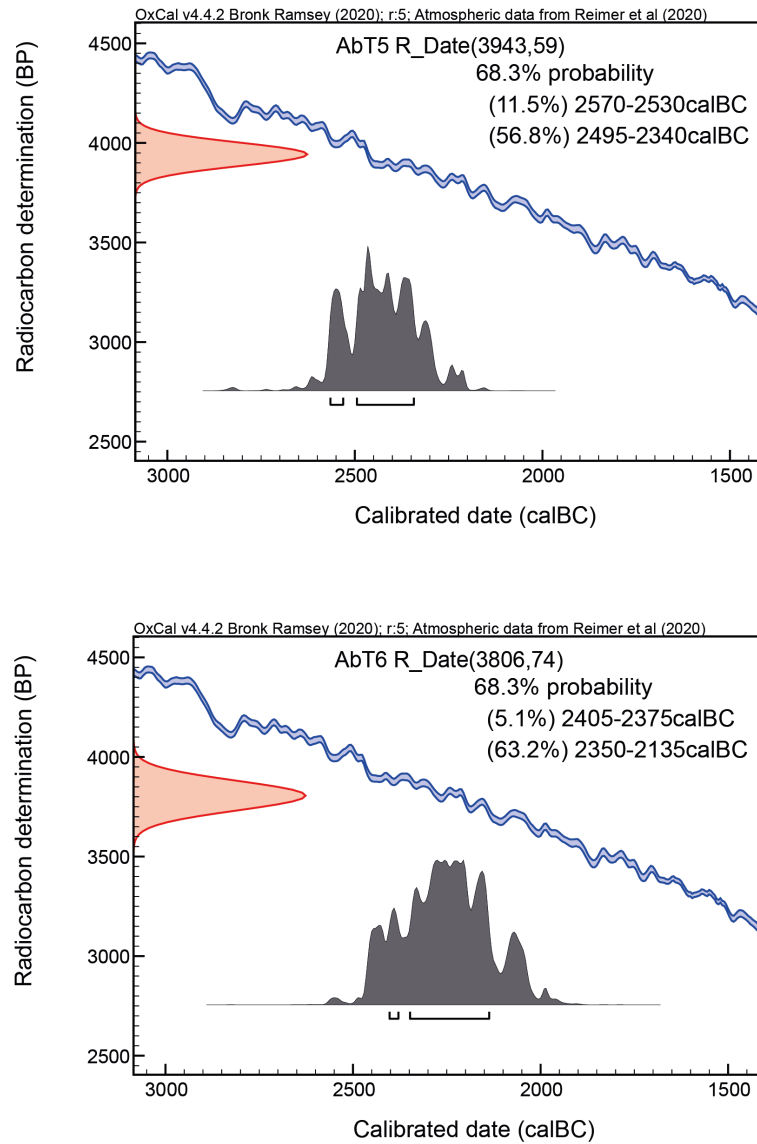


Figure 4.9: t_{rC} calibrated age for the sample AbT5 and AbT6. The blue line represents the calibration curve InrCal20, the conventional age of radiocarbon is reported on the y-axis and it is treated as a gaussian distribution. The curve width is given by the experimental uncertainty of the measured t_{rC} . The probability distribution for the calibrated age (grey shadow) is reported on the x-axis. The calibrated age ranges are reported on top of the graph, with the respective $1 - \sigma$ level of confidence. For each range, the probability that the true age value falls within is indicated.

Conclusions and outlook

The Ph.D. research activity described in this thesis was focused on the optimization and validation of the SCAR spectroscopic technique able to realise an accurate and all-optical measurement of the ^{14}C content in real-world samples, related to three thematic areas of high strategic importance. The procedure of analysis was defined by evaluating the critical aspects in the elimination of possible interfering molecules, that is an extremely important issue, given the analytical complexity in the measurement of trace elements such as radiocarbon. This result, which provided a significant improvement in the SNR, was possible thanks to the realization of a sample preparation protocol able to remove the interfering molecules that affect the spectroscopic measurement of $^{14}\text{CO}_2$. The methodology was then used for the analysis of samples of different nature and carbon content, to cover up the different fields of investigation with ^{14}C . The comparison with the standard methodology for the measurement of radiocarbon, AMS, demonstrated the high accuracy and precision of the SCAR technology for the analysis of modern samples in a wide range of concentrations of ^{14}C , such as biofuel blends or biobased materials. Moreover, the promotion of energy production from renewable sources is one of the objectives of the global energy policy and it constitutes the essential part of the package of measures needed to reduce greenhouse gas emissions, in line with the Paris Agreement on Climate Change. The agreement provides for holding the increase of global average temperature to well below 2°C above pre-industrial levels. Hence, deeper and faster cuts in emissions are required to shift to a highly efficient and renewable-based energy system by 2050. at the latest [75]. In this scenario, the industrial sector is expected to certify biogenic sources, accurately measuring the amount of radiocarbon as unequivocal marker of the presence of biogenic compounds. This can represent an effective method to carry out this task. Moreover, the certification of biofuel blends could play a key role in promoting globally adopted initiatives to mitigate greenhouse-gases warming, limiting the use of fossil fuels. Thus, the determination of radiocarbon content acquires a high value in certifying “green” products, which is currently considered an instance of great interest. By means of the SCAR technique, the radiocarbon content of these bio-materials can be measured in the full range, 0 - 100%, with a precision of 1% on the biofraction (1 pMC) in a measurement time shorter than 2 hours for each sample, by using a compact setup that, therefore, can be in principle deployed on-site. The compact dimensions of the SCAR spectrometer, if

compared with a typical AMS system, give further advantages. For example, a SCAR system can be easily set up in decommissioned nuclear power plants areas, to monitor nuclear waste containing concentrations of ^{14}C above the natural abundance. Furthermore, the comparison with AMS enlightened the absolute competitiveness of the SCAR technique also in the field of archaeometric dating, where high precision and the ultimate sensitivity are required.

With the aim of further reducing costs and dimensions of the C14-SCAR apparatus, this work moved in parallel with the purposes of the CNR spin-off company ppqSense s.r.l., which has the mission to realize a compact commercial SCAR setup. A new generation SCAR spectrometer will pave the way to new fields of application, such as direct analysis of atmospheric samples for climate change monitoring. Considering the highly compact size of this apparatus, it could become an integral part of a mobile station for atmospheric carbon collection and in situ analysis. To this purpose, it makes sense to thoroughly explore the possibility of using radiation in the vacuum UV range ($<200\text{ nm}$) to photodissociate N_2O molecules. The effectiveness of this approach was tested and the results are reported in the appendix.

Although the detection of mid-IR radiation raises a lot of interest since significant chemical compounds exhibit strong spectral fingerprints in this region, simple, low-noise, room-temperature detectors lag behind. Emerging applications, particularly in monitoring of trace molecules, call for improved detection systems that challenge present sensitivity levels. Measuring mid-IR light is often limited by the noise due to thermal background fluctuations. Indeed, our setup uses a photovoltaic detector based on InSb semiconductor that, due to its low bandgap energy, even at cryogenic temperatures, suffers from large dark current values generated by thermal radiation detected within its field of view. The IR power transmitted by the SCAR cavity is about 10 mW, thus it needs to be attenuated down to $100\ \mu\text{W}$ before photodiode detection. Alternatively frequency upconversion can be evaluated, instead of direct IR detection [76, 77]. In particular, sum-frequency generation (SFG) in a periodically-poled lithium niobate (PPLN) crystal can be used to shift the IR signal to near-visible wavelengths, so that it can be detected using a silicon-based photodiode [78, 79]. These detectors boast a performance far superior to mid-IR detectors in terms of efficiency, speed and noise. This circumvents or greatly reduces the noise sources associated with IR detection and eliminates the need for cryogenic cooling of the detector.

As we described in this work, both sensitivity and selectivity are crucial in trace gas detection and, certainly, one-photon absorption shows a limitation in terms of selectivity, due to the high density of molecular transitions that lie in the mid-IR spectral range. It becomes particularly problematic since detectors in this range have limited sensitivity. A very recent paper by Kevin K. Lehmann [80] provided a theoretical calculation of the sensitivity limits for two-photon cavity ring-down spectroscopy. With its analysis, he predicts a theoretical detection limit of 32 ppq ($10^{-15}\ \text{Hz}^{-1/2}$) for $^{12}\text{C}^{16}\text{O}_2$, higher than the sensitivity achieved with one-photon absorption [80, 81]. It depends on the interesting feature of the two-photon absorption process, to be intrinsically Doppler-free. On one hand, it means that it could

be possible to work at lower pressure, hence lower samples mass, with weaker Lorentzian interferences, that means easier isolation of the ultra narrow target line (even narrower than 10 MHz). On the other hand, designing a two-photon absorption set up for detection of the $^{14}\text{CO}_2$ target line is a challenging task, because finding a transition with a virtual level close to a real one is anything but trivial.

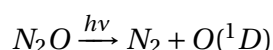
Finally, the present work and the last considerations let us deem that SCAR proves to be a powerful technique for the evaluation of biogenic content in any organic material. This first demonstration of the very wide applicability of the C14-SCAR technique paves the way for a new generation of compact on-site deployable spectrometers that may prove crucial in certifying the worldwide adoption of biobased materials as well as monitoring environmental quality.

Appendix

A

Photodissociation of N₂O molecule

Before solving the problem of removing interferents by means of the EA unit optimization described in Sec. 3.5, although the circuit for the CO₂ extraction had been setup, other different methods were considered. Typical chemical approaches were excluded mainly because they can not guarantee purity levels of few ppb. The possibility of inducing the decomposition of nitrous oxides by photochemical effects was evaluated. The photochemistry of nitrous oxides is widely characterized in the literature [82] since it involves in reactions that commonly occur in the upper atmosphere. Although N₂O is a nonreactive species, the absorption of ultraviolet radiation ($\lambda < 212$ nm) induces its decomposition according to the generic reaction:



Moreover, the singlet oxygen thus produced is highly reactive and can contribute to further removal of residual N₂O through different reactions that have nitrogen monoxide, nitrogen and oxygen as their main products. The mid-IR absorption band of these chemical species does not overlap with the ¹⁴CO₂ target line, while they do not interfere with the SCAR measurement. The advantage of using a photochemical method for the elimination of N₂O resides in the specificity of the process, indeed by appropriately selecting the wavelength of the radiation used for the irradiation of the mixture, it is possible to induce a highly selective photochemical reaction, thus preserving the concentration of carbon dioxide. The absorption cross section of CO₂ falls in a range of wavelengths between approximately 120 nm and 180 nm [83, 84] while

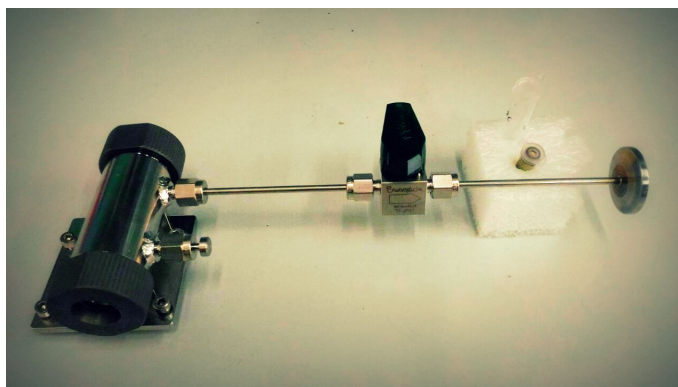


Figure 1.1: Alpha sampling module for gas modified to be filled with technical gases

for the N₂O molecule the absorption is between 160 nm and 220 nm, with a maximum at 182 nm ($1.47 \times 10^{-19} \text{ cm}^2 \text{ molecule}^{-1}$) [85, 86]. In order to avoid the photodissociation of CO₂ it is therefore necessary to operate with a source of electromagnetic radiation between 185 nm and 220 nm. In this way the photolysis of N₂O is guaranteed and that of CO₂ is excluded or in any case strongly minimized. To this aim, two different laser sources were considered. These tests were realized on technical gas samples provided by Nippon gases. These samples were irradiated with different sources and the FTIR spectrum was acquired to verify the photodissociation of the N₂O and that ¹²CO₂ remained unaltered. The FTIR alpha (Bruker) was used to record the IR spectrum. It is equipped with a sampling module consisting in a gas cell of 7 cm of optical path with CaF₂ windows (see Fig. 1.1) that allows the measurement of gaseous mixtures by transmission IR spectroscopy. In order to make the filling with gas possible, an aluminum channel (6 mm diameter) was fixed on the gas cell. It can be directly connect to the vacuum pump of the SCAR system. Once the vacuum has been achieved, the gas cell was filled with 100 mbar of N₂O and the FTIR spectrum of a sample of pure N₂O at room temperature was recorded. It is shown in Fig. 1.2 (on the top left hand side). In the spectrum we can observe the two N₂O fundamental ro-vibrational bands at 1290 cm⁻¹ and 2220 cm⁻¹ corresponding respectively to the symmetric and antisymmetric stretching of the molecule. The other weaker bands at higher frequency are different combination of the fundamental modes. This reference spectrum was used to make a comparison with the photolysed molecule. The first results in the photodissociation of N₂O were provided by the use of radiation at 206 nm delivered by a Nd:YAG laser [87]. A first test was aimed to verify that ¹²CO₂ was not photolysed. The sample gas cell was filled with 100 mbar of pure ¹²CO₂ and irradiated for about 15 hours. In Fig. 1.2 (on the top right hand side) the FTIR spectrum of the fundamental antisymmetric stretching band was acquired. The ¹²CO₂ absorption spectrum is unchanged despite the long irradiation time. This demonstrated that the radiation used does not induce ¹²CO₂ photolysis. Afterwards, 100 mbar mixtures of N₂O and ¹²CO₂ in a ratio 1:1 were made. The photodissociation of N₂O was observed as it was shown in Fig. 1.2 (on the

bottom left hand side). The black spectrum represents the non-irradiated molecule while the spectra recorded at increasing time under UV irradiation shows the N₂O photodissociation. The kinetics of N₂O decomposition can be estimated by fitting the intensity of the peaks as a function of time to an exponential function, as shown in Fig. 1.2 (on the bottom, right hand side). The analysis shows that, although the radiation used is effective for photolysis of N₂O, the kinetic constant obtained is quite long (approximately 25 h⁻¹) since the wavelength of the UV lased used does not correspond to the maximum of the N₂O photodissociation peak. Therefore, we have evaluated the possibility of using more effective sources. Among the most

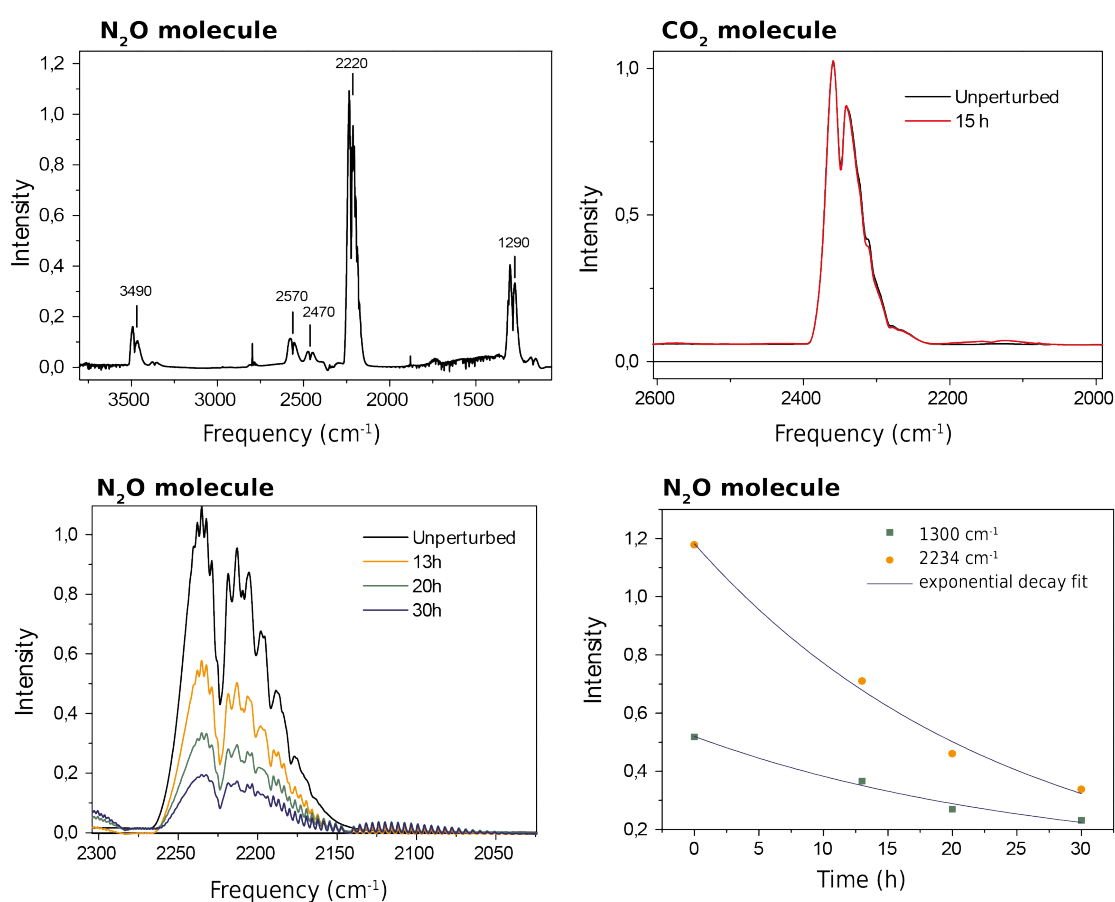


Figure 1.2: FTIR spectrum of non-irradiated N₂O molecule (left hand side on the top) and FTIR spectrum of ¹²CO₂ molecule before (black line) and after (red line) exposure of 206 nm radiation (right hand side on the top). Photodissociation rate of N₂O molecule by means of 206 nm radiation (left hand side on the bottom) and kinetics of N₂O decomposition (right hand side on the bottom)

suitable sources are excimer lamps and lasers, capable of producing short wavelength UV radiation [88, 89]. We initially evaluated the possibility of using a lamp, but the commercially available solutions were not suitable for our purposes. In fact, the most compact source found

in literature, is a lamp with an emission peak at 172 nm. This solution was discarded since this wavelength could also induce photolysis of CO_2 . Therefore, the possibility of using an ArF excimer laser, which emits a radiation peaked at 196 nm, was considered since this laser was available in the laboratories of the IFAC-CNR institute in Sesto Fiorentino. An excimer laser involves the use of a combination of noble gas (Xe, Ar) and a reactive gas (F, Cl). Under adequate conditions of pressure and electrical stimulation, a molecule is created that can only exist in an excited state (excimer), capable of generating coherent light in the UV range. Noble gases are highly inert and usually do not form chemical compounds, however, if they are in the excited state (induced by an electric discharge or high-energy electron beams), they can form molecules temporarily binding to themselves (excimer) or to halogens (exciplexes). The excited compound is able to release excess energy, emitting UV photons, by undergoing spontaneous or stimulated emission, generating a highly repulsive ground state molecule that dissociates very quickly (picoseconds) into two unbound atoms. In order to improve the efficiency of the photodissociative process under examination, the pulsed source (Lambda Physik, Compex 102) ArF excimer laser was used, which emits at 193 nm with energy per pulse of 40 mJ and repetition rate of 4 Hz. A new 100 mbar mixture of $^{12}CO_2$ and N_2O in a ratio 1:1 were realized for the photolysis experiment by means of the excimer lasers. Fig. 1.3 proves the effectiveness of the photodissociation of N_2O induced by the excimer laser source and shows the FTIR spectra that were acquired. In order to monitor the progress of the reaction

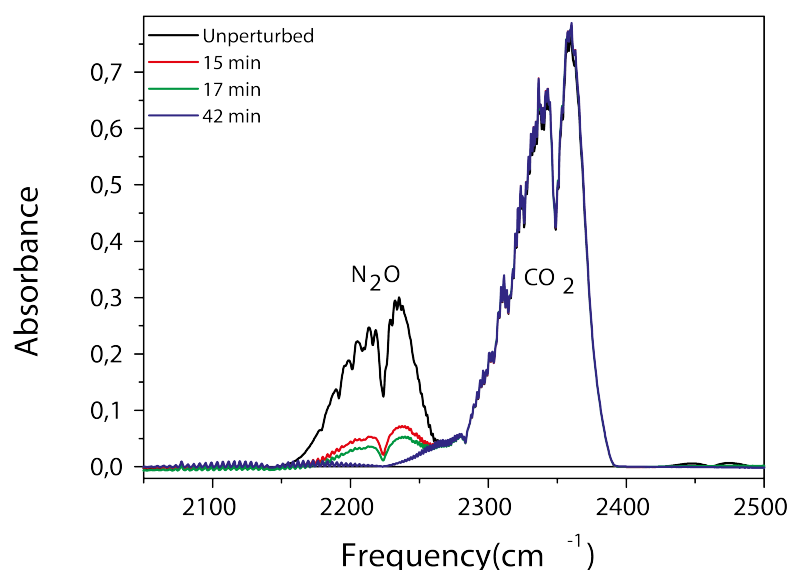


Figure 1.3: **FTIR spectra of 1:1 $^{12}CO_2/N_2O$ mixture at room temperature, before and after photolysis.** The black line represents the non-irradiated sample spectrum, the red green and blue lines show the photodissociation of N_2O by means of 193 nm radiation

through the SCAR system, we must take into account that the optical cavity must be filled

with 12 mbar of CO₂. Since the volume of the optical cavity is 0.7 L, estimated that the loading circuit of the optical cavity consists of an additional volume of 1.0 L, and considering that the volume of the sample cell used is equal to 0.014 L, the pressure necessary for filling the sample cell is: $P = 1457$ mbar. The sample cell was filled with a gas mixture ($\sim 100\%$ CO₂ and traces of N₂O coming from the combustion reaction) obtained by burning a sample weakly irradiated by neutrons (enriched graphite). The sample, which resulted in a gaseous mixture of CO₂ and N₂O, was collected in a Schlenk flask of 250 mL volume and analysed with the SCAR technique before being irradiated with the excimer laser. Fig. 1.4 (left hand side) shows

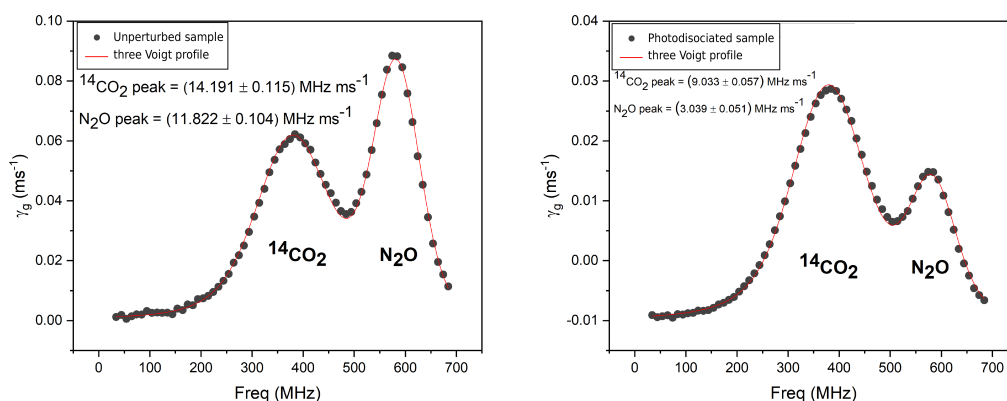


Figure 1.4: An enriched sample of graphite before (left hand side) and after (right hand side) irradiation by means of excimer laser at 193 nm

the SCAR spectrum of the described sample. The frequency scale is relative to the absolute frequency of 66227000 MHz. Centered at 400 MHz ($2209.1077 \text{ cm}^{-1}$) we can see the target ($00^0 1-00^0$) P(20) transition of $^{14}\text{CO}_2$, while centered at about 600 MHz ($2209.1144 \text{ cm}^{-1}$) we can see the ($01^1 1-01^1 0$) Q(12)e transition of the interfering molecule N₂O. The spectral area measured allows us to conclude that the sample shown is enriched in ^{14}C by almost a factor of ~ 10 with respect to natural abundance. The sample was collected back in the sample holder cell by means of a liquid nitrogen bath and placed under irradiation of the laser source at 193 nm for a time of 3 hours, with initial energy per pulse of 40 mJ (final laser energy = 30 mJ) and a repetition rate of 4 Hz. Then, it was again measured with the SCAR apparatus. Although it was observed that the irradiation of N₂O with the UV source at 193 nm led to the theorized results in a reasonable time, also the reduction of the $^{14}\text{CO}_2$ spectral area was observed after irradiation. This reduction could be due to an isotopic shift of the UV absorption spectrum of the target molecule, which could therefore have partially been photodissociated, but also in a dilution error due to logistical complexity. In fact, the laser suitable for photodissociation of the sample was in another laboratory. We cannot therefore rule out possible losses during transport. This hypothesis was not further investigated because another elegant solution for

the interferent removal was found, as described in Sec. 3.5.

List of abbreviations

AMS	Accelerator Mass Spectrometry
CRD	Cavity Ring Down
CRDS	Cavity Ring Down Spectroscopy
CW	Continuous-Wave
DFG	Difference-Frequency Generation
DoF	Degree of Freedom
EA	Elemental analyser
FET	Field-Effect Transistor
FNPSD	Frequency Noise Power Spectral Density
FSR	Free Spectral Range
FTIR	Fourier Transform Interferometer
FWHM	Full Width at Half Maximum
GPC	Gas Proportional Counting
ICOGS	Intra-Cavity OptoGalvanic Spectroscopy
JRC	Joint Research Centre
LO	Local Oscillator
LSC	Liquid Scintillation Counting
mid-IR	mid-InfraRed

NICE-OHMS Noise-Immune Cavity-Enhanced Optical Heterodyne Molecular Spectroscopy

NIST National Institute of Standards and Technology

NOX New Oxalic Acid

NPSD Noise Power Spectral Density

OGE OptoGalvanic Effect

PI Proportional-Integral

PID Proportional-Integral-Derivative

PDH Pound-Drever-Hall

pMC percent Modern Carbon

PLL Phase-Locked Loop

PPLN Periodically-Poled Lithium Niobate (LiNbO₃)

PS Polarization Spectroscopy

QCL Quantum Cascade Laser

RF Radio Frequency

RMS Root Mean Square

SCAR Saturated Absorption Cavity Ring down

SFG Sum-Frequency Generation

SNR Signal-to-Noise Ratio

SRM Standard Reference Material

TCD Thermal Conductivity Detector

TEM Transverse Electro-Magnetic

Bibliography

- [1] D Mazzotti et al. “Search for exchange-antisymmetric states for spin-0 particles at the 10^{-11} level”. In: *Phys. Rev. Lett.* 86 (2001), p. 1919. DOI: [10.1103/PhysRevLett.86.1919](https://doi.org/10.1103/PhysRevLett.86.1919).
- [2] E J Zak et al. “Room temperature line lists for CO₂ asymmetric isotopologues with *ab initio* computed intensities”. In: *J. Quant. Spectrosc. Radiat. Transfer* 203 (2017), p. 265. DOI: [10.1016/j.jqsrt.2017.01.037](https://doi.org/10.1016/j.jqsrt.2017.01.037).
- [3] W Demtröder. *Laser spectroscopy. Vol 1: Basic principles*. 3rd. Advanced Texts in Physics. Springer, 2008. DOI: [10.1007/978-3-662-05155-9](https://doi.org/10.1007/978-3-662-05155-9).
- [4] P Maddaloni, M Bellini, and P De Natale. *Laser-based measurements for time and frequency domain applications: a handbook*. Series in Optics and Optoelectronics. CRC Press, 2013. URL: <http://www.crcpress.com/product/isbn/9781439841518>.
- [5] W Demtröder. *Laser spectroscopy. Vol. 2: Experimental techniques*. Vol. 2. Springer, 2008. DOI: [10.1007/978-3-540-74954-7](https://doi.org/10.1007/978-3-540-74954-7).
- [6] J Faist et al. “Quantum cascade laser”. In: *Science* 264 (1994), p. 553. DOI: [10.1126/science.264.5158.553](https://doi.org/10.1126/science.264.5158.553).
- [7] A A Kosterev et al. “Methane concentration and isotopic composition measurements with a mid-infrared quantum-cascade laser”. In: *Opt. Lett.* 24 (1999), p. 1762. DOI: [10.1364/OL.24.001762](https://doi.org/10.1364/OL.24.001762).
- [8] L Menzel et al. “Spectroscopic detection of biological NO with a quantum cascade laser”. In: *Appl. Phys. B* 72 (2001), p. 859. DOI: [10.1007/s003400100562](https://doi.org/10.1007/s003400100562).
- [9] S Bartalini, S Borri, and P De Natale. “Doppler-free polarization spectroscopy with a quantum cascade laser at 4.3 μm ”. In: *Opt. Express* 17 (2009), p. 7440. DOI: [10.1364/OE.17.007440](https://doi.org/10.1364/OE.17.007440).
- [10] F Cappelli et al. “Subkilohertz linewidth room-temperature mid-IR quantum cascade laser using a molecular sub-Doppler reference”. In: *Opt. Lett.* 37 (2012), p. 4811. DOI: [10.1364/OL.37.004811](https://doi.org/10.1364/OL.37.004811).

- [11] E D Black. “An introduction to Pound–Drever–Hall laser frequency stabilization”. In: *Am. J. Phys.* 69 (2001), p. 79. DOI: [10.1119/1.1286663](https://doi.org/10.1119/1.1286663).
- [12] R W P Drever et al. “Laser phase and frequency stabilization using an optical resonator”. In: *Appl. Phys. B* 31 (1983), p. 97. DOI: [10.1007/BF00702605](https://doi.org/10.1007/BF00702605).
- [13] D Romanini et al. “Introduction to Cavity Enhanced Absorption Spectroscopy”. In: *Springer Series in Optical Sciences* 179 (Jan. 2014), pp. 1–60. DOI: [10.1007/978-3-642-40003-2-1](https://doi.org/10.1007/978-3-642-40003-2-1).
- [14] G Gagliardi and H–P Loock, eds. *Cavity-enhanced spectroscopy and sensing*. Vol. 179. Springer Series in Optical Sciences. Springer, 2014. DOI: [10.1007/978-3-642-40003-2](https://doi.org/10.1007/978-3-642-40003-2).
- [15] A O’Keefe and D A G Deacon. “Cavity ring-down optical spectrometer for absorption measurements using pulsed laser sources”. In: *Rev. Sci. Instrum.* 59 (1988), p. 2544. DOI: [10.1063/1.1139895](https://doi.org/10.1063/1.1139895).
- [16] M Mazurenka et al. “Cavity ring-down and cavity enhanced spectroscopy using diode lasers”. In: *Annu. Rep. Prog. Chem. C* 101 (2005), p. 100. DOI: [10.1039/b408909j](https://doi.org/10.1039/b408909j).
- [17] D Romanini, P Dupré, and R Jost. “Non-linear effects by continuous wave cavity ring-down spectroscopy in jet-cooled NO₂”. In: *Vib. Spectrosc.* 19 (1999), p. 93. DOI: [10.1016/S0924-2031\(99\)00018-1](https://doi.org/10.1016/S0924-2031(99)00018-1).
- [18] H Huang and K K Lehmann. “Sensitivity limits of continuous wave cavity ring-down spectroscopy”. In: *J. Phys. Chem. A* 117 (2013), p. 13399. DOI: [10.1021/jp406691e](https://doi.org/10.1021/jp406691e).
- [19] P Cancio et al. “Saturated-absorption cavity ring-down (SCAR) for high-sensitivity and high-resolution molecular spectroscopy in the mid IR”. In: *Cavity-enhanced spectroscopy and sensing*. Ed. by G Gagliardi and H–P Loock. Vol. 179. Springer Series in Optical Sciences. Springer, 2014, p. 143. DOI: [10.1007/978-3-642-40003-2_4](https://doi.org/10.1007/978-3-642-40003-2_4).
- [20] Jochen Hoefs. “Stable Isotope Geochemistry”. In: (Jan. 2015). DOI: [10.1007/978-3-319-19716-6](https://doi.org/10.1007/978-3-319-19716-6).
- [21] L M Libby and H R Lukens. “Production of radiocarbon in tree rings by lightning bolts”. In: *Journal of Geophysical Research* 78.26 (1973), pp. 5902–5903. DOI: [10.1029/JB078i026p05902](https://doi.org/10.1029/JB078i026p05902).
- [22] Christopher Bronk Ramsey. “Radiocarbon dating: revolutions in understanding”. In: *Archaeometry* 50.2 (2008), pp. 249–275. DOI: [10.1111/j.1475-4754.2008.00394.x](https://doi.org/10.1111/j.1475-4754.2008.00394.x).
- [23] R E Taylor and Ofer Bar. “Radiocarbon Dating: An Archaeological Perspective”. In: *American Journal of Archaeology* 122.2 (2018). DOI: [10.1002/gea.21519](https://doi.org/10.1002/gea.21519).

- [24] H Oeschger et al. “A box diffusion model to study the carbon dioxide exchange in nature”. In: *Tellus* 27.2 (1975), pp. 168–192. DOI: [10.3402/tellusa.v27i2.9900](https://doi.org/10.3402/tellusa.v27i2.9900). eprint: <https://doi.org/10.3402/tellusa.v27i2.9900>. URL: <https://doi.org/10.3402/tellusa.v27i2.9900>.
- [25] J R Arnold and W F Libby. “Age determinations by radiocarbon content: checks with samples of known age”. In: *Science* 110 (1949), p. 678. DOI: [10.1126/science.110.2869.678](https://doi.org/10.1126/science.110.2869.678).
- [26] M Stuiver and H A Polach. “Discussion: reporting of ^{14}C data”. In: *Radiocarbon* 19 (1977), p. 355. DOI: [10.1017/S0033822200003672](https://doi.org/10.1017/S0033822200003672).
- [27] W Kutschera. “The half-life of ^{14}C – why is it so long?” In: *Radiocarbon* (2019). DOI: [10.1017/RDC.2019.26](https://doi.org/10.1017/RDC.2019.26).
- [28] Eric T Sundquist. “Geological perspectives on carbon dioxide and the carbon cycle”. In: *The carbon cycle and atmospheric CO₂: natural variations archean to present* 32 (1985), pp. 55–59. DOI: [10.1029/GM032p0005](https://doi.org/10.1029/GM032p0005).
- [29] Alpreth Neftel et al. “Ice core sample measurements give atmospheric CO₂ content during the past 40,000 yr”. In: *Nature* 295.5846 (1982), pp. 220–223. DOI: [10.1038/295220a0](https://doi.org/10.1038/295220a0).
- [30] Eric Monnin et al. “Atmospheric CO₂ concentrations over the last glacial termination”. In: *Science* 291.5501 (2001), pp. 112–114. DOI: [10.1126/science.291.5501.112](https://doi.org/10.1126/science.291.5501.112).
- [31] Julia Pongratz et al. “Effects of anthropogenic land cover change on the carbon cycle of the last millennium”. In: *Global Biogeochemical Cycles* 23.4 (2009). DOI: [10.1029/2009GB003488](https://doi.org/10.1029/2009GB003488).
- [32] H E Suess. “Radiocarbon concentration in modern wood”. In: *Science* 122 (1955), p. 415. DOI: [10.1126/science.122.3166.415-a](https://doi.org/10.1126/science.122.3166.415-a).
- [33] E A G Schuur, E Druffel, and S E Trumbore, eds. *Radiocarbon and climate change. Mechanisms, applications and laboratory techniques*. Springer, 2016. DOI: [10.1007/978-3-319-25643-6](https://doi.org/10.1007/978-3-319-25643-6).
- [34] Reidar Nydal. “Increase in radiocarbon from the most recent series of thermonuclear tests”. In: *Nature* 200.4903 (1963), pp. 212–214. DOI: [10.1038/200212a0](https://doi.org/10.1038/200212a0).
- [35] J Masarik and J Beer. “Simulation of particle fluxes and cosmogenic nuclide production in the Earth’s atmosphere”. In: *Journal of Geophysical Research: Atmospheres* 104.D10 (1999), pp. 12099–12111. DOI: [10.1029/1998JD200091](https://doi.org/10.1029/1998JD200091).
- [36] Monty Charles. “UNSCEAR Report 2000: sources and effects of ionizing radiation”. In: *Journal of Radiological Protection* 21.1 (2001), p. 83. URL: https://www.unscear.org/docs/publications/2000/UNSCEAR_2000_Report_Vol.I.pdf.

- [37] Gregg Marland. “Accounting for carbon dioxide emissions from bioenergy systems”. In: *Journal of Industrial Ecology* 14.6 (2010). DOI: [10.1111/jieec.12043](https://doi.org/10.1111/jieec.12043).
- [38] Ingeborg Levin et al. “Observations and modelling of the global distribution and long-term trend of atmospheric $^{14}\text{CO}_2$ ”. In: *Tellus B: Chemical and Physical Meteorology* 62.1 (2010), pp. 26–46. DOI: [10.1111/j.1600-0889.2009.00446.x](https://doi.org/10.1111/j.1600-0889.2009.00446.x).
- [39] H D Graven, T P Guilderson, and R F Keeling. “Observations of radiocarbon in CO_2 at La Jolla, California, USA 1992–2007: Analysis of the long-term trend”. In: *Journal of Geophysical Research: Atmospheres* 117.D2 (2012). DOI: [10.1029/2011JD016533](https://doi.org/10.1029/2011JD016533).
- [40] H D Graven, T P Guilderson, and R F Keeling. “Observations of radiocarbon in CO_2 at seven global sampling sites in the Scripps flask network: Analysis of spatial gradients and seasonal cycles”. In: *Journal of Geophysical Research: Atmospheres* 117.D2 (2012). DOI: [10.1029/2011JD016535](https://doi.org/10.1029/2011JD016535).
- [41] HL De Vries and GW Barendsen. “Measurements of age by the carbon-14 technique”. In: *Nature* 174.4442 (1954), pp. 1138–1141. DOI: [10.1038/1741138a0](https://doi.org/10.1038/1741138a0).
- [42] Pall Theodorsson. “Gas proportional versus liquid scintillation counting, radiometric versus AMS dating”. In: *Radiocarbon* 33.1 (1991), pp. 9–13. DOI: [10.1017/S0033822200013163](https://doi.org/10.1017/S0033822200013163).
- [43] Harold Barker. “Radiocarbon dating: large-scale preparation of acetylene from organic material”. In: *Nature* 172.4379 (1953), pp. 631–632. DOI: [10.1038/172631a0](https://doi.org/10.1038/172631a0).
- [44] Henry Anthony Polach and JJ Stipp. “Improved synthesis techniques for methane and benzene radiocarbon dating”. In: *The International Journal of Applied Radiation and Isotopes* 18.6 (1967), pp. 359–364. DOI: [10.1016/0020-708X\(67\)90139-1](https://doi.org/10.1016/0020-708X(67)90139-1).
- [45] H-A Synal and L Wacker. “AMS measurement technique after 30 years: possibilities and limitations of low energy systems”. In: *Nucl. Instrum. Methods Phys. Res. Sect. B* 268 (2010), p. 701. DOI: [10.1016/j.nimb.2009.10.009](https://doi.org/10.1016/j.nimb.2009.10.009).
- [46] W Kutschera. “Accelerator mass spectrometry: state of the art and perspectives”. In: *Adv. Phys.* X 1 (2016), p. 570. DOI: [10.1080/23746149.2016.1224603](https://doi.org/10.1080/23746149.2016.1224603).
- [47] M Wahlen, R S Eng, and K W Nill. “Tunable diode laser spectroscopy of $^{14}\text{CO}_2$: absorption coefficients and analytical applications”. In: *Appl. Opt.* 16 (1977), p. 2350. DOI: [10.1364/AO.16.002350](https://doi.org/10.1364/AO.16.002350).
- [48] D Labrie and J Reid. “Radiocarbon dating by infrared laser spectroscopy. A feasibility study”. In: *Appl. Phys.* 24 (1981), p. 381. DOI: [10.1007/BF00899738](https://doi.org/10.1007/BF00899738).
- [49] I Galli et al. “The ν_3 band of $^{14}\text{C}^{16}\text{O}_2$ molecule measured by optical-frequency-comb-assisted cavity ring-down spectroscopy [Invited article]”. In: *Mol. Phys.* 109 (2011), p. 2267. DOI: [10.1080/00268976.2011.614284](https://doi.org/10.1080/00268976.2011.614284).

- [50] D E Murnick, O Dogru, and E Ilkmen. "Intracavity optogalvanic spectroscopy. An analytical technique for ^{14}C analysis with subattomole sensitivity". In: *Anal. Chem.* 80 (2008), p. 4820. DOI: [10.1021/ac800751y](https://doi.org/10.1021/ac800751y).
- [51] D Romanini et al. "CW cavity ring down spectroscopy". In: *Chem. Phys. Lett.* 264 (1997), p. 316. DOI: [10.1016/S0009-2614\(96\)01351-6](https://doi.org/10.1016/S0009-2614(96)01351-6).
- [52] G Genoud et al. "Radiocarbon dioxide detection based on cavity ring-down spectroscopy and a quantum cascade laser". In: *Opt. Lett.* 40 (2015), p. 1342. DOI: [10.1364/OL.40.001342](https://doi.org/10.1364/OL.40.001342).
- [53] A D McCartt et al. "Quantifying carbon-14 for biology using cavity ring-down spectroscopy". In: *Anal. Chem.* 88 (2016), p. 8714. DOI: [10.1021/acs.analchem.6b02054](https://doi.org/10.1021/acs.analchem.6b02054).
- [54] A J Fleisher et al. "Optical measurement of radiocarbon below unity fraction modern by linear absorption spectroscopy". In: *J. Phys. Chem. Lett.* 8 (2017), p. 4550. DOI: [10.1021/acs.jpcclett.7b02105](https://doi.org/10.1021/acs.jpcclett.7b02105).
- [55] I Galli et al. "Molecular gas sensing below parts per trillion: radiocarbon-dioxide optical detection". In: *Phys. Rev. Lett.* 107 (2011), p. 270802. DOI: [10.1103/PhysRevLett.107.270802](https://doi.org/10.1103/PhysRevLett.107.270802).
- [56] I Galli et al. "Spectroscopic detection of radiocarbon dioxide at parts-per-quadrillion sensitivity". In: *Optica* 3 (2016), p. 385. DOI: [10.1364/optica.3.000385](https://doi.org/10.1364/optica.3.000385).
- [57] Jean-Robert Petit et al. "Climate and atmospheric history of the past 420,000 years from the Vostok ice core, Antarctica". In: *Nature* 399.6735 (1999), p. 429. DOI: [10.1038/20859](https://doi.org/10.1038/20859).
- [58] J Mohn et al. "Fossil and biogenic CO_2 from waste incineration based on a yearlong radiocarbon study". In: *Waste Management* 32.8 (2012), pp. 1516–1520. DOI: [10.1016/j.wasman.2012.04.002](https://doi.org/10.1016/j.wasman.2012.04.002).
- [59] Glenn A Norton and Steven L Devlin. "Determining the modern carbon content of biobased products using radiocarbon analysis". In: *Bioresource technology* 97.16 (2006), pp. 2084–2090. DOI: [10.1016/j.biortech.2005.08.017](https://doi.org/10.1016/j.biortech.2005.08.017).
- [60] Kumar Sudesh and Tadahisa Iwata. "Sustainability of biobased and biodegradable plastics". In: *CLEAN–Soil, Air, Water* 36.5-6 (2008), pp. 433–442. DOI: [10.1002/clean.200700183](https://doi.org/10.1002/clean.200700183).
- [61] G Quarta et al. "Determination of the biobased content in plastics by radiocarbon". In: *Radiocarbon* 55.2–3 (2013), pp. 1834–1844. DOI: [10.1017/S0033822200048748](https://doi.org/10.1017/S0033822200048748).
- [62] Toru Onishi et al. "Biomass carbon ratio of polymer composites included biomass or petroleum origin resources". In: *Polymer degradation and stability* 95.8 (2010), pp. 1276–1283. DOI: [10.1016/j.polydegradstab.2010.03.011](https://doi.org/10.1016/j.polydegradstab.2010.03.011).

- [63] G Lappin and R C Garner. “Current perspectives of ^{14}C -isotope measurement in biomedical accelerator mass spectrometry”. In: *Anal. Bioanal. Chem.* 378 (2004), p. 356. DOI: [10.1007/s00216-003-2348-5](https://doi.org/10.1007/s00216-003-2348-5).
- [64] Graham Lappin and R Colin Garner. “The use of accelerator mass spectrometry to obtain early human ADME/PK data”. In: *Expert opinion on drug metabolism & toxicology* 1.1 (2005), pp. 23–31. DOI: [10.1517/17425255.1.1.23](https://doi.org/10.1517/17425255.1.1.23).
- [65] F Lozac’h et al. “Evaluation of cAMS for ^{14}C microtracer ADME studies: opportunities to change the current drug development paradigm”. In: *Bioanalysis* 10 (2018), p. 321. DOI: [10.4155/bio-2017-0216](https://doi.org/10.4155/bio-2017-0216).
- [66] M A Malfatti et al. “Radiocarbon tracers in toxicology and medicine: recent advances in technology and science”. In: *Toxics* 7 (2019), p. 27. DOI: [10.3390/toxics7020027](https://doi.org/10.3390/toxics7020027).
- [67] Man-Sung Yim and François Caron. “Life cycle and management of carbon-14 from nuclear power generation”. In: *Progress in Nuclear Energy* 48.1 (2006), pp. 2–36. DOI: [10.1016/j.pnucene.2005.04.002](https://doi.org/10.1016/j.pnucene.2005.04.002).
- [68] G Giusfredi et al. “Saturated-absorption cavity ring-down spectroscopy”. In: *Phys. Rev. Lett.* 104 (2010), p. 110801. DOI: [10.1103/PhysRevLett.104.110801](https://doi.org/10.1103/PhysRevLett.104.110801).
- [69] E J Zak et al. “Room temperature line lists for CO_2 symmetric isotopologues with *ab initio* computed intensities”. In: *J. Quant. Spectrosc. Radiat. Transfer* 189 (2017), p. 267. DOI: [10.1016/j.jqsrt.2016.11.022](https://doi.org/10.1016/j.jqsrt.2016.11.022).
- [70] G Giusfredi et al. “Theory of saturated-absorption cavity ring-down: radiocarbon dioxide detection, a case study”. In: *J. Opt. Soc. Am. B* 32 (2015), p. 2223. DOI: [10.1364/JOSAB.32.002223](https://doi.org/10.1364/JOSAB.32.002223).
- [71] I E Gordon et al. “The HITRAN 2016 molecular spectroscopic database”. In: *J. Quant. Spectrosc. Radiat. Transfer* 203 (2017), p. 3. DOI: [10.1016/j.jqsrt.2017.06.038](https://doi.org/10.1016/j.jqsrt.2017.06.038).
- [72] Franco D’Agostino et al. “ABU TBEIRAH. PRELIMINARY REPORT OF THE FIRST CAMPAIGN (JANUARY-MARCH 2012)”. In: *Rivista degli studi orientali* 84.1/4 (2011), pp. 17–34. ISSN: 03924866, 17241863. URL: <http://www.jstor.org/stable/43927254>.
- [73] CSM Turney, D Wheeler, and Allan R Chivas. “Carbon isotope fractionation in wood during carbonization”. In: *Geochimica et Cosmochimica Acta* 70.4 (2006), pp. 960–964. DOI: [10.1016/j.gca.2005.10.031](https://doi.org/10.1016/j.gca.2005.10.031).
- [74] Paula J Reimer et al. “The IntCal20 Northern Hemisphere radiocarbon age calibration curve (0–55 cal kBP)”. In: *Radiocarbon* 62.4 (2020), pp. 725–757. DOI: [10.1017/RDC.2020.41](https://doi.org/10.1017/RDC.2020.41) [Opens in a new window].
- [75] European Union. “A European green deal: Striving to be the first climate-neutral continent”. In: (2019). URL: https://ec.europa.eu/info/strategy/priorities-2019-2024/european-green-deal_en.

- [76] P Tidemand-Lichtenberg et al. “Mid-infrared upconversion spectroscopy”. In: *J. Opt. Soc. Am. B* 33 (2016), p. D28. DOI: [10.1364/JOSAB.33.000D28](https://doi.org/10.1364/JOSAB.33.000D28).
- [77] S Junaid et al. “Video-rate, mid-infrared hyperspectral upconversion imaging”. In: *Optica* 6 (2019), p. 702. DOI: [10.1364/OPTICA.6.000702](https://doi.org/10.1364/OPTICA.6.000702).
- [78] Jeppe Seidelin Dam, Peter Tidemand-Lichtenberg, and Christian Pedersen. “Room-temperature mid-infrared single-photon spectral imaging”. In: *Nature photonics* 6.11 (2012), pp. 788–793. DOI: [10.1038/nphoton.2012.231](https://doi.org/10.1038/nphoton.2012.231).
- [79] Qi Hu et al. “High-resolution mid-IR spectrometer based on frequency upconversion”. In: *Optics letters* 37.24 (2012), pp. 5232–5234. DOI: [10.1364/OL.37.005232](https://doi.org/10.1364/OL.37.005232).
- [80] Kevin K Lehmann. “Optical cavity with intracavity two-photon absorption”. In: *JOSA B* 37.10 (2020), pp. 3055–3062. DOI: [10.1364/JOSAB.392539](https://doi.org/10.1364/JOSAB.392539).
- [81] Kevin K Lehmann. “Resonance enhanced two-photon cavity ring-down spectroscopy of vibrational overtone bands: A proposal”. In: *The Journal of Chemical Physics* 151.14 (2019), p. 144201. DOI: [10.1063/1.5122988](https://doi.org/10.1063/1.5122988).
- [82] Peter Warneck. *Chemistry of the natural atmosphere*. Elsevier, 1999. DOI: [10.1029/2002JD003348](https://doi.org/10.1029/2002JD003348).
- [83] WH Parkinson, J Rufus, and K Yoshino. “Absolute absorption cross section measurements of CO₂ in the wavelength region 163–200 nm and the temperature dependence”. In: *Chemical Physics* 290.2-3 (2003), pp. 251–256. DOI: [10.1016/S0301-0104\(03\)00146-0](https://doi.org/10.1016/S0301-0104(03)00146-0).
- [84] D Ityaksov, H Linnartz, and W Ubachs. “Deep-UV absorption and Rayleigh scattering of carbon dioxide”. In: *Chemical Physics Letters* 462.1-3 (2008), pp. 31–34. DOI: [10.1016/j.cplett.2008.07.049](https://doi.org/10.1016/j.cplett.2008.07.049).
- [85] Gary Selwyn, James Podolske, and Harold S Johnston. “Nitrous oxide ultraviolet absorption spectrum at stratospheric temperatures”. In: *Geophysical Research Letters* 4.10 (1977), pp. 427–430. DOI: [10.1029/GL004i010p00427](https://doi.org/10.1029/GL004i010p00427).
- [86] K Yoshino, DE Freeman, and WH Parkinson. “High resolution absorption cross-section measurements of N₂O at 295–299 K in the wavelength region 170–222 nm”. In: *Planetary and space science* 32.10 (1984), pp. 1219–1222. DOI: [10.1016/0032-0633\(84\)90065-5](https://doi.org/10.1016/0032-0633(84)90065-5).
- [87] Davide D’Ambrosio. “Characterizing a Mid-IR laser source with a molecular beam”. PhD thesis. XXXI Ciclo, Scuola di Metrologia, Politecnico di Torino, 2019. URL: <http://hdl.handle.net/11583/2749554>.
- [88] Masaharu Tsuji et al. “Photochemical removal of NO₂ by using 172-nm Xe₂ excimer lamp in N₂ or air at atmospheric pressure”. In: *Journal of hazardous materials* 162.2-3 (2009), pp. 1025–1033. DOI: [10.1016/j.jhazmat.2008.05.136](https://doi.org/10.1016/j.jhazmat.2008.05.136).

- [89] Masaharu Tsuji et al. "N₂O removal in N₂ or air by ArF excimer laser photolysis at atmospheric pressure". In: *Journal of hazardous materials* 108.3 (2004), pp. 189–197. DOI: [10.1016/j.jhazmat.2004.02.024](https://doi.org/10.1016/j.jhazmat.2004.02.024).